Quantifying the Impact of Altered Hemodynamics and Vascular Biomechanics to Changes in Structure and Function in Native and Corrected Aortic Coarctation

Arjun Menon
Marquette University

QUANTIFYING THE IMPACT OF ALTERED HEMODYNAMICS AND VASCULAR BIOMECHANICS TO CHANGES IN STRUCTURE AND FUNCTION IN NATIVE AND CORRECTED AORTIC COARCTATION

by

Arjun R. Menon

A Dissertation submitted to the Faculty of the Graduate School,
Marquette University,
in Partial Fulfillment of the Requirements for
the Degree of Doctor of Philosophy

Milwaukee, Wisconsin

May 2012

ABSTRACT
QUANTIFYING THE IMPACT OF ALTERED HEMODYNAMICS AND VASCULAR BIOMECHANICS TO CHANGES IN STRUCTURE AND FUNCTION IN NATIVE AND CORRECTED AORTIC COARCTATION

Arjun R. Menon

Marquette University, 2012

Coarctation of the aorta (CoA) is associated with substantial cardiovascular morbidities despite successful treatment through surgical or catheter-based intervention. Although specific mechanisms leading to these morbidities remain elusive, abnormal hemodynamics and vascular biomechanics are implicated. We used a novel animal model that facilitates quantification of CoA-induced hemodynamic and vascular biomechanics alterations and their impact on vascular structure and function, independent of genetic or confounding factors. Rabbits underwent thoracic CoA at 10 weeks of age (~9 human years) to induce a 20 mmHg blood pressure (BP) gradient using permanent or dissolvable suture thereby replicating untreated and corrected CoA. Computational fluid dynamics (CFD) was performed using subject-specific imaging and BP data at 32 weeks to quantify velocity, strain, and wall shear stress (WSS). Vascular structure and function were evaluated at proximal and distal locations by histology, immunohistochemistry, and myograph analysis.

Results revealed proximal systolic and mean BP was elevated in CoA compared to corrected and control rabbits leading to vascular remodeling, endothelial dysfunction proximally and distally, and increased stiffness and reduced active force response proximally. Corrected rabbits had reduced but significant medial thickening, endothelial dysfunction, and stiffening limited to the proximal region despite 12 weeks of alleviated systolic and mean BP (~4 human years) after the suture dissolved. Proximal arteries of CoA and corrected groups demonstrated increased non-muscle myosin expression and decreased myosin heavy chain expression, and this dedifferentiation may influence vascular remodeling and aortic stiffening. CFD analysis of untreated CoA rabbits demonstrated significantly reduced WSS proximal to CoA and markedly elevated WSS distally due to the presence of a stenotic velocity jet. Results from corrected rabbits indicate the velocity jet may have persistent effects on hemodynamics, as WSS remained significantly reduced. These hemodynamic and morphological observations are consistent with alterations in human patients.

Using these coupled imaging and experimental results, we may determine changes in structure and function specific to CoA and correction and how they are influenced by hemodynamics and vascular biomechanics. We are now poised to augment clinical treatment of CoA through several methods, including investigation of specific cellular mechanisms causing morbidity in CoA and the development of therapies to improve endothelial function and restore vascular stiffness.

ACKNOWLEDGMENTS

Arjun Menon

This work is dedicated to my parents, Rajan and Vatsala. In my lifetime I will never be able to fully repay them for the time, dedication, and compassion they have selflessly given me over the past 28 years. I only hope that this work will build towards something that they can look back on with pride.

I also wish to extend my sincere gratitude to my graduate advisor and mentor, Dr. LaDisa. Since joining the lab in the fall of 2007, I have had the good fortune of learning a wide variety of tools in biomedical engineering with his guidance. In our numerous meetings and discussions over the years, I have learned a great deal from him about analytical thinking and problem solving that I know will benefit me greatly in my future pursuits. Beyond technical advice, Dr. LaDisa's work ethic, relentless curiosity, internal motivation, and consideration for others has been an inspiration during my graduate studies that will continue throughout my career.

I sincerely appreciate the time and effort of my committee members, Dr. Audi, Dr. Toth, Dr. Samyn, and Dr. Eddinger in preparing this dissertation, as this work would not have been possible without their expertise and guidance over the years. I especially would like to thank Dr. Toth and Eddinger for their role in our extensive collaborations over the past few years. Dr. Toth has kindly accommodated my experimental schedules and allowed me use of his lab and materials to perform histological experiments, for which I am very grateful. In addition, Dr. Toth has always been willing to offer technical advice and guidance whenever he gets a chance which has helped me learn a great deal

about biomaterials. Similarly I have thoroughly enjoyed my time collaborating with Dr. Eddinger in the biological sciences department. I began my graduate studies with very little knowledge of smooth muscle mechanics, however with the help and guidance of Dr. Eddinger I gradually began to take a more active role in vascular function experiments. In addition to technical expertise offered by Dr. Eddinger in designing the myograph experiments for the current study, he has always set aside time for me to ask questions and provide a unique biological insight into biomedical engineering that has vastly expanded my perspective of the field. The quality of this work is largely attributed to the time and effort put forth by Drs. Toth and Eddinger, and I hope that I can begin to repay their efforts with continued publications associated with the current project. I would like to extend my thanks to Dr. Audi for his help in understanding mathematical models and technical writing advice. I hope that this work is part of continued collaborations with him in the cardiopulmonary rehab center. I sincerely appreciate the role of Dr. Samyn in this work, as it has been invaluable to have the perspective of a pediatric clinician to understand what issues are faced in clinical treatment of cardiovascular disease. I hope that collaborations between Marquette and the Children's Hospital of Wisconsin will continue to advance biomedical research.

This work is largely dependent on the success of the animal model, and several people have been instrumental in this regard. Dr. LaDisa provided the inspiration and creation of the model as well as execution of many complex surgical procedures. I also wish to thank Hongfeng Wang from the CVTEC lab for his help in the surgeries and painstakingly careful excision of arteries from the rabbits. Hongfeng often worked around his very busy schedule to allow us to carry out rabbit experiments and I appreciate that. I

also appreciate the time and effort of Dr. Eric Jensen, who provided crucial assistance in the rabbit model and expert insight as a veterinarian. I wish to thank John Tessmer and David Schwabe in the Department of Anesthesiology at the Medical College of Wisconsin for their technical assistance.

I would like to recognize Dr. Kristina Ropella for her generous support in offering me a GAANN fellowship for the past 3 years of my graduate studies. The funding source of the fellowship allowed me considerable peace of mind to focus on research work, as well as exposing me to teaching experiences as an assistant for BIEN 3300: Signals and Systems under both Dr. Gilat-Schmit and Dr. Schmit.

In addition to Hongfeng Wang, I want to thank my other friends and colleagues in the CVTEC lab: David Wendell, Timothy Gundert, Ronak Dholakia, Dr. Laura Ellwein, Sung Kwon, Sara Nomeland, DJ Quam, and Andrew Williams. Over the past four years I have benefited from your helpful advice regarding a variety of topics related to research and certainly have enjoyed our time spent together as friends. I also wish to thank Dr. Sharath Chedella in the biomaterials lab for his accommodation and help with histology during his time as a technician.

Lastly, I would like to acknowledge the support of my brother Manas who continues to be an inspiration for me, and most notably, April Breyer.

TABLE OF CONTENTS

LIST OF TABLES

LIST OF FIGURES

COMMON ABBREVIATIONS & ACRONYMS

ACH = Acetylcholine

BP = Blood pressure

CFD = computational fluid dynamics

CoA = Coarctation of the aorta

dAo = Descending aorta

IEL/EEL = Internal/External elastic lamina

IMT = Intimal Medial Thickness

MHC = Myosin heavy chain

MIP= Maximum intensity projection

MRA = Magnetic Resonance Angiography

MRI = Magnetic Resonance Imaging

NM = Non muscle

NO = Nitric oxide

OSI = Oscillatory shear index

PC-MRI = Phase Contrast Magnetic Resonance Imaging

PE = Phenylephrine

PSS = Physiological saline solution

RCCA/LCCA = Right/Left common carotid artery

RSA/LSA = Right/Left subclavian artery

SM = Smooth muscle

SMC = smooth muscle cell

SNP = Sodium nitroprusside

TAC = total arterial compliance

TAWSS = time-averaged wall shear stress

WSS = wall shear stress

CHAPTER 1: SPECIFIC AIMS

Coarctation of the aorta (CoA) is a congenital heart defect characterized by a severe stenosis in the proximal descending thoracic aorta. It currently represents 8-11% of congenital defects, affecting 3,000 to 4,000 newborns annually in the United States [7]. Surgical intervention, most commonly through resection with end-to-end anastomosis, can alleviate the blood pressure (BP) gradient and post-operative survival outcomes have improved dramatically as a result. However long-term evaluations of surgically repaired patients reveal a decreased life expectancy due to substantial residual morbidity in the form of early-onset coronary artery disease, hypertension, and aneurysm formation [8, 9], challenging the notion of CoA as a simple disease. While specific mechanisms remain elusive, early research from O'Rourke and Cartmill suggested that nearly all morbidity can be explained on the basis of altered hemodynamics and vascular biomechanics [10] in the thoracic aorta and its branches.

Computational fluid dynamics (CFD) is a simulation tool that enables detailed spatiotemporal quantification of mechanical forces based on magnetic resonance imaging (MRI) and BP data. Using CFD in concert with imaging data, a patient-specific vascular region of interest can be modeled for investigation of cardiovascular disease susceptibility based on regional and local alterations in hemodynamics and vascular biomechanics. Studies by our group and others [11-14] have shown alterations in hemodynamic indices and blood flow patterns in the thoracic aorta occurring in patients following CoA repair as compared to healthy age-matched controls. Importantly, changes in BP and wall shear stress (WSS) in conduit vessels may influence structural remodeling, active and resting vascular contractility, and vasorelaxation in a coordinated manner [15-17]. Collectively these studies suggest that CoA may impart changes in

hemodynamics and vascular biomechanics that are not fully corrected with surgical repair. These alterations may influence the structure and function of the associated vasculature, thereby increasing the likelihood of residual cardiovascular morbidities.

The current investigation used an established experimental model that mimics clinical CoA as well as morphology observed after end-to-end anastomosis repair to test the hypothesis that despite alleviating deleterious BP gradients and vascular morphology present in CoA, altered indices of hemodynamics and biomechanics persist, leading to sites of vascular remodeling, endothelial dysfunction, and altered contractility. This hypothesis was tested using the following specific aims:

SPECIFIC AIM #1: Quantify alterations in hemodynamic and vascular biomechanics indices including blood flow velocity, WSS, oscillatory shear index (OSI), and cyclic strain as surrogates of morbidity in a clinically representative rabbit model of aortic coarctation and repair.

Approach: Randomly assign 10 week old, ~1 kg rabbits (~equivalent to 9 human years) to one of three experimental groups: 1:CoA with silk suture replicating untreated coarctation (CoA); 2: CoA with Vicryl suture that dissolves over 8-10 weeks to mimic surgical resection and end-to-end anastomosis (corrected); and 3: non-surgical control. All rabbits then undergo MRI at 32 weeks of age to obtain vascular anatomy and phase contrast (PC-MRI) flow data for use with CFD simulations. Intravascular BP measurements are then collected above and below the coarctation region and CFD simulations are conducted. Hemodynamic and vascular biomechanics indices of interest mentioned above are then quantified from converged CFD simulation results.

SPECIFIC AIM #2: Compare structural changes in the arterial wall accompanying coarctation-induced alterations in hemodynamics and vascular biomechanics using histological techniques.

Approach: Medial thickness and remodeling are quantified using arterial segments excised from the carotid artery, thoracic aorta proximal to coarctation, descending thoracic aorta distal to coarctation, and femoral artery using established histological and immunohistochemistry techniques and compared to spatial distributions of WSS, OSI, BP, and cyclic strain from CFD simulations.

SPECIFIC AIM #3: Quantify the endothelium-dependent and contractile responses to agents using established myograph techniques for arterial segments in regions of altered hemodynamics and vascular biomechanics proximal and distal to experimental coarctation as compared to control rabbits.

Approach: Functional vascular response to contractile and vasorelaxation agonists are quantified for arterial segments excised from the regions from the thoracic aorta mentioned in Aim 2 using established myograph techniques and compared to spatial distributions of BP, as well as WSS, OSI, and cyclic strain from CFD simulations.

CHAPTER 2: BACKGROUND

2.1 Coarctation of the aorta

Congenital heart disease is a major health problem, affecting more than 30,000 infants per year in the United States alone. CoA is currently the second most common congenital defect, occurring in 8-12% of these births annually [18], and more commonly in males than females (4:1). The disease is characterized by a severe stenosis in the proximal descending thoracic aorta **(Figure 1)**. CoA most commonly occurs distal to the left subclavian artery and opposite the ductus arteriosus, a vessel present during fetal development containing smooth muscle cells which are thought to cause partial ductal closure immediately after birth [19].

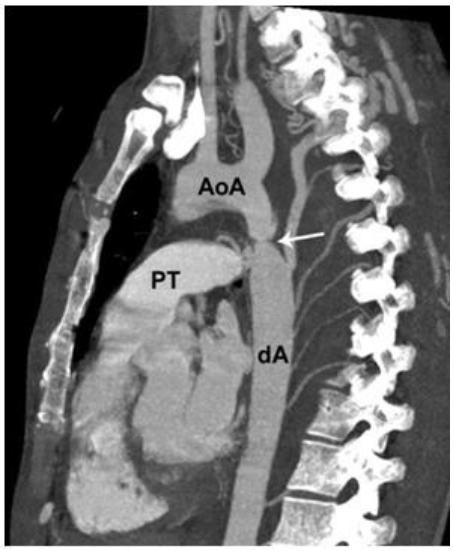

Figure 1. Transverse view of untreated aortic coarctation, with a stenosis present in the proximal descending thoracic aorta (white arrow). AoA = Ascending aortic arch, dA = descending aorta, PT = pulmonary trunk. (Adapted from Leschka et al, [1])

CoA is often associated with other cardiovascular defects including ventricular septal defect, aortic arch hypoplasia, hypoplastic left heart syndrome, and most

commonly bicuspid aortic valve [20]. In addition 30% of patients diagnosed with the chromosomal disorder Turner's syndrome also present with CoA [21].

Together CoA and its associated abnormalities impede the conduit and cushioning functions of aorta, which respectively include the large arteries that rapidly deliver oxygenated blood for distribution to tissues and organs with minimal pressure loss, as well as the pronounced capacitance that is the hallmark of the thoracic aorta and contains approximately 60% of the total arterial capacitance [4]. While these changes may have several consequences, the most commonly reported involves the development of a BP gradient across the CoA, an elevation in pulse BP proximally, and a drop in pulse BP distal to the CoA. As such, putative clinical guidelines for treatment of CoA includes a mean BP gradient of ≥20 mmHg between the upper and lower extremities [22]. The source of symptoms of CoA are unclear, but often associated with increased BP in the proximal vasculature and are may include hypertension, shortness of breath, exercise fatigue, headaches, nosebleeds, and leg pains associated with claudication [23].

2.2 Motivation: Residual morbidity despite successful surgical repair

Treatments for coarctation have developed considerably over the years and include both catheter-based and surgical approaches. Recent developments in catheter-based techniques include the use of balloon dilation for CoA as early as 1982 and stent implantation in the early 1990s [24, 25]. While these catheter-based techniques offer reduced hospitalization time and costs, the need for re-intervention and increased likelihood for re-coarctation due to somatic growth associated with these techniques are

potential limitations to their use in children [26]. In contrast, surgical repair of CoA was first performed in 1944 and remains the treatment of choice in children <1 year old [27, 28]. Evidence of long-term aneurysm risks (as high as 23%) following techniques involving synthetic patch aortoplasty lead to the preference of resection and end-to-end anastomosis techniques and aneurysm risk has decreased to approximately 5-8% as a result [27], with aneurysm risk in the general population reported to be between 1.4-4.0% [29]. This procedure involves excision of the coarctation using an incision along the underside of the aortic arch and posterior wall of the descending aorta. Aortic tissue is then sutured, or anastomosed, together [30-32] **(Figure 2)**. However a high incidence (24-41%) of recoarctation is reported [33].

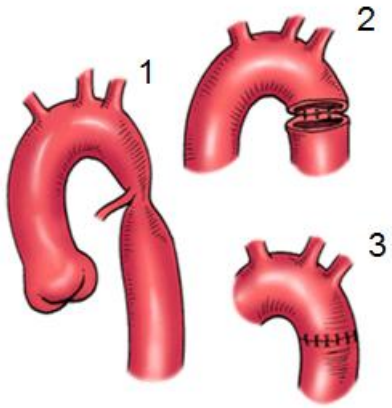

Figure 2. Schematic of resection and end-to-end anastomosis repair. The region of the coarctation is resected and the vessel ends are joined using circumferential sutures perpendicular to the flow domain. (Adapted from Thumbnail Guide to Congenital Heart Disease [2])

Subsequent research involving this intervention found recoarctation rates were reduced from 41% to 3.6 % when a longer anastomosis is used. This method, known as extended end-to-end anastomosis **(Figure 3)**, uses a suture line beveled (oblique) to the primary direction of blood flow and simultaneously addresses posterior arch hypoplasia [32].

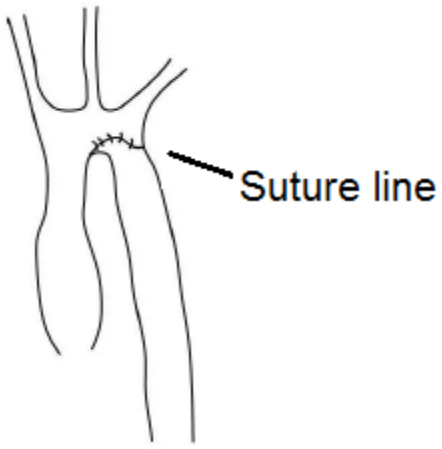

Figure 3. Depiction of extended end-to-end anastomosis repair of CoA. This technique reduces the chance of re-coarctation by using a larger region of anastomosis than traditional end-to-end anastomosis repair. (Adapted from Gargiulo et al, 2007 [3])

Despite postoperative BP restoration, studies continue to show significant residual morbidity including coronary artery disease, resting or exercise-induced hypertension, cerebral aneurysms, and stroke in patients after repair by any means. The natural history of CoA documented in the literature therefore suggests life expectancy are decades less than that of the average population despite treatment, challenging the notion of CoA as a simple pathology [8, 9].

2.3 The possible influence of hemodynamic and vascular biomechanics indices on CoA morbidity

Mechanical forces influence the development and progression of cardiovascular disease. Alterations in arterial structure are common in vascular diseases and are thought to occur primarily by vascular remodeling, defined as any change in the vessel geometry

in response to hemodynamic and vascular biomechanical stimuli [34, 35]. Hemodynamics is defined by forces that govern blood flow and include blood pressure and derivatives of velocity. Biomechanics concerns the effects produced by internal and external forces acting on the vascular system (in particular structure and function). For the purposes of this study, vascular biomechanics include parameters of cyclic strain, medial thickness, and vascular relaxation and constriction. While the source of these structural alterations are not fully understood, research illustrating the role of WSS in endothelial nitric oxide (NO) release in vasodilatation and modulation of wall thickness through cell turnover (proliferation and apoptosis) has elucidated the role of WSS in myogenic regulation [15, 16, 36]. Vessels respond to an increase in WSS associated with concomitant increases in blood flow by increasing production of NO which subsequently dilates the vessel, increasing lumen size and thus returning WSS and eventually NO production back to a normal and preferred range of operating values. This homeostatic response of WSS is essential for certain processes including exercise, where local increases in oxygen demand occur which require increased blood flow [37]. However, if WSS alterations are sustained, changes in arterial medial thickness can occur through cell turnover and reorganization in the dilated (or constricted, in the case of reduced WSS) state such that the arterial wall becomes re-established at a diameter and thickness that differs from that associated with the preferred range of operating values. Although blood flow and thus WSS are returned to near normal values in cases of corrected CoA, local alterations persist [14] and may cause persistent alterations to vascular structure and function associated with CoA morbidity [36].

This homeostatic response can be accordingly applied to changes in tensile stress, wherein arteries with elastic properties respond to changes in BP by altering luminal radius in a manner that maintains wall tensile stress at normal levels. Assuming BP returns to normal soon thereafter, wall tensile stress is reduced and the vessel regains its original caliber. If the BP increase is sustained however, compensatory vascular remodeling may occur to increase medial thickness in the dilated state, thus restoring tensile stress to its preferred homeostatic level. This may serve to reset vessel caliber or thickness at a level where indices of vascular structure, biomechanics, and function are altered and cannot return to their prior functional levels despite restoration of BP due to changes in vascular smooth muscle content and organization.

The specific mechanisms associated with altered arterial wall structure and function as a result of sustained changes to mechanical forces are not fully defined and may be due to both cellular and acellular changes in the associated vasculature. Acellular changes causing increased wall stiffness, medial thickness, and altered expression of contractile and structural proteins can limit changes in BP by offsetting the smooth muscle response. These changes may impart the vasculature with a high residual wall stress which serves to reduce relaxation capability and exaggerate exercise induced increases in BP. Alternatively, mechanisms of morbidity may be rooted in cellular mechanisms involving impairment of vasodilation through endothelial NO release, or reactive molecules present due to the applied hemodynamic/tensile stresses [38, 39]. Together these findings suggest that sustained alterations to hemodynamic and vascular biomechanics indices as a result of CoA may cause altered structural reorganization along with mechanical forces that are not fully alleviated by the removal of the CoA stenosis.

These alterations may contribute to the high rates of residual morbidity observed following CoA repair. **Table 1** shows an illustration of how alterations to these parameters of hemodynamics and biomechanics may relate to an increased potential of morbidity.

Hemodynamic Parameter	Applicable Source of Morbidity and Mortality
Indices of WSS	Stroke, CAD, Aneurysm Formation
Blood Pressure	Hypertension, Aneurysm Formation
Biomechanics Parameter	**Applicable Source of Morbidity and Mortality**
Cyclic strain	Hypertension, Aneurysm Formation
Medial thickness	Hypertension, CAD
Vascular relaxation and constriction	Hypertension, CAD, Stroke, Aneurysm Formation

Table 1. Description of how alterations to parameters of hemodynamic and vascular biomechanics may serve as surrogates for the potential of morbidity and mortality reflective of the major causes of death in post-repair CoA patients.

2.4 Sustained hemodynamic alterations influence vascular function

In addition to relaxation previously discussed, endothelial cells (ECs) also mediate inflammatory and thrombogenic responses through the selective release of coagulants, adhesion molecules, and cytokines [15, 40, 41]. Dynamic physiologic response of the endothelium is essential. However, persistent or deleterious changes in hemodynamics and vascular biomechanics can lead to a state of impaired endothelial release of NO and vasodilation, known as “endothelial dysfunction”. Endothelial dysfunction has been associated in the development of atherosclerosis and thrombosis in addition to reduced vasodilatory capacity [42], but studies have only recently identified specific mechanisms in this process [40, 43, 44]. As a result, endothelial dysfunction may

connect altered functional experimental results in pathophysiological conditions with appropriate surrogates for morbidity. Early-onset coronary artery disease in particular has been associated with endothelial dysfunction [27], and thus observation of dysfunction in untreated and corrected CoA may suggest an increased risk of morbidity in these groups.

Sustained alterations in WSS and BP may also serve to alter vascular contractility in a coordinated manner. The classic myogenic response involves the reduction of vessel diameter in response to an increase in BP, which is thought to be caused by an increase in cyclic stretch on smooth muscle cells (SMCs). The relative contributions of active and resting force on the regulation of arterial diameter depend on the dynamic interaction between resting tension, diameter, and the magnitude of active tension [45]. It is likely that similar mechanisms are involved in the vascular response to deleterious increases in BP. As previously discussed, the arterial vasculature is believed to maintain wall tensile stress homeostasis by structural and regulatory changes, and these may have direct consequences on the resting and active contractile components of smooth muscle. Changes in vessel stiffness due to hypertension occur primarily as a result of increased pulse BP and have been directly associated with increased risk of coronary artery disease and atherosclerosis [46-49]. Active force components may reflect deleterious changes as well [50, 51] as changes in medial thickness, extracellular matrix deposition not discussed in detail here, and endothelial function may result in altered active force which is indicative of atherogenic changes in the conduit vessels.

2.5 Review of abnormal hemodynamics and vascular biomechanics in CoA literature

Surgical correction of CoA suggests that removal of the stenosis should alleviate hypertension proximal to the site. However studies as early as 1971 [10, 52, 53] applied the theory of vascular impedance and wave reflection to describe the effect that large artery diseases such as CoA have on the cushioning function (i.e. capacitance) of the arterial system. Vascular input impedance is defined as pulsatile resistance, ratio of oscillatory BP and flow, at any particular region of the arterial vasculature. Input impedance completely describes the arterial system and relevant physiological parameters of capacitance, systemic vascular resistance, and characteristic impedance can be derived from its spectra [54, 55] (**Figure 4**). Arterial capacitance is classically defined as the relationship between blood volume in a segment of vasculature and the pressure distending on the vascular walls, and thus provides an index of elasticity of the large arteries such as the thoracic aorta, an important risk factor for cardiovascular disease. Systemic resistance, or total vascular resistance, refers to the resistance to blood flow offered by the entire systemic vasculature and is primarily determined by arterioles [54]. Characteristic impedance represents the resistance, compliance, and inertance of the proximal artery of interest.

CoA causes a marked reduction in proximal aortic compliance, leading to increased pulse and systolic BP during rest. These alterations may affect diastolic BP and thus coronary artery perfusion providing a possible explanation for the high rates of heart failure seen in these patients.

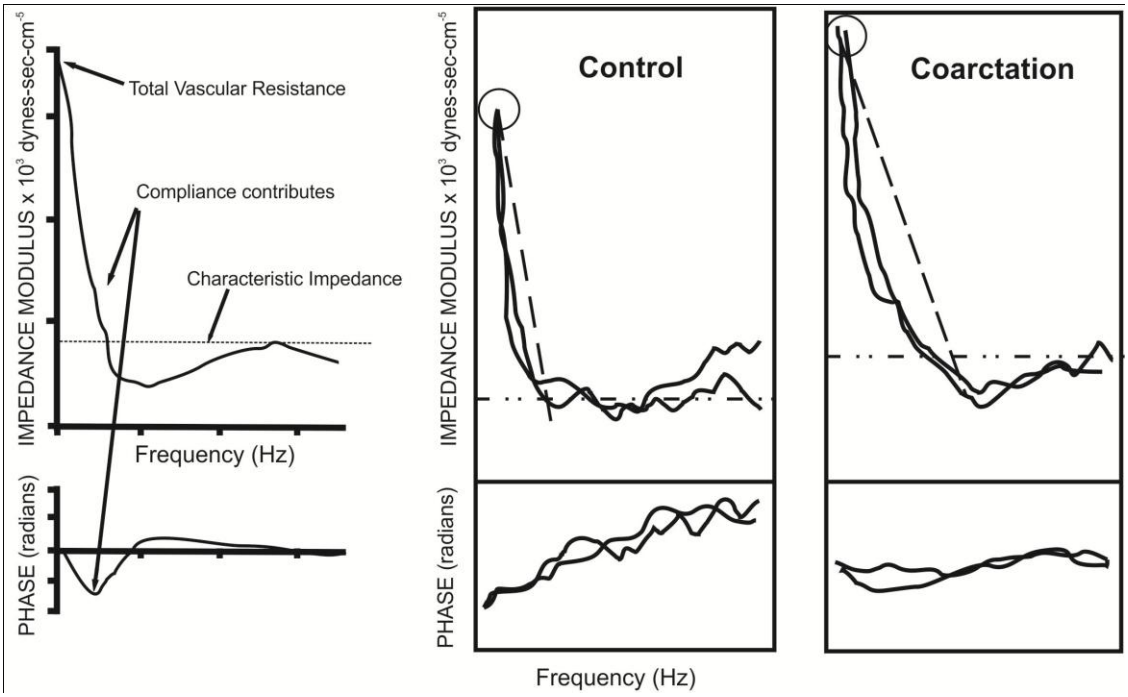

Figure 4. Representative input impedance spectra with relevant physiological indices labeled (left). Patient data from control and coarctation subjects reveal differences due to coarctation observable on the impedance spectra (right).Total vascular resistance and characteristic impedance are increased in CoA, highlighted by circles and dash-dotted lines respectively. Dashed lines indicate reduced compliance in CoA through a less negative impedance modulus slope. (Adapted from Nichols and O'Rourke, 1971, [4]).

To counteract the reduced blood flow to the descending aorta in cases of untreated CoA, it is common for collateral vessels to develop [56]. Collateral vessels commonly originate from the left subclavian artery and create anastomoses to the intercostal circulation, thus restoring conduit blood flow function. The long and tortuous nature of collateral vessels unfortunately still impedes the cardiovascular system's ability to transmit pressure pulses, thus impairing the cushioning function of the thoracic aorta.

Recently, studies using multidirectional flow analysis for detailed investigation of hemodynamics in the human thoracic aorta [57] found healthy young adults demonstrate

low WSS and elevated OSI occurring in a rotating pattern progressing down the descending aorta. A subsequent study of middle-aged adults with preexisting plaques had similar WSS and OSI patterns which correlated with areas of atherosclerotic plaque. CoA patients following end-to-end anastomosis repair demonstrate localized alterations to WSS compared to age-matched controls, and these findings are in agreement with 4D MRI flow studies illustrating altered blood flow patterns in the aorta associated with vascular remodeling and aneurysm risk following coarctation repair [58, 59].

Together, these observations were able to establish a connection to altered hemodynamics and vascular biomechanics which may influence morbidity in a manner reflective of the major causes of death observed in treated CoA patients. Application of these observations to the current status of treatment suggests that surgical repair of CoA may not address flow disturbances and mechanical stresses in the aorta that may influence residual morbidity in these patients.

2.6 Structural alterations following CoA correction

To date several clinical studies have investigated the structure of arterial conduit vessels using post-repair CoA patients to determine possible factors of residual morbidity [60-62]. Using non-invasive B-mode ultrasound imaging, arterial intimal-medial thickness (IMT) and subsequent changes can be determined at important locations in the vasculature. IMT is influenced by local hemodynamics and vascular biomechanic indices and has been used as a surrogate end point for cardiovascular disease risk [63], particularly atherosclerosis. Prospective studies have shown that an increase in IMT is

associated with increased relative risk of heart failure, while decreased IMT is associated with a decreased risk. Clinical evaluations of IMT were performed in carotid and femoral arteries of postcoarctectomy patients and compared to age-matched, normotensive, healthy volunteers [60]. Interestingly, results demonstrated IMT was increased in young patients (ages 24-30) after successful repair of CoA compared to controls, particularly in the carotid arteries. While early surgical intervention (defined as <1 year) was demonstrated to have a beneficial effect on the distal vasculature, carotid arteries still demonstrated increased IMT despite repair as early as neonatal age. These results suggested for the first time that structural abnormalities are present despite successful surgical intervention in CoA and may indicate an increased risk of cardiovascular complications. The specific mechanisms causing these structural alterations are not precisely known, but thought to be a result of either the damaging effects of elevated arterial BP in the proximal arteries or an innate developmental defect present in the CoA pathology [62, 64].

2.7 Functional alterations following CoA correction

Expanding on these findings of altered structure, several studies [60, 65, 66] investigated functional properties of the conduit arteries in post-repair CoA patients using forearm blood flow measured through gauge-strain plethysmography. Briefly, the change in diameter of the brachial artery was determined after producing a brief ischemia in the forearm through a suprasystolic BP cuff. Deflation of the BP cuff causes reactive hyperemia which produces a WSS stimulus inducing endothelial release of NO and

vasodilation [67]. While it does not provide an exact measure of functionality, this approach known as flow-mediated dilatation has been established to reflect endothelial function of the brachial artery and correlates with coronary endothelial function [68]. Results from the clinical evaluations revealed that despite no differences in systolic BP, endothelial vasodilatory function was impaired in repaired patients (ages 29-33) at 10-15 year follow up compared to healthy controls, and that the severity of dysfunction was related to age at surgery [65, 69]. While endothelial dysfunction provides evidence of altered vasodilatory properties, it also indicates a compromised anti-inflammatory capacity of the endothelium. This was subsequently confirmed in follow up studies of post-repair CoA patients [70], and further supports a possible explanation for the high incidence of coronary artery disease in these patients.

Together these findings suggest that despite alleviation of the BP gradient and vessel geometry, post-repair normotensive patients show morphological and functional changes in the conduit vasculature that may influence and predict future morbidities leading to reduced life expectancy.

2.8 Computational Fluid Dynamics

Recent advancements in computational modeling have led to the implementation of CFD as a tool to investigate altered hemodynamics resulting from vascular diseases. Previous CFD studies were often conducted assuming a constant BP or velocity profile at the vessel outlets, but arterial blood flow is strongly influenced by the distal arteriolar bed. The methods used for the current investigation therefore allow accurate

representation of the systemic vasculature by including an estimate of the time-varying resistance that occurs in vivo through the use of 3-element Windkessel models at the computational domain outlets [71]. Subject-specific data including BP and distribution of flow to the branch arteries of the aorta are used to determine these outlet boundary conditions, resulting in CFD models with physiologically representative flow and BP distributions. As mentioned in the introduction, several hemodynamic indices are of particular interest when studying morbidity in the setting of CoA including blood flow velocity, time-averaged wall shear stress (TAWSS), and OSI. The analysis of vascular biomechanics includes indices of cyclic strain, distensibility, and stiffness. The detailed calculations associated with these indices are discussed in more detail in the methods section in chapter 3.

Clinical imaging data and novel computational modeling tools may be combined for detailed analysis of CoA induced alterations to hemodynamics and vascular biomechanics using CFD. While CFD studies on human patients with CoA are still in their infancy, work in our laboratory has identified localized differences in hemodynamic indices in corrected CoA using CFD which are consistent with 3D and 4D MRI imaging studies detailing velocity distributions as mentioned previously [57, 72, 73]. However the direct link between altered indices and changes in the vasculature is difficult to establish due to the limited number and heterogeneity of patients at any given center.

2.9 Clinical significance

An *in vivo* model was used to quantify hemodynamic and vascular biomechanics indices seen in untreated and corrected CoA, and subsequently their impact on vascular histology and function. Furthermore, it aimed to reproduce changes in these indices observed in untreated CoA distinctly from those occurring after correction of BP and morphology in a manner similar to resection and end-to-end anastomosis, currently the most common method of intervention in congenital CoA [3, 32]. The collective results may improve our clinical understanding of the substantial morbidity present in CoA patients despite successful repair. Identification of changes in hemodynamics, vascular biomechanics, structure, and function caused specifically by untreated CoA and correction may augment current clinical intervention techniques for CoA, which currently does not consider these phenomena. Identification of specific changes caused specifically by CoA and correction may allow optimization of surgical techniques such that indices of hemodynamics in post-correction CoA patients are restored as closely as possible to those of healthy patients. In addition, implementation of the current model may allow future studies to identify specific cellular mechanisms caused by altered hemodynamics and vascular biomechanics which directly relate to deleterious structural and functional changes in corrected CoA. Identification of specific cellular pathways in CoA pathophysiology increases the feasibility of applying appropriate drugs (inhibitors) which may alleviate cardiovascular morbidities, thus dramatically improving patient outcomes in CoA.

CHAPTER 3: METHODS COMMON TO ALL AIMS

3.1 Experimental protocol

All experimental procedures were approved by the Animal Care and Use Committee of Marquette University and the Medical College of Wisconsin (IACUC #: Marquette AR-223, MCW AUA0001175). In addition, all conformed to the "Guiding Principles in the Care and Use of Animals" of the American Physiological Society and the *Guide for the Care and Use of Laboratory Animals*. Following a 72 hour acclimation period, male New Zealand white rabbits ~10 weeks old were randomly assigned to undergo either descending thoracic aortic coarctation with Vicryl (dissolvable) suture (n=7, corrected group), coarctation with silk suture (permanent; n=7, CoA group), or non-operation control (n=7, control group). Rabbits in surgical groups were given 40 mg/kg of ketamine and 5 mg/kg of xylazine intramuscularly, and underwent endotracheal intubation, where anesthesia is maintained by 1-2% isofluroane administered through ventilator (Harvard Apparatus, Holliston, Massachusetts). The antibiotic cefazolin (20 mg/kg) was administered at least 1 hour prior to the first incision, and fur above the 3-8th intercostals spaces was shaved and prepped for sterile surgery using antiseptic solution. CoA in the mid-descending thoracic aorta was induced through a left thoracotomy between the 5th and 6th intercostal arteries. Muscular and tissue layers were carefully and gently navigated to expose the descending proximal thoracic aorta (dAo). 3-0 silk (CoA group) or Vicryl (corrected group) ligatures were then tied around the aorta against a 16 gauge (1.6 mm) stainless steel wire. Removal of the wire resulted in a CoA of repeatable and known size causing a 15-30 mmHg BP gradient across the CoA at harvest as verified by previous research [74, 75]. Notably, "clinical significance" for CoA is commonly defined as a BP gradient of ≥20 mmHg at rest [22, 76] and thus a gradient of 20 mmHg

was targeted using this technique. To evacuate the pneumothorax caused by induction of CoA, a flexible tube was inserted into the pleural cavity, secured by a purse-string suture, and the chest was closed in layers. Suction was applied to the tube using a syringe and 3-way stopcock, and the tube was removed 1.5 hours after surgery when the rabbit was sternal and no additional air or fluid could be extracted.

3.2 Monitoring

Extensive monitoring was conducted during all experimental procedures using quantitative criteria with preferred operating ranges for oxygen saturation, heart and respiratory rate, temperature, mucous membrane color and capillary refill time. Monitoring was conducted at ten-minute intervals during procedures, as well as for 4-5 hours after surgery and 2-3 hours after the MRI procedures discussed below. Buprenorphine (0.025 mg/kg SQ) and cefazolin (20 mg/kg SQ) were administered for postoperative analgesia and antibiotic prophylaxis, respectively, for two days after surgery. Qualitative criteria such as attitude, appetite, urination, defecation, vomiting and appearance of the surgical site were recorded along with the clinical measures mentioned above 2, 3, 5, 10 and 14 days after surgery and periodically thereafter. Furosemide was also administered for two weeks post-op (4 mg/kg SQ BID) and as needed thereafter to treat any ensuing respiratory symptoms due to pulmonary edema. Rabbits were provided with enrichment in 4x8 ft runs.

3.3 Magnetic Resonance Imaging

Rabbits underwent anatomic and phase contrast MRI for use with CFD modeling to allow determination of cyclic vascular strain upon reaching adult size at 32-36 weeks. Rabbits were anesthetized using ketamine (22 mg/kg) and xylazine (2.5 mg/kg) and a saline filled angiocath IV inserted into the left marginal ear vein for contrast-enhanced illumination of the thoracic aorta and its branches. Cardiovascular MRI was conducted with a 3T GE Sigma Excite scanner (GE Healthcare, Waukesha, WI) in the supine, "head-first" position using a quadrature knee coil and the sequences shown in **Table 2**. To ensure adequate anesthesia, an external pulse oximeter (Nonin Medical Inc, Plymouth, MN) and a core temperature sensor approved for use in the MR environment were included. Cardiac triggering was obtained by use of a peripheral pulse oximeter attached to the right ear which provided heart rate. Two doses (0.2 mmol/kg) of gadolinium (Gd; Omniscan gadodiamide; GE Healthcare, Princeton, NJ) were prepared and loaded into the distal end of extension tubing that was connected to the angiocath IV. Additional saline-filled extension tubing was also attached to the IV and an MR-compatible pump within the scanner room. Rabbits were allowed to breathe freely throughout the imaging session. Gadolinium-enhanced magnetic resonance angiography (MRA) scans were performed at an injection rate of 2 ml/sec. Gadolinium dose was limited to 0.2 mmol/kg based on common usage of animals of similar size. Blood flow information for use with CFD was acquired using a cardiac-gated, 2D, PC-MRI sequence with through-plane velocity encoding. PC images were obtained at planes transverse to the ascending aorta (AscAo), the cervical arteries, the coarctation, and dAo.

	MRA	PC-MRI
Sequence	3D fast GRE	2D fastcard PC
TR/TE/flip angle	6.0 ms/1.7 ms/30 degrees	8.5 ms/1.7 ms/20 degrees
Slice thickness	1.2 mm	3.0 mm
Acquisition matrix (pixels)	256 x 192	256-384 x 224-256
Field of view (cm)	12 x 12	12 x 12
VENC (cm/sec)	-	80-200
Cardiac frames	-	20

Table 2. Magnetic resonance imaging parameters utilized for collection of volumetric MRA and PC-MRI flow imaging data.

3.4 Intravascular blood pressure measurements

After detailed offline analysis of MRI data, rabbits were again anesthetized for measurement of BP prior to tissue harvest. Proximal and distal aortic BP waveforms were measured simultaneously and obtained from the same model pressure transducer (Harvard Apparatus, Holliston, MA) from which waveforms were digitally recorded at 720 Hz using a computer interfaced with an analog-to-digital converter. Transducers were attached to 5 inch noncompliant fluid-filled catheters. The proximal fluid-filled catheter was inserted into the common carotid artery and tracked retrogradely to the aortic arch. The distal fluid-filled catheter was inserted into the femoral artery and tracked retrogradely to the aortoiliac bifurcation.

3.5 CFD

3.5.1. Model Creation

The three-dimensional MRA data from each rabbit was used to reconstruct the vessel geometry and contour of the thoracic vasculature. MRA imaging data was processed using specialized software to correct for any gradient nonlinearities that can cause geometric distortions within the imaging volume. Using software that facilitates volume visualization and conversion of the MRA imaging data into geometrically representative computer models, CFD representations were created for each subject imaging set. Briefly, the process of model creation involves finding the centerline path of each artery, performing segmentations to delineate the arterial wall, connecting these segments to form a representative model, and discretizing the model using a commercially available automatic mesh generator. A brief outline of the model creation process is shown in **Figure 5**.

2D segmentation techniques were used to build all models, which began at the level of the aortic sinus and included the ascending, transverse, and descending aorta terminating at the level of the diaphragm. Head and neck vessels including the right common carotid (RCCA), right subclavian artery (RSA), left common carotid (LCCA), and left subclavian artery (LSA) were included in the model. MRA volumetric data acquired as previously described was visualized for geometric modeling using eFlim (Merge Healthcare, Milwaukee, WI) software and Simvascular. Volume rendering was performed in VolView where parameters of visualization were determined and subsequent .vti files were loaded into Simvascular.

Vessel centerline paths through regions of interest were manually created through all arteries included in each CFD model. Spline points were then used to smooth the centerlines depending on the length and tortuosity of the vessel and paths were saved using unique identifiers as they act as the basic framework of the 2D model construction. For all models, 300 spline points were used to generate the path of the thoracic aorta, and 100 spline points were used for the branch vessels. The imaging data was then resampled in planes perpendicular to the centerline and the vessel lumen was segmented using manual segmentation techniques to accurately delineate the vessel boundary. All 2D segments were stored using unique identifiers for each vessel of interest. Segments were adjusted axially to avoid intersection or artificial shape changes and create geometrically representative and well defined vessels.

The set of 2D segments delineating the vessel lumen along the centerline path for each vessel of interest was lofted to form a solid model. Individual vessels were joined into a single solid model. Branch intersections were blended to create smooth transitions between vessels reflective of the native physiology. Solid model faces were defined as inflow, outflow, or wall to prescribe boundary conditions and facilitate analysis of surface properties. The solid model was then discretized into an isotropic mesh of chosen edge size [77, 78] before local adaptation of this computational mesh was performed as described in more detail below.

As detailed above, rabbits in CoA group retained a dramatic stenosis due to implantation of the CoA with permanent silk suture which resulted in a mean BP gradient of ~20 mmHg in the thoracic aorta. In order to accurately represent this gradient in the computational domain, the diameter of the stenosis was delineated from PC-MRI data

obtained at the location of the CoA. The vessel segment corresponding to the CoA was then adjusted to match this measured diameter and the measured BP gradient. CoA models were then subjected to steps typical of a traditional numerical simulation with mesh adaptation and pulsatile analysis as described below.

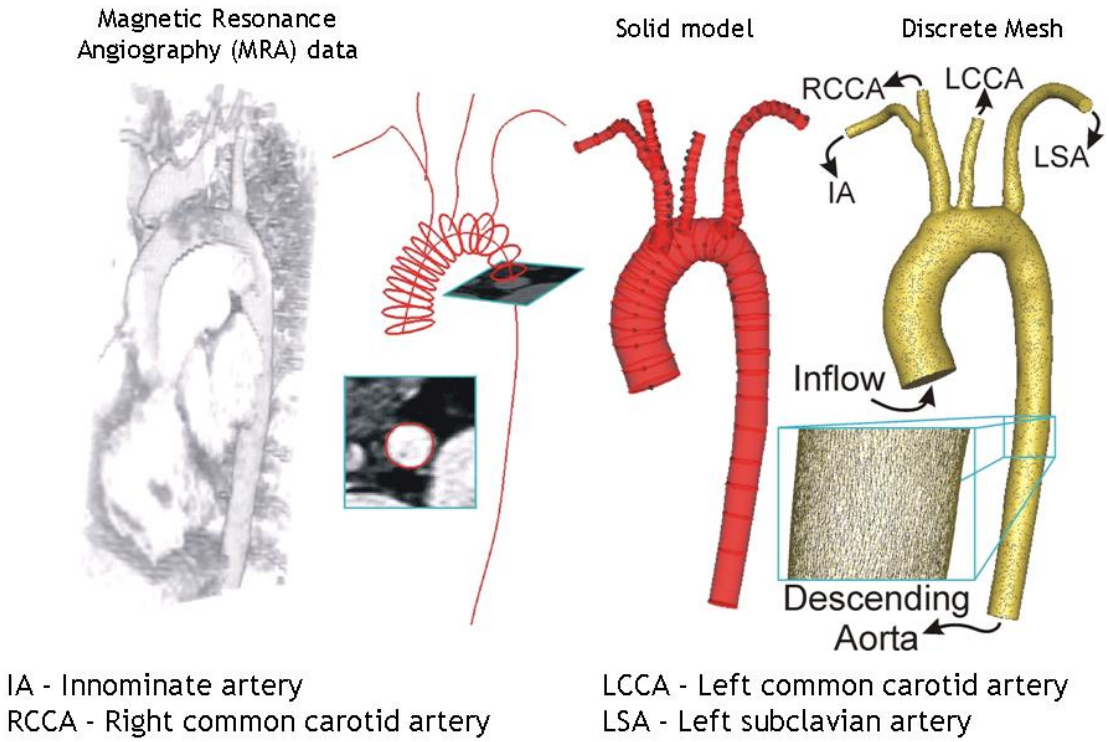

Figure 5. Overview of the process used to create CFD models using a 2D model creation process. Vessel centerlines are created from MRA data, from which vessels of interest are segmented and lofted to form the model, which is finally discretized into the mesh of chosen edge size.

3.5.2 Inlet boundary conditions

PC-MRI images were obtained orthogonal to the ascending aorta near the aortic sinus. The vessel lumen was delineated from PC-MRI images using the Simvascular software package and pixel velocity values within the segmented region were adjusted

with a second order, spatially dependent baseline correction algorithm to account for phase errors that result from gradient eddy currents. The corrected velocity was then integrated over the 2D lumen segmentation to yield an instantaneous flow rate at each of the 20 PC-MRI images. The ascending aorta waveform was then mapped to the inlet face of the CFD model using a time-varying parabolic velocity profile (**Figure 6**).

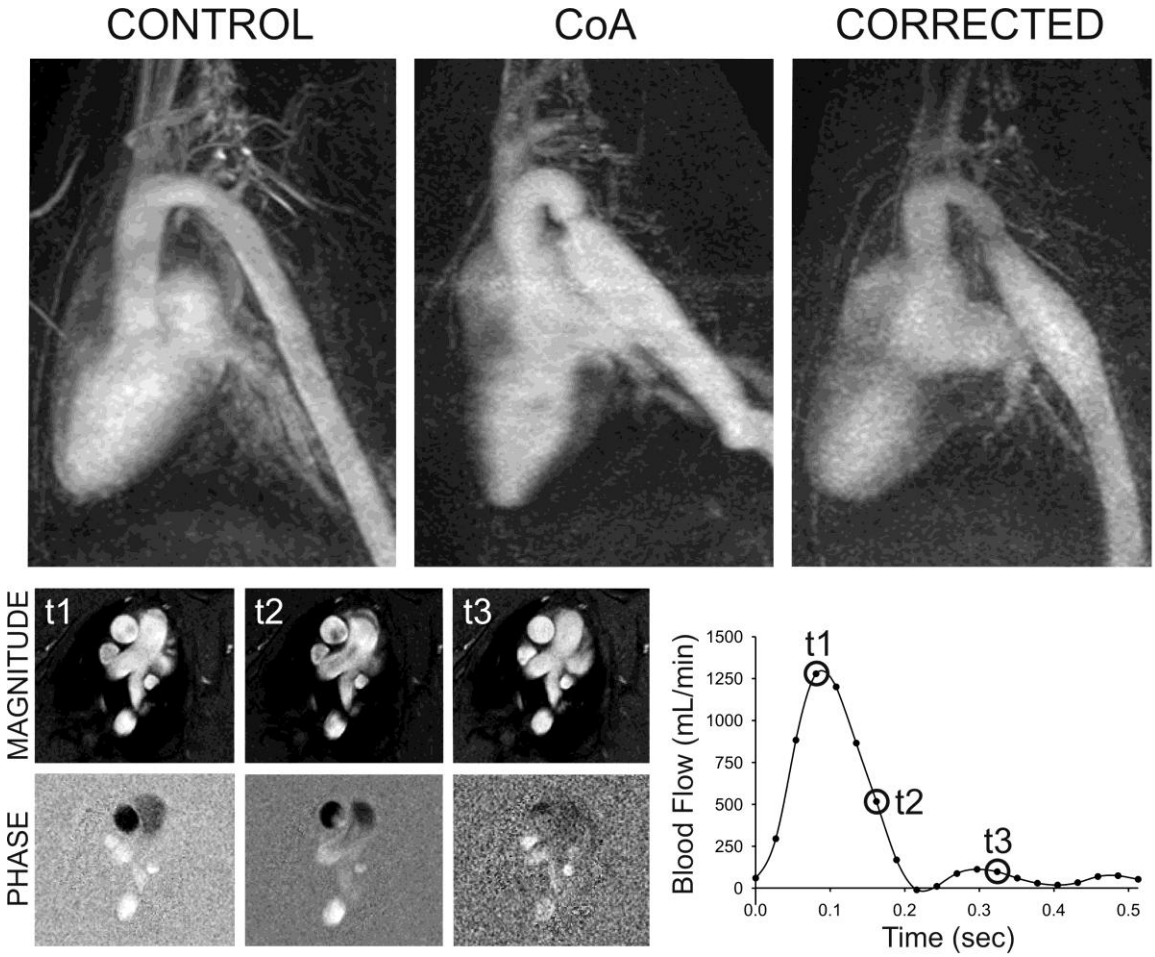

Figure 6. Representative maximum intensity projections of each experimental group from MRA data (top). Phase-contrast MRI phase and magnitude data at the ascending aorta (bottom left) used to calculate inflow waveform (bottom right) for use in CFD simulations.

3.5.3 Outflow boundary conditions

In order to create a physiologically relevant CFD model, simulation flow and BP values were matched to flow waveforms obtained at the RSA, RCCA, LCCA, and LSA along with measured BP data to prescribe outflow boundary conditions. To replicate the physiologic effect of arterial networks distal to the CFD model, 3-element Windkessel outlet boundary conditions were imposed using a coupled-multidomain method [79, 80]. This method provides an intuitive representation of the arterial tree beyond model outlets and can be described by three parameters with physiologic meaning: characteristic (regional) impedance (Rc), arterial capacitance (C), and peripheral resistance (Rp). The total arterial capacitance (TAC) for control and corrected rabbits was determined from inflow and BP measurements assuming an initial characteristic to total resistance (Rc: Rp) ratio of 6% [81], and adjusted for the CoA group according to previous literature. The TAC was then divided among the outlets according to their blood flow distributions [80]. Once the capacitance terms for each branch were assigned, the terminal resistance (Rt) was calculated from mean BP and flow measurements and distributed between the Rc and Rp parameters by adjusting the Rc:Rt ratios to replicate measured BP using the pulse pressure method [55]. These methods resulted in BP and flow waveforms similar in shape and magnitude to the clinically measured BP and PCMRI flow values respectively (**figure 7**) [82, 83].

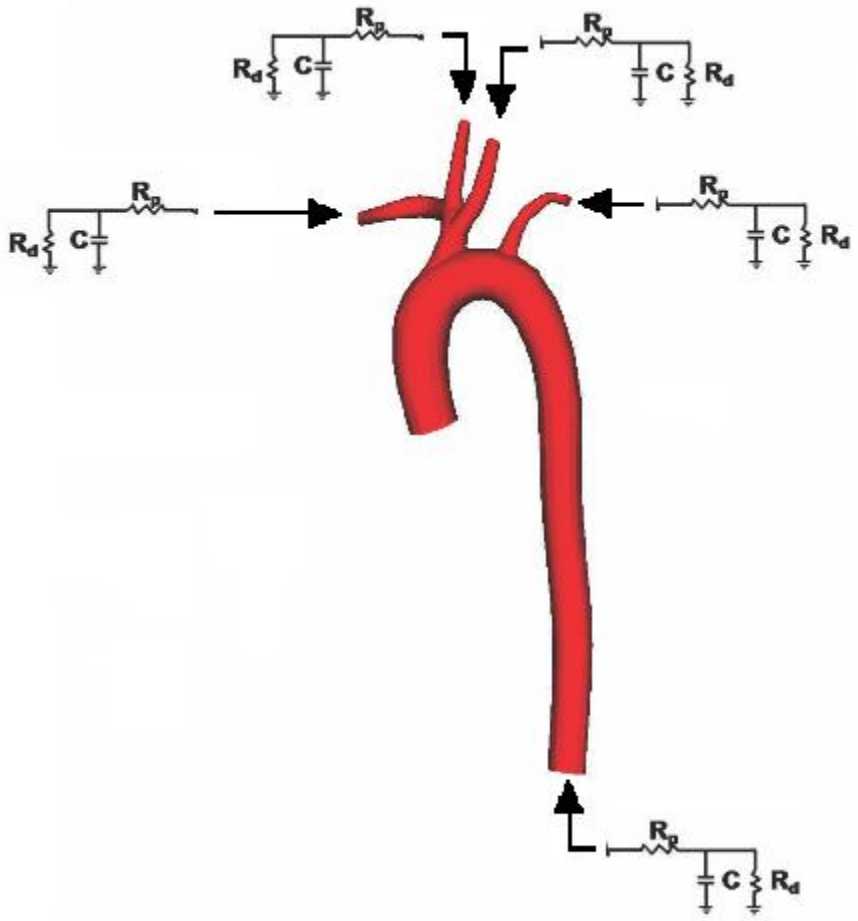

Figure 7. Representative CFD solid model with 3-element Windkessel outlet boundary conditions displayed as circuit equivalents of the impedance at each model outlet. Application of outlet boundary conditions results in pressure and flow values similar to experimental measurements.

3.5.4 Simulations

CFD models were created for 7 subjects in each of the three groups described previously: untreated CoA, corrected CoA, and control. Simulations were then performed using a novel stabilized finite element method to solve equations for the conservation of mass (continuity) and balance of fluid momentum (Navier-Stokes). Conservation of mass can be expressed mathematically as:

$$\frac{\partial \rho}{\partial t} + \frac{\partial (\rho u_x)}{\partial x} + \frac{\partial (\rho u_y)}{\partial y} + \frac{\partial (\rho u_z)}{\partial z} = 0$$

Where ρ is the fluid density and u_x, u_y, u_z are the directional x, y, and z components of the velocity vector.

The motion of incompressible fluids can be described by the governing differential equations of Navier-Stokes and can be used to represent blood flow in the fluid domain of the vessel lumen, from which the three-dimensional components of velocity (u_x, u_y, u_z) and pressure (p) can be determined. The equations can be expressed as a set of coupled non-linear partial differential equations:

$$\rho\left(\frac{\partial u_x}{\partial t} + u_x\frac{\partial u_x}{\partial x} + u_y\frac{\partial u_x}{\partial y} + u_z\frac{\partial u_x}{\partial z}\right) = -\frac{\partial p}{\partial x} + \rho g_x + \mu\left(\frac{\partial^2 u_x}{\partial x^2} + \frac{\partial^2 u_x}{\partial y^2} + \frac{\partial^2 u_x}{\partial z^2}\right)$$

$$\rho\left(\frac{\partial u_y}{\partial t} + u_x\frac{\partial u_y}{\partial x} + u_y\frac{\partial u_y}{\partial y} + u_z\frac{\partial u_y}{\partial z}\right) = -\frac{\partial p}{\partial y} + \rho g_y + \mu\left(\frac{\partial^2 u_y}{\partial x^2} + \frac{\partial^2 u_y}{\partial y^2} + \frac{\partial^2 u_y}{\partial z^2}\right)$$

$$\rho\left(\frac{\partial u_z}{\partial t} + u_x\frac{\partial u_z}{\partial x} + u_y\frac{\partial u_z}{\partial y} + u_z\frac{\partial u_z}{\partial z}\right) = -\frac{\partial p}{\partial z} + \rho g_z + \mu\left(\frac{\partial^2 u_z}{\partial x^2} + \frac{\partial^2 u_z}{\partial y^2} + \frac{\partial^2 u_z}{\partial z^2}\right)$$

Where g is the acceleration due to gravity.

Vessels were modeled as rigid and blood was assumed to be Newtonian with a density of 1.06 g/cm^3 and a viscosity of 4cP consistent with previous reports of rabbits [84] and upon consideration of shear rates observed in the current investigation.

3.6 Simulation parameters

The following methods describe the simulation process for each subject. First, the model was discretized into an isotropic finite element mesh with a maximum edge size of 0.5 mm, such that a ~500,000 element computational mesh was produced. Using mean blood flow inlet boundary conditions and resistance outlet boundary conditions, a steady simulation was then performed with the isotropic mesh. Mean BP and flow results for each outlet were compared to values measured from catheter BP and PC-MRI data, and adjustments were made to terms in the 3-element Windkessel models for each outlet to ensure the mean simulation accurately matched physiological data (mean BP difference < 1 mmHg, mean flow difference < 5%). Following the first simulation, localized refinement of the mesh elements was performed using an adaptation method which regionally redistributes elements based on residual error of the CFD solutions [85, 86]. These methods resulted in an anisotropic mesh of roughly 3 million elements with preferred minimum and maximum edge sizes dictated by the user.

Following adaptation, a mean simulation was performed on the new mesh to initialize the flow domain in preparation for a pulsatile simulation. Pulsatile simulations were performed for 4-6 cardiac cycles using the inflow boundary condition previously described. The number of time steps per cardiac cycle for pulsatile simulations were selected such that they satisfy a Courant-Friedrichs-Lewy (CFL) condition < 1.

Stabilized flow and BP measurements for each outlet were compared with physiologic measurements. Pulsatile flow was averaged over the last cardiac cycle to obtain a mean value, and mean pulsatile flow within 5% of targeted PC-MRI

measurements was deemed acceptable, while systolic, diastolic, and pulsatile BP were within 5mmHg of measured value based on previous research using CFD simulation techniques [13, 87]. The procedure of adaptation, steady simulation, and pulsatile simulation was subsequently performed until simulations met WSS mesh independence criteria (discussed below).

3.7 Mesh independence

If indices of WSS are to be used as metrics to predict the risk or progression of disease, it is important to ensure that calculation of these metrics is not influenced by placement of mesh elements. An undersampled computational mesh may lead to inaccurate indices of WSS that result in erroneous conclusions of the hemodynamic influence on structural and functional alterations.

To this end, as mesh densities increased, TAWSS was quantified in 2mm circumferential bands at four regions of interest: 1) ascending aorta, 2) proximal descending thoracic aorta, 3) mid-descending thoracic aorta, and 4) descending thoracic aorta just proximal to the diaphragm at identical locations in each mesh. For this study, simulation results were deemed to be mesh independent when mean TAWSS at all of these locations changed by less than 1% between successive meshes. Importantly, previous CFD studies investigating hemodynamics in the abdominal aorta utilized mesh independence criteria of 2% and 8% difference in TAWSS [87, 88], suggesting the current methods apply sufficient criteria for spatial mesh independence. In general, final meshes for the control group ranged from 2-2.5 million elements, while corrected and

CoA models ranged from 2.5-3.5 million elements at completion. This discrepancy in element number is due to the more continuous geometry and therefore decreased complexity in blood flow patterns present in control rabbits and does not prevent reasonable comparisons of hemodynamic parameters to be made across groups as all simulations satisfied CFL conditions which account for element size and peak velocity.

3.8 Determination of indices of wall shear stress

Upon verifying that simulation results were mesh independent and replicated aimed BP and flow distributions from clinical measurements, blood flow velocity, BP, WSS, and OSI were visualized using Paraview software (Kitware Inc., Clifton Park, NY).

In its simplest form, WSS (τ) can be defined as:

$$\tau = -\mu \frac{\partial u}{\partial y}$$

where μ is dynamic viscosity, u the fluid velocity near the wall, and y the distance from the wall, such that $\frac{\partial u}{\partial y}$ is the velocity gradient near the wall. The accuracy of WSS is therefore dependent on the proximity to the wall that velocity can be determined. In this regard, CFD offers an advantage over calculation of WSS using other imaging modalities. The resolution of the CFD model has the potential to be much higher than PC-MRI based methods assuming the computational mesh is sufficiently resolved [89].

TAWSS and OSI were calculated [87] over the last cardiac cycle as previously described [90]. Specifically, TAWSS was computed at each node on the surface of the CFD mesh as:

$$TAWSS = \left| \frac{1}{\mathrm{T}} \int_{0}^{\mathrm{T}} \overrightarrow{WSS}\, dt \right|$$

Where $\overrightarrow{WSS}$ is the WSS vector at a node and T is the period of one cardiac cycle. Similarly, OSI was computed at each surface node as:

$$OSI = \frac{1}{2}\left(1 - \frac{\left|\frac{1}{T}\int_0^T \overrightarrow{WSS}\, dt\right|}{\frac{1}{T}\int_0^T \left|\overrightarrow{WSS}\right| dt}\right)\overrightarrow{WSS}$$

OSI is a measure of the cyclic change in WSS over the cardiac cycle and thus indicates the directionality of WSS. Lower OSI values indicate WSS is oriented predominately in the primary direction of blood flow while a value of 0.5 is indicative of bi-directional WSS with a time-average value of zero throughout the cardiac cycle.

3.9 Statistical analysis

Seven rabbits were used for each experimental group. Statistical analysis was conducted using one-way multiple analysis of variance (ANOVA) followed by Tukey-Kramer multiple comparison test. Changes within and between groups were considered statistically significant when $P<0.05$. Data are expressed as means ± standard error of the mean (SEM).

CHAPTER 4: QUANTIFY ALTERATIONS IN HEMODYNAMIC INDICES INCLUDING BLOOD FLOW VELOCITY, WALL SHEAR STRESS, AND CYCLIC STRAIN AS SURROGATES OF MORBIDITY IN A CLINICALLY REPRESENTATIVE MODEL OF AORTIC COARCTATION AND REPAIR

4.1 Review of rationale applicable to the current aim

Recent advancements in computational modeling may allow unique investigation into the hemodynamic and biomechanical basis of morbidity associated with CoA. If untreated and corrected CoA are associated with abnormal hemodynamics, future studies may investigate modifications that restore favorable flow patterns. Although computational modeling methods have recently been applied to CoA patients following repair [14], results will be difficult to establish due to the limited number and heterogeneity of patients at any given center, thus motivating the need for a representative animal model.

The objective of this specific aim was to quantify the impact of pathophysiology on hemodynamics and vascular biomechanics in the thoracic aorta using an animal model representative of clinical CoA. Specifically, the goal of this aim was to reproduce changes in indices observed in untreated CoA distinctly from those occurring with correction of BP and morphology in a manner similar to surgical treatment of resection and end-to-end anastomosis. The aim begins with a description of the animal model developed for this purpose from which morphology, BP, and simulation indices of WSS, OSI, strain, and velocity were observed using CFD techniques to quantify the severity of the hemodynamic consequences caused uniquely by untreated CoA and correction to determine if disparities are indicative of those previously associated with long-term morbidity [72, 91, 92].

4.2 METHODS UNIQUE TO THE CURRENT AIM

4.2.1 Calculation of hemodynamic indices

As mentioned in the previous chapter, simulations were conducted using a parabolic velocity profile mapped to the inflow face and run for 4-7 cardiac cycles until flow and BP results yielded periodic solutions, and indices of WSS including TAWSS and OSI were found to be independent of the computational mesh. Previous imaging studies found local low TAWSS and elevated OSI values that were statistically different from circumferential averages [73, 93] motivating the need to report detailed local WSS results in CFD studies. However, CFD modeling experiments present a unique challenge of how to effectively present 3D data in a method that captures the immense amount of information generated in a way that is both meaningful and succinctly understandable to the reader. To this end, a number of quantification techniques are presented here to provide a clear, concise, and thorough representation of the data from computational simulations. This starts with a description of local quantification of hemodynamic results and then techniques to display the full 3D vessel geometry in a 2D format that is easily understandable.

Circumferential TAWSS or OSI values were extracted at locations corresponding to near where histological and myograph analyses were conducted. Spatially equivalent regions in the thoracic aorta were queried for all rabbits using the worst-case untreated CoA rabbits as a guide. Thus, the proximal region represents the approximate midway location between the LSA and coarctation, while the distal region represents the center of

the impact zone created by the impinging velocity jet. The spatial location of these regions was determined for each CoA model as the axial distance distal to the LSA outlet. To account for variance in vessel shape and size, these distances were expressed in terms of the number of diameter of the descending aortic outlet. The outlet diameter locations for the proximal and distal regions were then averaged across the CoA group such that a single normalized outlet diameter multiple was obtained for the proximal and distal locations to be applied to all models. The distal end of the LSA served as a marker position for the origin of axial plots based on previous work detailing the influence of the aortic valve at locations proximal to the LSA (discussed in limitations).

Circumferential results at each location were divided into 16 sectors of equal size and values within each sector were averaged in order to quantitatively determine the degree of localized hemodynamic alterations due to CoA and correction. Values for each sector were extracted using a series of Matlab scripts. First, a .vtk file corresponding to the TAWSS or OSI of the model was loaded, from which three mesh variables were stored: 1) vertices, containing x,y,z coordinates of the mesh nodes, 2) connectivity, detailing node and element connections, and 3) scalars, containing TAWSS or OSI values for each node.

A plane orthogonal to the path was then determined along the centerline at the locations mentioned above. Circumferential points were then mapped to a virtual set of cylindrical points, and the vessel centerline mapped to the z-axis via a series of rotations. Circumferential position was calculated by the arctangent of the (x,y) components of the points. The (x,y,z) coordinates and WSS indices for points from 0 to 360 degrees were found by interpolating at the four nearest nodes.

4.2.3 Visualization

In order to visualize indices of WSS, the vessel surface was unwrapped and mapped to a cylindrical (θ, l) coordinate system, where θ represents the angular position (0-360 degrees) of the node. The zero degree landmark was selected to lie along the inner curvature of the vessel. The dimension l represents the axial length along the vessel in which the node was located, and is measured relative to the centerline path created during model construction. However since this pathway was user-created, it may not accurately represent the center of the vessel. To adjust the centerline, a circle fitting algorithm was used to fit circles to the vessel at a specified number of evenly spaced locations along the original path. Fitted circles were preferred over a centroid method as centroids would be skewed away from bifurcating vessels. From the adjusted centerline, the (x,y,z) points were stored and used to unwrap the vessel.

The vessel was divided along the inner curvature of the vessel and displayed as a flat surface. From the unwrapped vessel, TAWSS values were queried at locations along the thoracic aorta at specified axial increments using the worst-case CoA group as a guide previously discussed.

4.2.4 Cyclic strain

Cyclic vascular strain and associated mechanical properties were delineated from PC-MRI data acquired at the ascending aortic inlet. Luminal diameter was segmented over the 20 frames of the cardiac cycle using 2D manual techniques. Maximum and mean Green-LaGrange strain ($E_{\theta\theta}$) was calculated as:

$$E_{\theta\theta,mean} = 0.5\left(\left(\frac{D_{current}}{D_{diastolic}}\right)^2 - 1\right)$$

And

$$E_{\theta\theta,max} = 0.5\left(\left(\frac{D_{systolic}}{D_{diastolic}}\right)^2 - 1\right)$$

where D=diameter and $D_{diastolic}$ is its reference value during diastole. Pressure-strain elastic modulus (Ep) was subsequently determined as:

$$Ep = \frac{\Delta BP * D_{mean}}{\Delta D}$$

Where ΔBP = systolic BP – diastolic BP, and ΔD = maximum diameter – minimum diameter.

Aortic distensibility, an index of aortic elasticity, was calculated based on previous research [94] as:

$$Distensibility = \frac{2 * \Delta D}{D_{diastolic} * \Delta BP}$$

4.3 RESULTS

4.3.1 Morphology

Maximum intensity projections (**Figure 8**) of the acquired MRA data confirmed that rabbits undergoing coarctation with silk suture developed a pronounced stenosis following surgery, similar to untreated CoA in humans. Rabbits undergoing CoA with

degradable Vicryl suture initially developed stenosis, however degradation of the suture after 56-70 days returned aortic diameter close to that of controls with modest residual narrowing present in the suture region. These morphological characteristics are similar to human surgical treatment of resection with end-to-end anastomosis, the most common method of surgical intervention in CoA. Control rabbits represented healthy subjects of similar age and weight. There were no differences in body weight between rabbits in each experimental group at the conclusion of the experimental protocol (control: 3.1 kg, CoA: 3.0 kg, corrected: 3.2 kg)

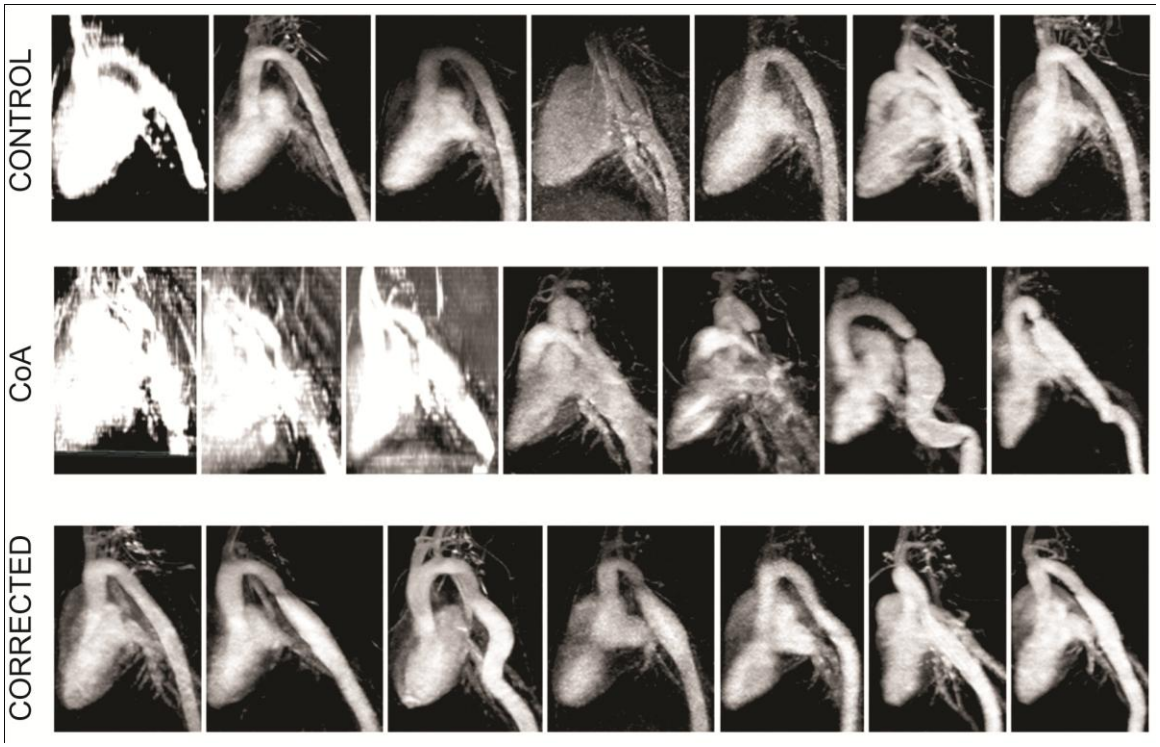

Figure 8. Maximum intensity projections (MIPs) from rabbit imaging data, n=7 rabbits presented for each group.

4.3.2 BP data

Rabbits undergoing coarctation with silk suture demonstrated a significantly increased ($P<0.05$) mean BP gradient of 20 ± 2.0 mmHg across the proximal and distal aortic catheter locations compared to control and corrected groups (**Figure 9**). In contrast, corrected rabbits showed significant alleviation of the BP gradient (2.7 ± 1.3 mmHg; $P<0.05$).

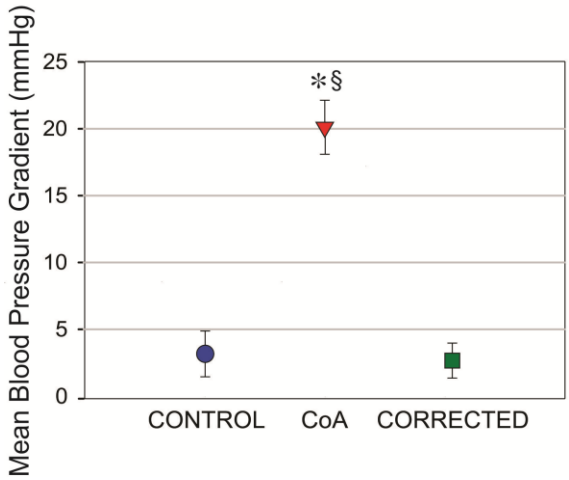

Figure 9. Mean blood pressure gradient from rabbits in each experimental group, taken as the difference between fluid-filled catheter measurements in the carotid and femoral arteries. ✻ = CoA significantly different (P<0.05) from control; § = CoA significantly different (P<0.05) from corrected.

Representative waveforms show increased proximal systolic and mean BP in CoA rabbits (**Figure 10**). Corrected rabbits show BP waveforms similar to control as well as systolic and mean BP significantly less than the CoA group.

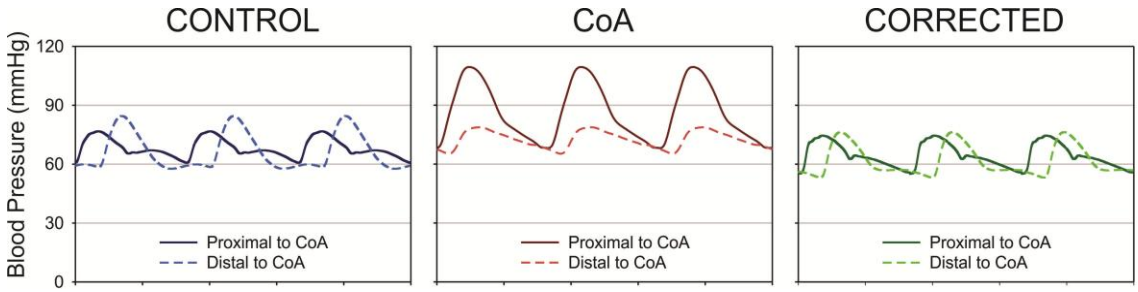

Figure 10. Representative ensemble-averaged waveforms from rabbits in each experimental group. Solid lines indicate proximal (carotid) BP measurements and dashed lines indicate distal (femoral) BP.

Distal artery BP recordings revealed no significant differences in systolic or mean BP across all groups (**Table 3**), however pulse BP was significantly reduced in the CoA group compared to controls (5.5 ± 1.5 mmHg vs. 25.4 ± 1.4 mmHg respectively; $P<0.05$).

		Control	CoA	Corrected
Proximal				
	Systolic BP	71 ± 3	99 ± 7*§	69 ± 3
	Mean BP	64 ± 4	87 ± 8*§	61 ± 4
	Diastolic BP	58 ± 4	74 ± 10	54 ± 4
	Pulse Pressure	13 ± 1	25 ± 4*§	16 ± 1
Distal				
	Systolic BP	78 ± 5	70 ± 9	73 ± 4
	Mean BP	61 ± 4	67 ± 9	58 ± 4
	Diastolic BP	52 ± 4	64 ± 8	50 ± 4
	Pulse Pressure	25 ± 1	6 ± 2*§	22 ± 1

Table 3. Blood pressure measurements (mmHg) obtained at carotid (Proximal) and femoral (distal) locations. Values are means ± SEM, n=7/group. ✲ = CoA

significantly different (P<0.05) from control; † = corrected significantly different (P<0.05) from control; § = CoA significantly different (P<0.05) from corrected.

4.3.3 Velocity, TAWSS, and OSI

Representative solid models for all rabbits are shown in ***Figure 11***. Rabbits undergoing coarctation developed tortuosity distal to the stenosis that was more severe for CoA than corrected rabbits.

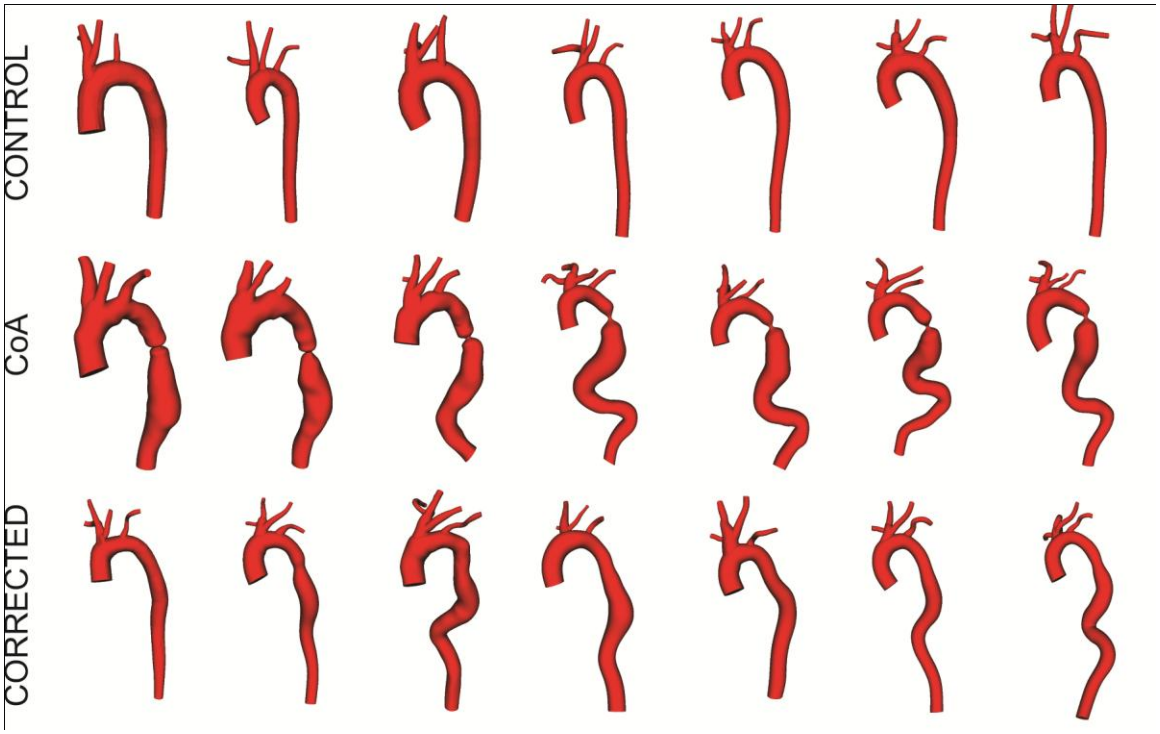

Figure 11. CFD solid models created from volumetric imaging data. Control subjects (top row), untreated CoA (middle row), and corrected CoA (bottom row). Models began at the aortic sinus and terminated at the location of the diaphragm.

Systolic velocity patterns for all rabbits are similarly shown in ***Figure 12.*** Velocity profiles at peak systole in control rabbits were generally parabolic with values ~60 cm/s present throughout the aorta and branches. CoA rabbits show lower velocity in

the aortic arch, a dramatic velocity jet due to the coarctation, and a region of post-stenotic dilation and tortuosity distal to the coarctation. Corrected rabbits demonstrate a region of increased velocity at the coarctation site where residual narrowing was present, and reduced velocity magnitude in the distal region where a moderate dilation is present.

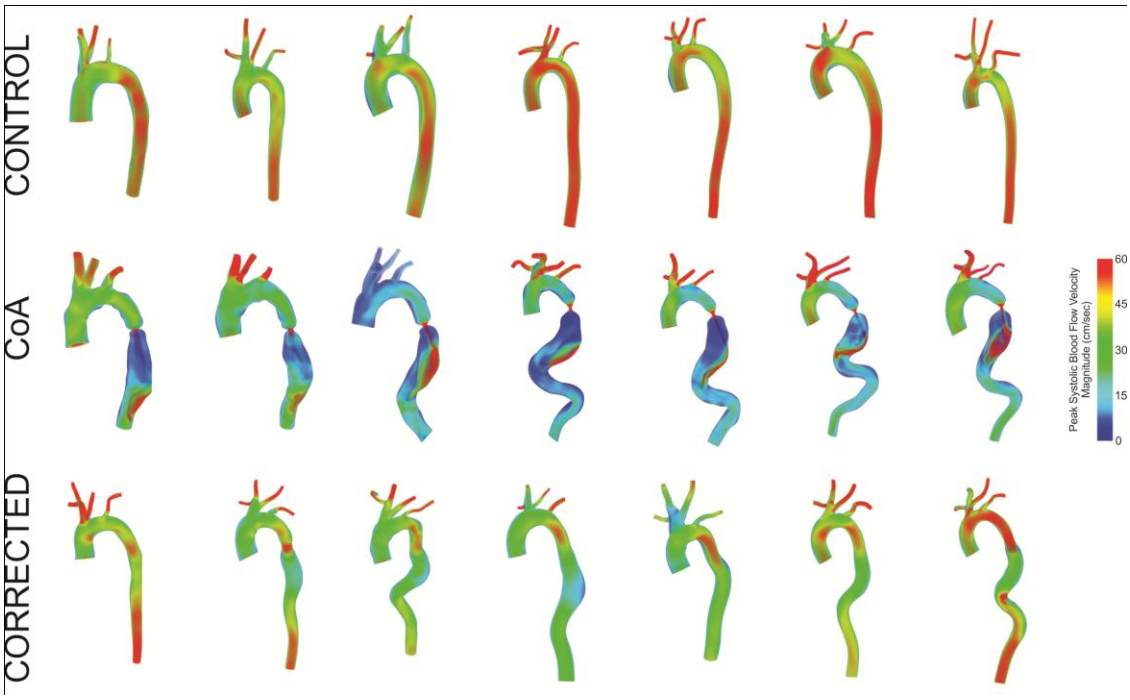

Figure 12. Peak systolic velocity simulation results in control subjects (top row), untreated CoA (middle row), and corrected CoA (bottom row).

Global TAWSS results (**Figure 13**) followed trends consistent with associated velocity distributions. Control rabbits had fairly consistent distributions of TAWSS, particularly in the dAo, ranging from 15-20 dynes/cm^2. CoA rabbits showed marked differences including regions of low TAWSS proximal to the coarctation and extremely high TAWSS at the location of velocity jet impingement distal to coarctation. The corrected group revealed a small region of increased TAWSS at the site of residual narrowing and reduced TAWSS distal to the coarctation.

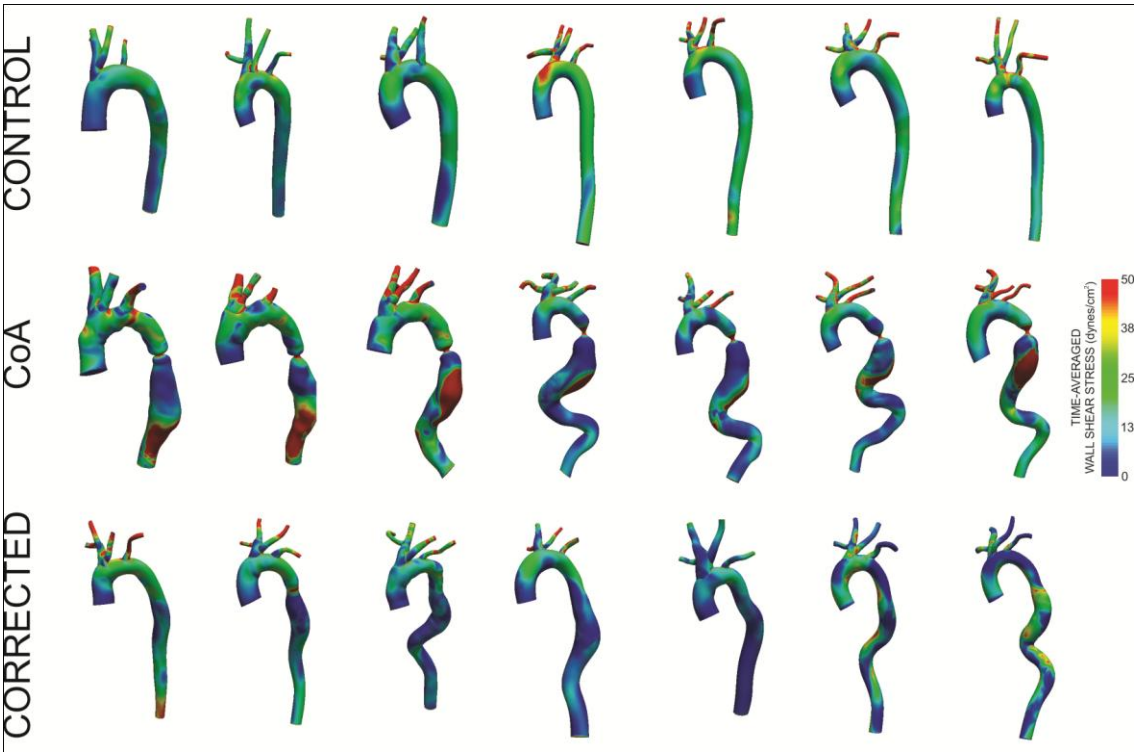

Figure 13. Time-averaged wall shear stress simulation results in the control subjects (top row), untreated CoA (middle row), and corrected CoA (bottom row).

OSI, an index of flow separation, demonstrated values generally ranging from 0.20-0.25 in controls, while CoA rabbits had elevated OSI immediately distal to the coarctation and in the tortuous region (0.40-0.50). These trends were similarly present in corrected rabbits, but to a lesser degree (0.35-0.45; **Figure 14**).

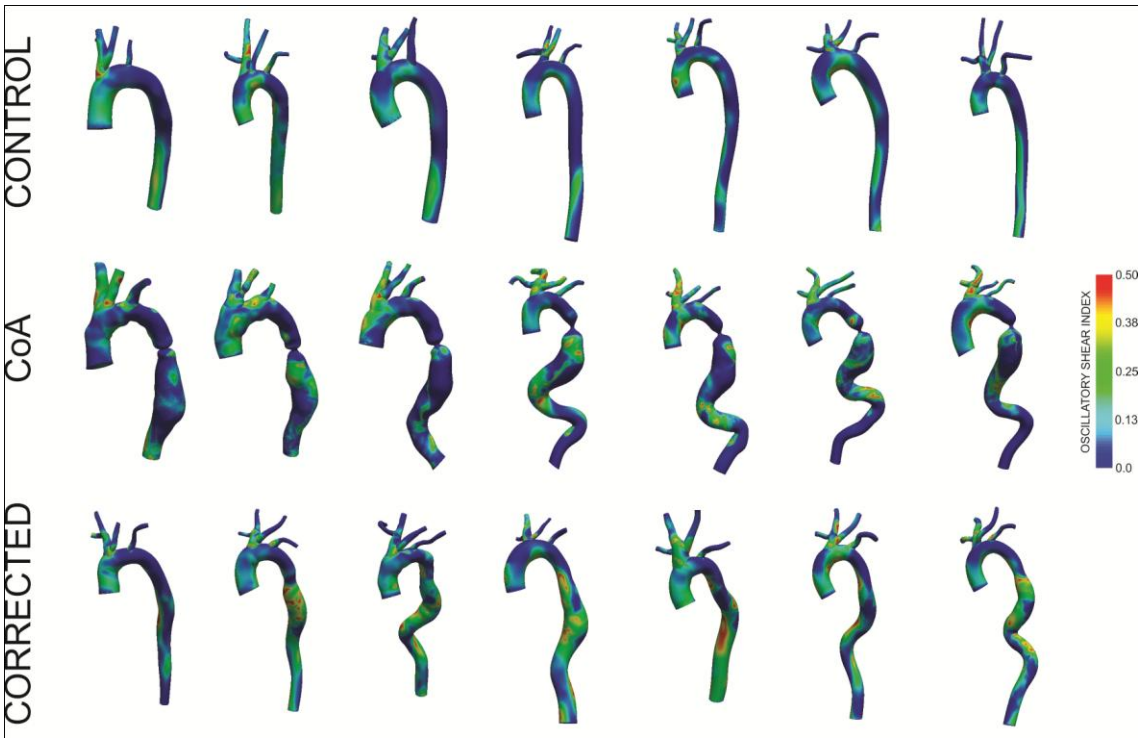

Figure 14. Oscillatory shear index in the control subjects (top row), untreated CoA (middle row), and corrected CoA (bottom row).

	Control	CoA	Corrected
Proximal	6.960 ± 0.168	7.358 ± 0.232	6.847 ± 0.242
CoA stenosis	6.605 ± 0.172	1.894 ± 0.080*§	6.175 ± 0.247
Distal	5.753 ± 0.124	9.529 ± 0.225*§	8.353 ± 0.355†§

Table 4.Vessel diameters for CFD models. Values are means ± SEM, n=7/group. ✻ = CoA significantly different (P<0.05) from control; † = corrected significantly different (P<0.05) from control; § = CoA significantly different (P<0.05) from corrected.

4.3.4 Circumferential TAWSS

TAWSS results unwrapped about the inner curvature of the dAo are presented in **Figure 15**. Proximal to the coarctation, CoA rabbits had significantly reduced TAWSS

compared to controls ($P<0.05$) along the outer wall, but no differences were observed in the corrected group.

In the distal region, CoA TAWSS was significantly elevated at the site where the velocity jet impinged in the outer left wall (100-130 dynes/cm^2 greater than control, $P<0.05$). In contrast, corrected rabbits showed significantly reduced TAWSS in the inner right luminal wall compared to controls (3.3-5.4 dynes/cm^2 in corrected vs. 13.8-17.5 dynes/cm^2, $P<0.05$) at this location.

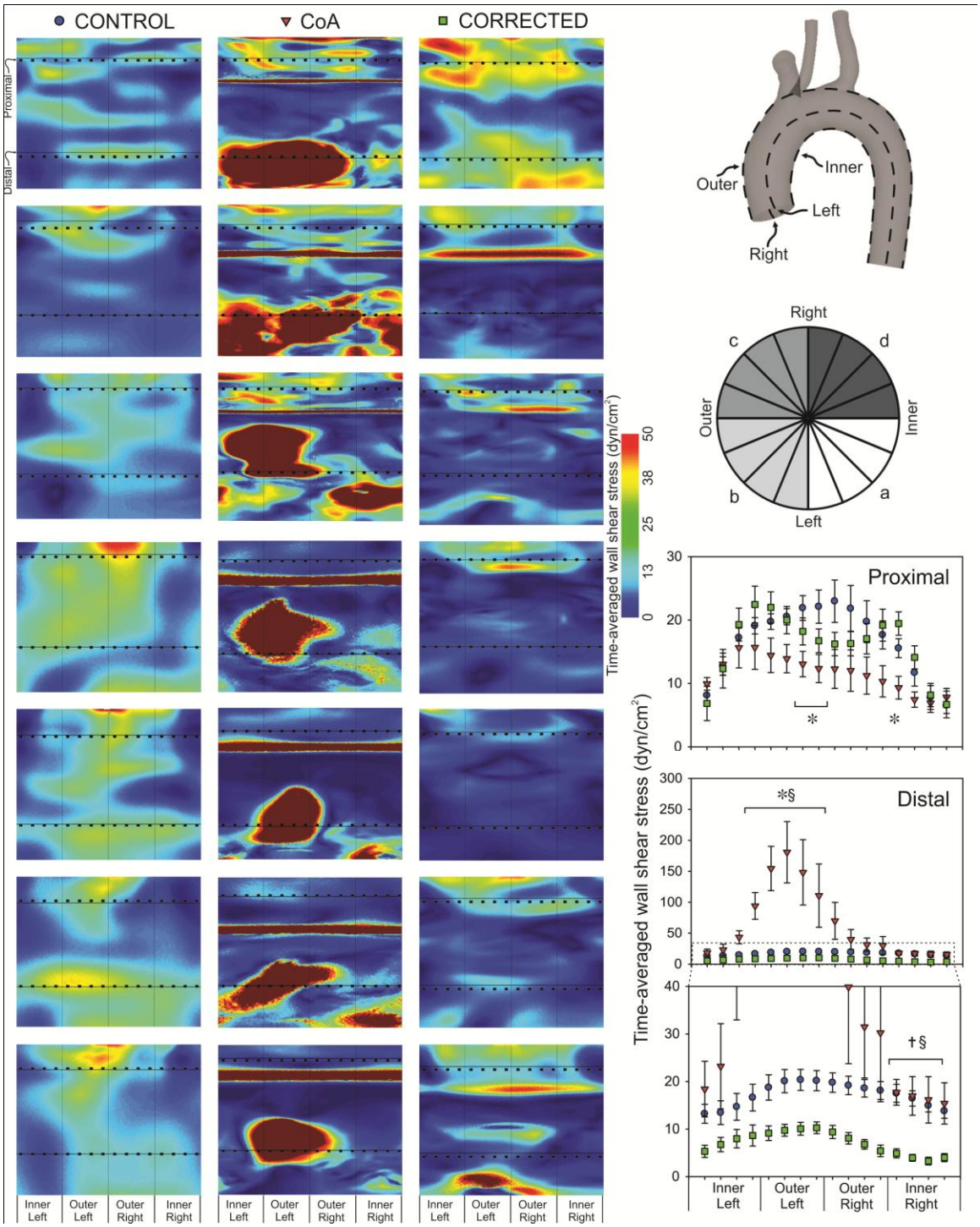

Figure 15. Unwrapped TAWSS data maps for each rabbit (left columns). Schematic of spatial sectors and locations for TAWSS data (top right). Locations where circumferential TAWSS data were quantified at proximal and distal regions are indicated by hashed lines on TAWSS maps (middle left). Distal unwrapped TAWSS results are shown (bottom right) with a range to account for all data, as well as a magnified scale to clarify differences between control and corrected groups. Values are means ± SEM, n=7/group. ✲ = CoA significantly different (P<0.05) from control; † = corrected significantly different (P<0.05) from control; § = CoA significantly different (P<0.05) from corrected.

4.3.5 Cyclic Strain

CoA and corrected rabbits demonstrated significantly (P<0.05) reduced mean and maximum strain at the ascending aorta as well as distensibility compared to controls, with CoA rabbits showing pronounced reductions as compared to the corrected group (**Table 5**). Pressure-strain elastic modulus was significantly increased in CoA rabbits ($47.2\pm4.66*10^3$ N/m^2, P<0.05) compared to both controls ($8.46\pm1.05*10^3$ N/m^2) and corrected ($15.6\pm1.39*10^3$ N/m^2) rabbits, indicating increased stiffness in the CoA group. Ascending aortic diameter in CoA rabbits was significantly greater (P<0.05) than controls: 8.976 ± 0.393 mm vs. 7.531 ± 0.225 mm. Corrected rabbits showed a slight increase in mean diameter (8.137 ± 0.195 mm), but this did not reach significance.

	Control	**CoA**	**Corrected**
Mean Eθθ	0.138 ± 0.013	0.044 ± 0.004*§	0.068 ± 0.004†
Max Eθθ	0.274 ± 0.025	0.082 ± 0.005*§	0.156 ± 0.003†
Modulus, N/m^2	8.46E+03 ± 1.05E+03	47.2E+03 ± 4.66E+03*§	15.6E+03 ± 1.39E+03
Mean Diameter, mm	7.531 ± 0.225	8.976 ± 0.393*	8.137 ± 0.195
Aortic Distensibility	0.038 ± 0.005	0.008 ± 0.002*§	0.019 ± 0.002†

Table 5. *Strain parameters delineated from PC-MRI imaging data. Values are means ± SEM, n=7/group. ✲ = CoA significantly different (P<0.05) from control; † = corrected significantly different (P<0.05) from control; § = CoA significantly different (P<0.05) from corrected.*

4.4 SUMMARY

Research has indicated the conduit and cushioning functions of the thoracic aorta are influenced by CoA in a manner that may cause persistent changes to vascular biomechanics and hemodynamics despite removal of the stenosis. Unfortunately the scarce number of affected human patients at any given center and their heterogeneity in terms of treatment or accompanying co-conditions severely limit analysis of hemodynamic alterations caused directly by the CoA. Therefore the objective of this specific aim was to quantify the impact of CoA pathophysiology on hemodynamics and vascular biomechanics of the thoracic aorta in an animal model representative of clinical CoA and correction in human patients. Putative criteria for surgical intervention (a mean BP gradient ≥20 mmHg) in CoA was established in the untreated CoA group, demonstrated by the presence of a significant mean BP gradient compared to control and corrected groups, as well was an increased systolic BP. Importantly, the corrected group demonstrated a complete alleviation of mean BP gradient, with systolic BP and mean BP similar to controls, thus mimicking critical clinical criteria of successful end-to-end anastomosis repair of coarctation. As compared to previous research studying pathophysiology of induced CoA [95-97] often using animal models with excessively large BP gradients that may result in vascular phenomena not normally associated with CoA, the current methods benefit from a more realistic representation of BP gradient. In the current study, morphological characteristics were in agreement with clinical findings, as the CoA group demonstrated development of a stenosis, post-stenotic dilation, and tortuosity similar to that of untreated CoA patients, while corrected rabbits showed modest residual narrowing at the location of CoA and a slight dilation distal to the

stenosis. The methods described therefore provide evidence that significant alterations to indices of hemodynamics and vascular biomechanics occur due to CoA and persist despite BP restoration. These methods also provide an animal model of coarctation that facilitates longitudinal studies to determine long-term consequences of the disease that is completely independent of confounding genetic or developmental factors.

The current aim used this model coupled with CFD to analyze the degree of localized alterations to hemodynamic indices of WSS, OSI, and blood velocity due to untreated and corrected CoA. Peak velocity was parabolic with a magnitude ~60 cm^2/s throughout the thoracic aorta of control rabbits, while untreated rabbits demonstrated reduced velocity above the stenosis and a stenotic velocity jet in the descending aorta. Corrected rabbits showed modest flow acceleration in the region of residual narrowing, and slightly reduced velocity in the distal dAo at the location of modest dilation. Results from TAWSS data complimented these velocity observations. In CoA rabbits, reduced TAWSS was present proximal to the stenosis, while the pronounced velocity jet causes increased TAWSS distally and appears to play a role in the tortuosity observed. Corrected rabbits show reduced TAWSS in the distal region, and these are likely caused by morphological changes associated with the impinging velocity jet during CoA.

The current results of velocity distribution in control rabbits are in agreement with previous research which characterized flow in the thoracic aorta of healthy adults using 3D MRI [57, 72, 73]. Previous work using CFD methods similar to those used in the current aim demonstrated flow patterns reflective of these trends, which involved mainly axial flow during early systole, and helical flow patterns in the descending aorta [14, 57]. Subsequent analysis of age and gender matched patients following CoA correction with

resection and end-to-end anastomosis showed alterations to WSS in the form of low TAWSS distal to the stenosis due to re-circulating flow. The current CFD results demonstrated parabolic flow during peak systole in controls and reduced velocity and WSS distal to the stenosis in corrected subjects, thus agreeing with flow patterns in both control and corrected human subjects from previous 3D MRI and CFD studies. This supports the comparison of hemodynamic indices using the current CFD methods. The results indicate that changes in vascular morphology due specifically to CoA induce alterations in indices of velocity and WSS in untreated and corrected CoA which are independent of developmental factors.

Regions of low TAWSS appear to be predisposed to atherosclerosis in the thoracic aorta [72], however little is known about alterations in TAWSS due to CoA. The current methods allow understanding and quantification of critical hemodynamic indices at multiple scales in a more accurate manner than conventional ultrasound based methods. The results indicate CoA causes hemodynamic alterations above and below the stenosis, and that alterations distal to the stenosis may lead to persistent hemodynamic changes that persist despite BP alleviation. From a clinical perspective, these findings may be used to augment treatment techniques in coarctation either by considering patient outcomes based on the severity of hemodynamic alterations as a result of correction, or by development of treatment techniques which result in minimal disturbance to hemodynamic indices.

Arterial stiffening was observed in untreated and corrected CoA through vascular biomechanics indices of reduced distensibility and strain. Alterations to resting biomechanical properties are typically reflective of changes in collagen, elastin, and

medial thickness [98], and aortic stiffening causes increased cardiac afterload and decreased coronary perfusion [10]. Thus, the ability of the current methods to determine localized alterations in both CoA and corrected subjects is useful in understanding possible causes of late morbidity in patients following surgical correction of CoA. Reduced strain in the untreated group is likely due to the downstream coarctation, however results from the corrected group indicates that resting tension remains elevated despite BP alleviation. This finding is in agreement with previous studies suggesting altered vascular properties persist despite treatment [46]. These abnormalities are likely to contribute to the development of late systolic hypertension and atherosclerosis.

In summary, by quantifying hemodynamic and vascular biomechanics indices in a representative animal model of CoA and correction, these results indicate the ramifications of coarctation go far beyond the removal of the BP gradient, as altered hemodynamic and vascular biomechanics indices persist under these treatment guidelines. The incorporation of patient-specific outlet boundary conditions allows clinical measurements of pressure and flow to be replicated in CFD results and illustrate the benefits of including flow disturbances caused by CoA. These CFD methods may be extended to identify specific cellular mechanisms affected by altered hemodynamics in CoA.

4.5 Limitations

Results from the current aim should be interpreted within the constraints of several potential limitations. Notably, CFD models in the current methods used rigid

walls that do not account for deformability, which may provide more complete information of hemodynamic alterations but were not implemented into the current model due to the immense computational cost required for larger models. Spatial changes in tissue mechanical properties were not considered which may be of particular concern as it has been shown that 60% of total arterial capacitance is located in the proximal thoracic aorta and decreases distally leading to tissue properties that account for increased rigidity and pulse wave amplification relative to the upstream locations [4]. Recent advances in CFD modeling are now beginning to account for spatially-varying tissue properties [99], and future implementation of these methods may allow a more accurate simulation of pulse BP changes in coarctation, as the current CFD results appear to underestimate this value. Results presented from CFD simulations should also consider fluid dynamics of the rabbit vasculature. Importantly, mean Reynold's number in the ascending aorta of the current rabbits ranged from ~260-300, while previous studies investigating CoA in humans demonstrate mean Reynold's numbers of ~1100-1500 [14]. Although these data confirm the assumption of laminar flow in both cases, differences present in the flow regime of rabbits suggest viscous-dominated flow is present, while human aortic flow is inertially-dominated. An important implication for evaluation of hemodynamics is that turbulence and secondary flows are not likely to occur in the rabbit aorta, whereas they may be present in the human thoracic aorta. Additionally, a parabolic velocity profile was used as to map the PCMRI flow data to the inflow face. Recent work by this lab has demonstrated that inclusion of the aortic valve geometry at the inlet boundary condition can influence hemodynamic indices in the ascending aorta as far as the LSA. In lieu of implementing subject-specific valve anatomy into the current CFD models, this limitation

was addressed by truncating quantitative analysis of hemodynamics to regions distal of the LSA, as the influence of valve inclusion is limited to this region in previous analysis.

It cannot be confirmed that mesh independence was reached at all locations of the CFD simulation in each subject. Although there were some portions where mesh independence was achieved, the areas were selected with no consideration for regions of complex flow or vessel tortuosity, both of which could influence regional variations in TAWSS.

CHAPTER 5: COMPARE STRUCTURAL CHANGES IN THE ARTERIAL WALL ACCOMPANYING COARCTATION-INDUCED ALTERATIONS IN HEMODYNAMICS AND VASCULAR BIOMECHANICS USING HISTOLOGICAL TECHNIQUES

5.1 Review of rationale applicable to the current aim

Despite successfully alleviating the BP gradient by surgical treatment, CoA is associated with persistent morbidity. The previous chapter revealed important local alterations in hemodynamic and vascular biomechanics indices that have been previously linked to cardiovascular morbidity. Additionally, long-term clinical evaluations of CoA patients have detailed structural changes present in the proximal arteries of post-repair patients in the form of increased IMT [61, 65], a clinical marker for atherogenic risk. Further research regarding the timeline of surgical intervention found that early repair (<6 months) seems to benefit the aortic wall distal to CoA but does not similarly benefit the aortic wall proximal to CoA. Since surgery as early as the neonatal stage (1-2 months) does not fully alleviate structural abnormalities [61, 62], there is currently some debate as to whether the source of these structural changes is caused by hemodynamic forces from the damaging effects of raised arterial BP due to CoA or rather developmental factors present in the congenital CoA pathology.

Acute hypertensive models have established that localized increases in BP are associated with increased vascular thickness [16, 74]. These changes are thought to occur as a result of homeostatic mechanisms in response to the sustained BP increase whereby wall thickness increases and luminal radius remains constant, thus reducing wall stress. Pressure induced medial thickening may occur through various mechanisms including hypertrophy, hyperplasia, and extracellular matrix remodeling [34, 100, 101]. Similarly, sustained reductions in flow and subsequently WSS are associated with increased vessel thickness through neointimal hyperplasia [102-104] due to WSS homeostasis. Untreated and corrected CoA may cause notable alterations to hemodynamic indices of WSS as

previously illustrated, and these alterations are typically associated with vascular remodeling. While clinical studies are beginning to utilize ultrasound-based methods to investigate localized hemodynamics and IMT in human CoA patients, understanding of these structural changes is limited, particularly in corrected CoA. The current model improves on research in this regard by providing a coupled imaging and experimental method by which highly accurate localized WSS quantification can be compared to precise measurements through histological techniques in untreated and corrected CoA. In addition to quantifying overall changes to medial thickness, evaluation of SMC phenotypic modulation markers smooth muscle (SM) α-actin, non-muscle myosin (NM myosin), smooth muscle myosin heavy chain (SM MHC), and caldesmon is feasible using the current methods and may further clarify how altered hemodynamics and vascular biomechanics may influence structural changes.

Maintenance of arterial structure and function is critically dependent on controlled differentiation of highly specialized vascular smooth muscle cells [100]. A change in differentiation of smooth muscle cells has been demonstrated to occur in conditions of vascular injury [100, 105], and these changes may thus be present in CoA [105, 106]. NM myosin is a motor protein that plays a role in cellular force and translocation through its actin-binding and contractile properties. Although NM myosin is distinguished as a non-muscle protein, it is present in muscle cells and has several functions. Through development, differentiation is thought to occur such that NM myosin expression decreases from ~50% in embryonic stages to less than 10% in mature animals [107]. However recent research has increasingly indicated that NM myosin can uniquely provide a convergence point between external forces and cellular responses that regulate

its activation [108], thus providing a possible link between altered hemodynamics and biomechanics and structural surrogates of morbidity observed in untreated and corrected CoA. External forces may result in phosphorylation or conformational changes in NM myosin which subsequently alter cytoskeleton mobility and filament interaction, ultimately leading to changes in smooth muscle migration and adhesion [109]. While several reports have documented a mechanosensitive role for NM myosin in cell culture experiments [110, 111], no studies to date have observed the expression of vascular NM myosin in pathophysiological conditions where biomechanics can be accurately quantified. These alterations may serve to affect phenotypic expression of smooth muscle differentiation marker proteins specifically by altering NM myosin, which may play a role in the remodeling and functional response.

The current aim seeks to advance research in this area by using a rabbit model capable of mimicking untreated and corrected CoA and free of genetic or other confounding factors. The objective of this aim was to compare structural alterations present in untreated and corrected CoA to control subjects using histological techniques and immunhistochemical analysis. From the experimental model, vascular medial thickness and expression of key smooth muscle differentiation proteins can be obtained in spatial locations of interest proximal and distal to the CoA in each of the groups. The presence of structural abnormalities and altered phenotypic expression of smooth muscle differentiation proteins in groups of untreated and corrected CoA would suggest that alleviation of BP does not address structural changes caused specifically by CoA pathology, independent of developmental factors. When compared with local alterations from CFD, histological and immunohistochemical changes could further elucidate the

cause of substantial morbidities potentially leading to reduced life expectancy and persistent morbidity in post-repair human CoA patients.

5.2 METHODS

5.2.1 Harvest of arteries

The animal model for this specific aim has been described in detail in Specific Aim 1. Following BP catheter measurements, rabbits remained on anesthesia and were prepared for excision of arteries at 32 weeks. The chest was opened via midline sternotomy and the left ventricular apex was incised for perfusion with 400-500 mL of lactated ringer's solution while the rabbit was exsanguinated via femoral vein incision. Rabbits were then humanely euthanized by intravenous overdose of pentobarbital sodium (100 mg/kg), and arteries from the descending thoracic aorta proximal and distal to CoA, LCCA, and femoral were excised and immediately fixed with 10% neutral buffered formalin for histology. Additional sections from the thoracic aorta proximal and distal to CoA were excised for immunohistochemistry as described below. In order to orient arteries for consistent histological measurements, samples were denoted to mark the region closest to the CoA suture and the outer wall using either suture tied to the fascia or tissue landmarks.

5.2.2 Fixation

Fixation with 10% neutral buffered formalin prevents autolysis and putrefaction by creating covalent chemical bonds between proteins and to maintain cells in a natural state for histological observation. This fixative is buffered to a neutral pH to avoid possible damage to blood cells. In addition, formalin permits restoration of natural color to tissues and is thus useful for optimizing light microscopy observation of sections. Previous research has indicated a general minimum guideline of 8-36 hours for fixation time of paraffin-embedded tissues [112-114], and thus a fixation time of at least 48 hours at room temperature was used for all arteries.

5.2.3 Infiltration

After fixation, arteries from the regions mentioned above underwent a controlled infiltration protocol to remove water from the tissue and replace with a solid medium in preparation for sectioning. Samples were dehydrated in graded baths of progressively increasing concentrations of ethanol (70% - 100% EtOH), followed by a clearing agent (xylene) miscible in alcohol. Samples were then infiltrated with molten paraffin wax prior to sectioning for light microscopy at 5 μm. Previous research with vascular sections indicates that paraffin provides a sufficiently hard surface to allow sectioning at this thickness [16].

5.2.4 Orientation, embedding, and sectioning

Arteries were embedded in paraffin wax following infiltration and arteries from the descending aorta were oriented such that sections would be obtained from the region closest to CoA and by notching the paraffin blocks at tissue landmark locations denoting the outer wall. Resulting paraffin blocks were sectioned on a microtome (Leica RTS; Wetzlar, Germany) and collected. Sections were floated on a warm water bath to avoid wrinkling, mounted on clear glass slides, labeled, and allowed to dry.

5.2.5 Staining protocol

Verhoeff Van Gieson staining was used to identify medial borders including the internal and external elastic lamina (IEL and EEL, respectively) and elastic fibers. During this protocol, the tissue is stained with a regressive hematoxylin, composed of ferric chloride and iodine. Differentiation is accomplished by using excess ferric chloride (mordant) to break the tissue-mordant complex. Since elastic tissue has the strongest affinity of the iron-hematoxylin solution, it retains the dye longest and thus remains darkly colored. Briefly, sections were first deparaffinized and hydrated to distilled water by exposure to successively decreasing concentrations of ethanol. Slides were then immersed in Verhoeff's hematoxylin for at least 30 minutes to stain the tissue completely black. Following a brief wash in tap water, sections were differentiated in a 2% ferric chloride solution. This step was performed by periodic microscopic observation for black fibers against a gray background. Extreme care was taken during the regressive staining step to repeatedly observe coloration of samples without damaging adherent tissue to

ensure proper differentiation of the vascular tissue occurred that would allow qualitative and quantitative analysis **(Figure 16)**. Sections were quickly rinsed with water and counterstained with Van Gieson's solution to color collagenous elements red. Upon completion, the sections were dehydrated rapidly, cleared in xylene, and coverslipped using a permount medium [115].

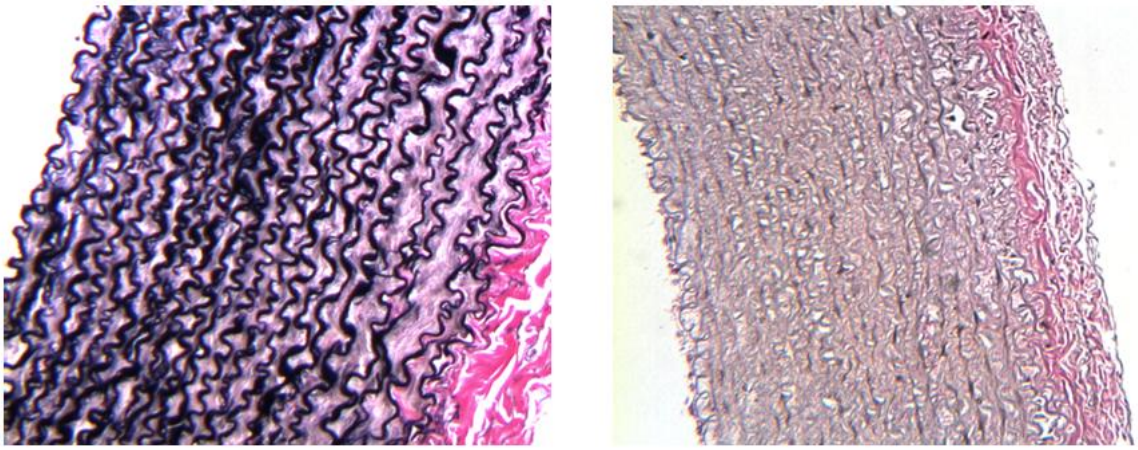

Figure 16. Example of correctly differentiated Van Gieson stained image (left) and overdifferentiation (right) with luminal border on the left and the adventitial side on the right. Elastic laminae and medial borders are obscured throughout (right) due to excessive differentiation with ferric chloride.

5.2.6 Image capture, calibration, and quantification

Digital images of stained sections were collected for qualitative and quantitative observation using a Zeiss light microscope at 6.3x and 16x objective magnifications and stored using IM50 software before color and contrast balancing was performed. Quantification of medial thickness (distance between IEL and EEL) and remodeling area (medial region of elastin fragmentation and discoloration measured radially from the IEL) was subsequently analyzed using ImageJ and appropriate calibration for

magnification strength. Measurements of medial thickness were obtained by use of lines normal to the lumen to accurately measure radial thickness and avoid possible errors due to the natural curvature of the arterial region of interest **(Figure 17)**. The medial area of arteries was also calculated by tracing the EEL and IEL and subtracting the respective areas to account for possible differences in lumen radius and vessel thickness occurring due to artery fixation and varying pressures. For histological analysis, seven rabbits were used for each experimental group. 5 μm sections from each spatial location of interest were taken for each rabbit from which nine measurements were averaged to obtain an estimate of medial and remodeling thickness for each subject. Quantification was conducted in triplicate by three investigators blinded to the experimental group.

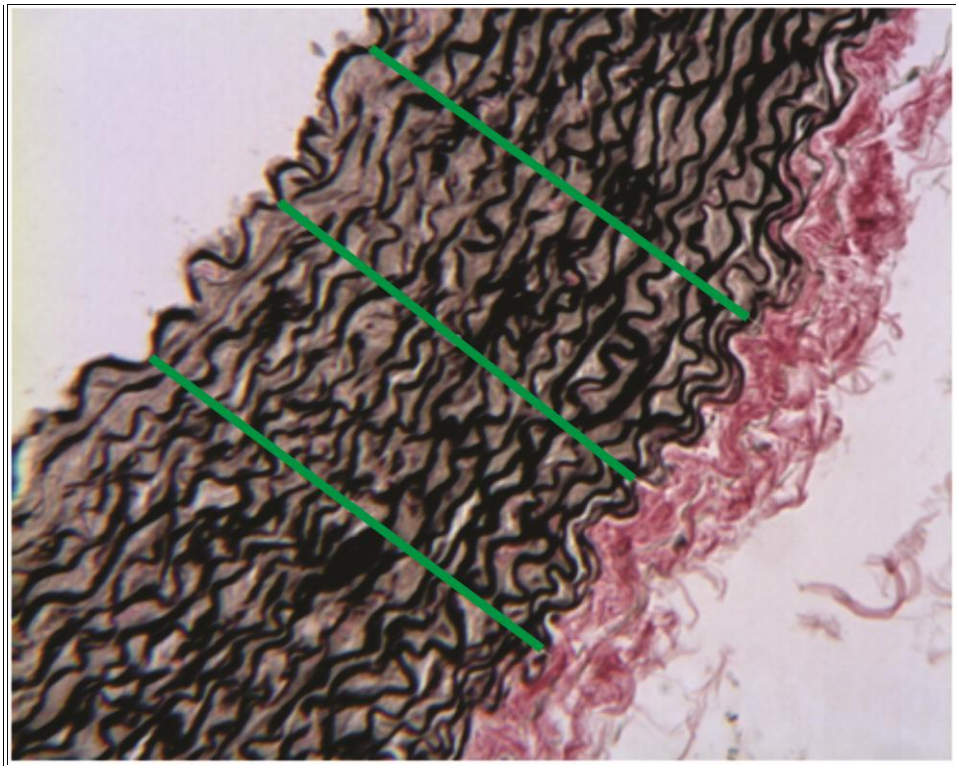

Figure 17. Example of Van Gieson stained image and quantification of medial thickness. Green lines indicate where measurements of medial thickness from inner elastic laminae

to external elastic laminae were made using ImageJ. Measurement lines are normal to the lumen to ensure consistent quantification of thickness.

5.2.7 Immunohistochemistry

To understand the process of structural adaptation in CoA and correction, there is a need to quantify changes in phenotypic modulation of the vascular wall. As such the expression of selected standard SMC differentiation marker proteins [116] were evaluated at proximal and distal dAo locations: SM α-actin, NM myosin, SM MHC, and caldesmon. SM α-actin and SM MHC are isoforms of contractile proteins and are thus excellent markers of the differentiation state of SMC [100]. Caldesmon is an actin and calmodulin-binding protein that has been detected in SMCs and various non-muscle cells [117]. When considered together, expression of these proteins may provide a more sensitive indicator of SMC differentiation than the common use of SM α-actin or SM MHC alone. Tissue specimens from the regions described above were cleaned of blood and loose connective tissue and frozen or isopentane cooled in liquid nitrogen and stored at -80C. 8 um sections were cut on a Leica CM 1900 cryostat, mounted on glass slides, and stored at -20C until used.

Tissues were treated as previously reported [118]. Frozen sections were fixed with 2% paraformaldehyde for 10 min, permeabilized in 0.5% Triton X-100 for 10 min, and blocked with 5 mg/mL bovine serum albumin (BSA) for 1 hour. Sections were reacted with primary antibody for 2 hours and the appropriate secondary antibody for 2 hours, incubated with DAPI (0.5 uM) for staining nuclei, and coverslipped. Multiple washes were used after primary and secondary incubation to avoid non-specific binding. All

immunoreacting solutions were made in PBS-Tween with 0.1% bovine serum albumin (BSA) as carrier. Antibodies were obtained from the following sources: SM α-actin (A 2547), SM MHC (F0791), Talin (8D4), Fibronectin (IST-3) and Caldesmon (T3287) from Sigma Chemical Co (St. Louis, MO); NM myosin (BT-561) from Biomedical Technologies Inc (Stoughton, MA) ; Cy2 and Cy3 secondary antibodies from Jackson immuno Research (West Grove, PA), and DAPI (157574) from Molecular Probes/Invitrogen (Eugene, OR).

Sections were observed with an Olympus IX70 microscope with epifluorescense illumination. Digital images were taken with 16-bit Princeton Instruments camera controlled through PCI board via IPLab for Windows. In order to view the relatively large media of aortic sections, all images were taken at 10X air lens. Quantitative analysis was performed using ImageJ software. Grayscale images for SM α-actin, NM myosin, SM MHC, caldesmon, fibronectin, and talin were collected using similar light intensity and exposure times for all samples. For quantitative comparison of SMC protein expression, mean optical density was determined from 3 randomly chosen regions of interest of equal size from each animal (9-15 per group) which spanned the entire medial wall in each region and the mean optical density was determined. For each protein, data was expressed as average values of staining intensity (unitless) ± SEM. Three to five animals were quantified for each experimental group.

5.2.8 Statistical procedures used for data analysis

Statistical analysis of histological and immunhistochemistry data was conducted based on criteria previously outlined in the methods common to all specific aims.

5.3 RESULTS

Histology

Figure 18 shows representative Verhoeff Van Gieson stained images at each region as well as total medial thickness, where hashed portions of the plot indicate the amount of media containing disorganized or fragmented lamellae not present in the control group. The current histological methods using Van Gieson's staining uniquely allows detailed observation of elastic fibers and was thus preferred to more traditional staining techniques using hematoxylin and eosin. In both LCCA and proximal dAo regions, total medial thickness was significantly increased in CoA and corrected groups compared to controls ($P<0.05$) with pronounced elastin fragmentation. These differences in medial thickness were not present downstream of the CoA in the distal dAo or femoral arteries. However disorganized lamellae were also present in the corrected group and to a lesser degree in CoA rabbits in the distal dAo. Elastic laminae are not normally present in the medial layer of femoral arteries and neointimal hyperplasia was not observed in any sections resulting in a remodeling thickness of zero in these distal vessels.

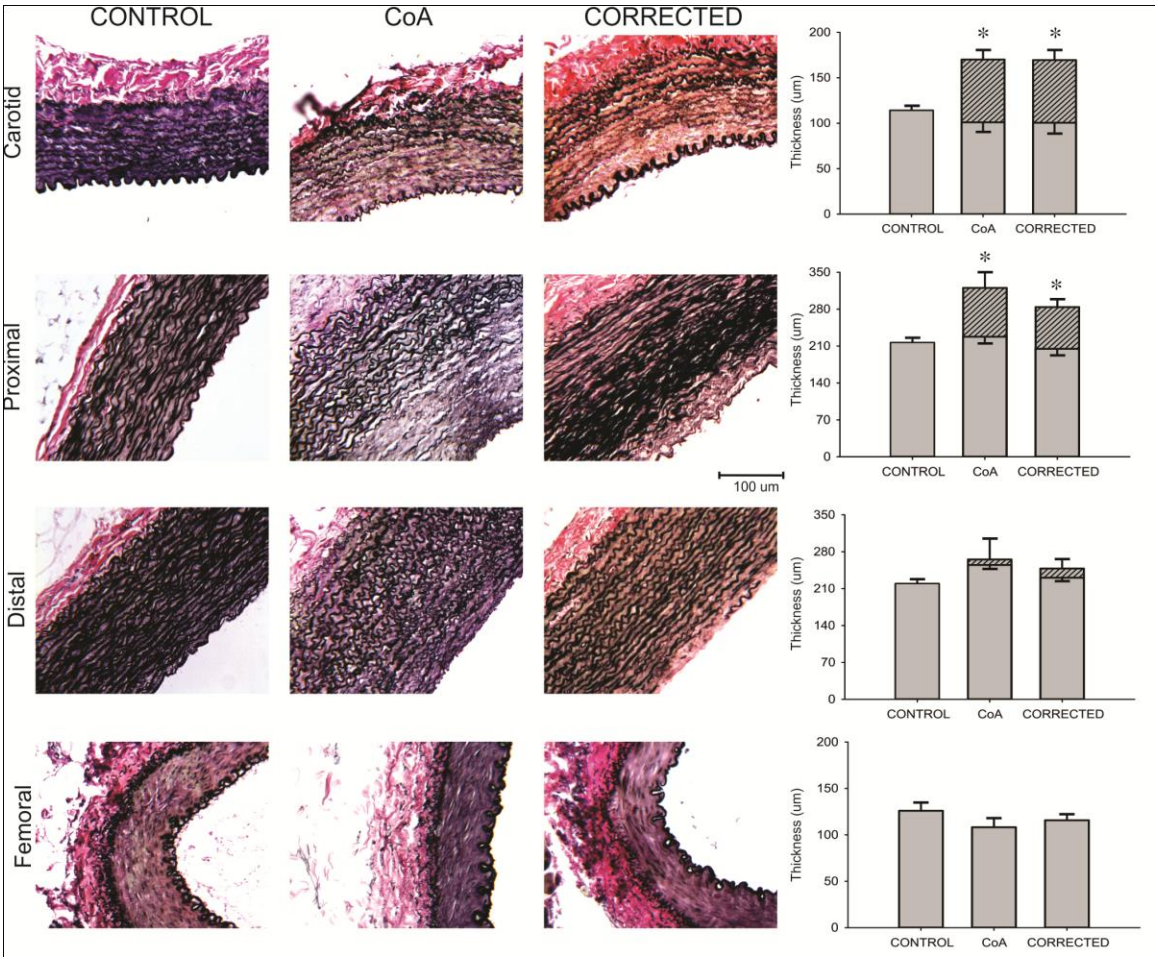

Figure 18. Verhoeff Van Gieson stained arterial sections representative of those obtained proximal and distal to the coarctation region in CoA and corrected groups as compared to spatially equivalent locations from control rabbits. Hashed portions of the plots indicate the amount of the medial layer containing fragmented lamellae devoid of darkly-stained elastin. Upward error bars correspond to the SEM for the entire medial thickness while downward error bars represent the SEM for hashed portions of the plots. ✲ = significantly different ($P<0.05$) from control.

Arteries were not fixed at a defined pressure and thus differences in lumen area and medial thickness may be present as evidenced by previous research [119]. In order to address this limitation, Figure 19 shows quantified medial area in proximal and distal aortic segments in measurements. Proximal results show CoA and corrected medial area

were significantly increased compared to control (P<0.05) while no differences where present distally, similar to thickness results observed.

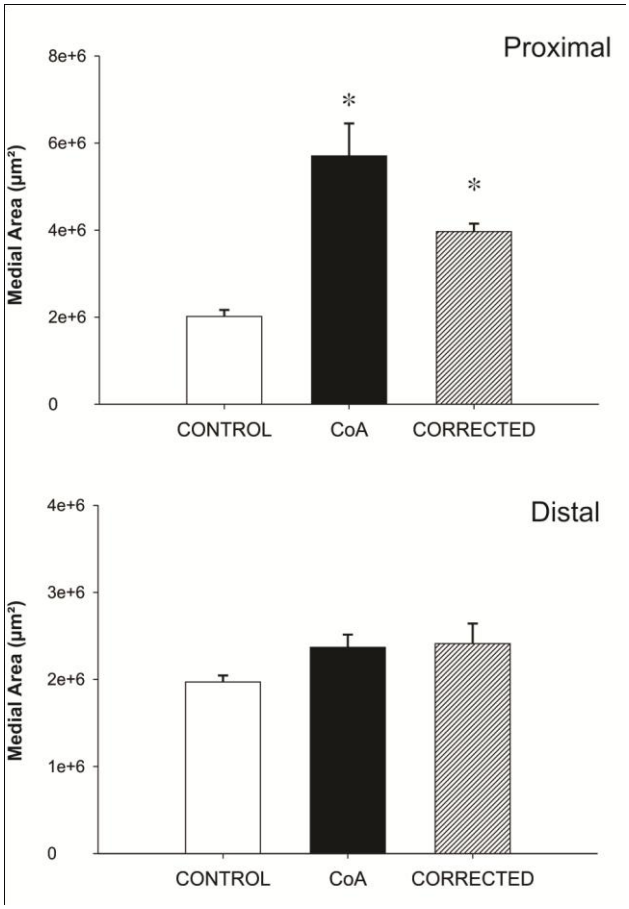

Figure 19. Quantification of medial area (displayed as um^2) from histological segments to account for possible differences in fixation pressure. Area measurements were obtained by tracing EEL and IEL borders and subtracting respective areas. Error bars correspond to the SEM for the medial area. ✲ = significantly different (P<0.05) from control

Immunohistochemistry

NM myosin staining intensity was significantly increased in proximal dAo arteries of both CoA and corrected rabbits compared to control (87.0 ± 6.4 and 83.2 ± 3.6

respectively vs. 37.6 ± 2.6, P<0.05) **(Figure 20)**. These differences were not present in the distal dAo region. No significant differences were observed in fluorophore intensity radially across the media. The use of histograms to further detect any spatial trends in the distribution of NM myosin under experimental conditions also did not yield any significant differences. SM MHC staining intensity of proximal arteries was significantly reduced in CoA and corrected groups compared to controls (51.6 ± 4.4 and 57.7 ± 5.8 respectively vs. 117.8 ± 11.2, P<0.05), while no significant differences in SM MHC intensity were present distally. Caldesmon intensity was significantly reduced in proximal arteries of CoA rabbits, while no differences were present distally (Caldesmon data not shown). There were also no statistical differences in Talin, Fibronectin, or SM α-actin staining intensity across groups (Talin and Fibronectin not shown).

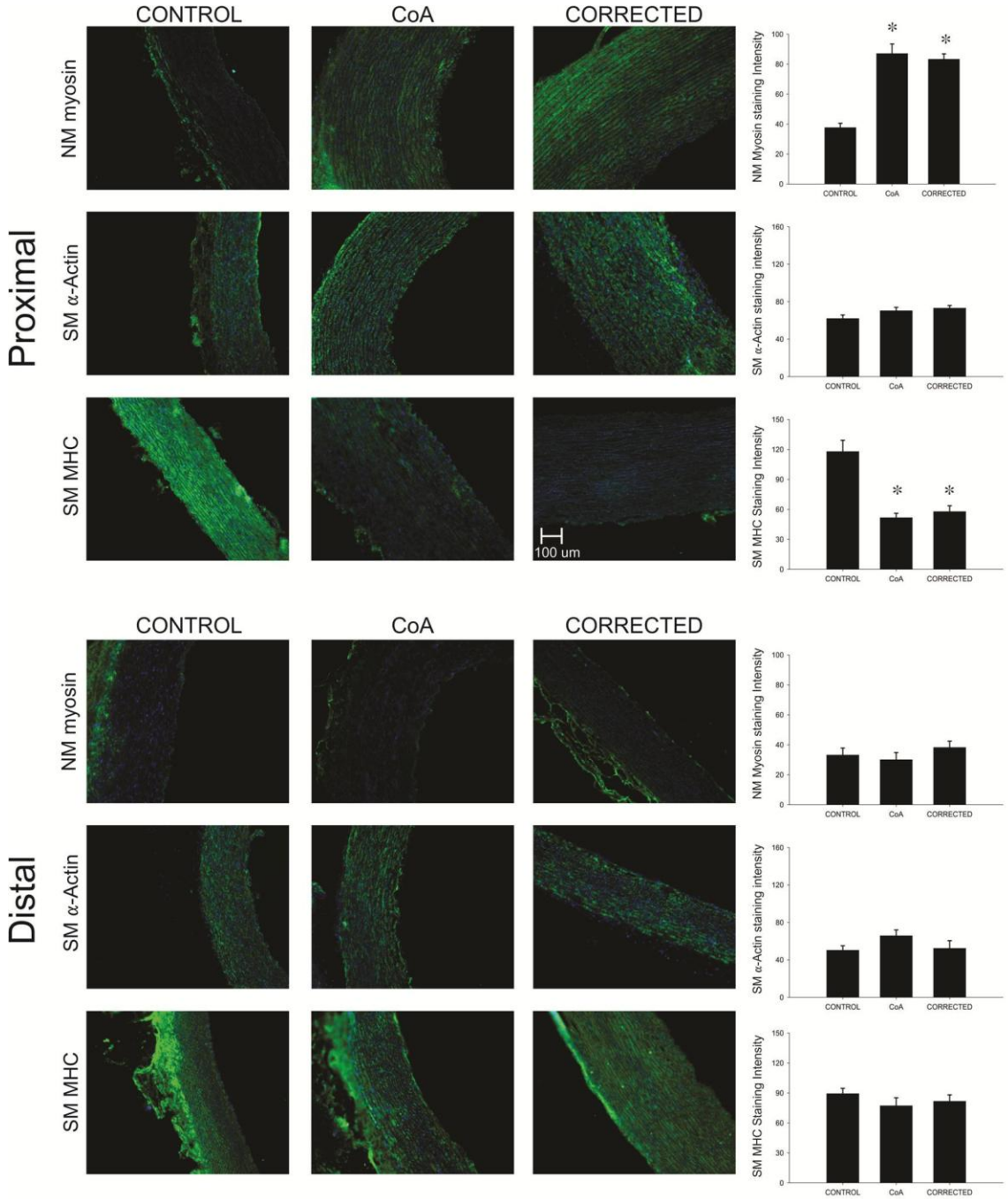

Figure 20. Representative micrographs of immunohistochemical staining of proximal (top row) and distal (bottom) aorta with NM myosin, SM MHC, and SM α-Actin. Quantified staining intensity (mean ± sem) for each location and group (right). ✻ = significantly different ($P<0.05$) from control

5.4 SUMMARY

Histology

Structural analysis of arteries in various pathophysiological conditions has been performed for some time [64, 91, 98, 103, 120, 121]. Studies typically observe medial thickness, intimal thickness, or volume using either a singular response or serial studies to observe the time course of associated changes [36, 74]. The current investigation uses a reproducible method by which structural changes in the arterial wall can be observed in the setting of untreated and corrected CoA at locations near the coarctation and in the distal vasculature to observe changes in the structural properties of conduit arteries relative to local hemodynamic alterations quantified from CFD. Results indicate that structural abnormalities in the form of increased medial thickness, medial area, and elastin fragmentation exist in proximal arteries of untreated CoA and persist in the corrected group despite restoration of a normal BP and BP gradient for 12 weeks (the equivalent of 4 human years). Previous research demonstrates minor changes in luminal radius and wall thickness may be present at different intraluminal pressures which cannot be accounted for using thickness measurements. Medial area was quantified to account for this discrepancy, and statistical trends were similar to thickness results.

The fact that differences in medial thickness and medial area were confined to the proximal arteries supports the theory of a hypertensive vascular remodeling response, as BP was increased in these regions permanently in the untreated CoA group, and transiently in the corrected group. Previous research with hypertensive animal models has

identified this response as a compensatory mechanism by which the vessel seeks to restore wall stress homeostasis [36, 106, 122]. This increased thickness has been documented in the coronary arteries, but not the cerebral vasculature [122]. Interestingly, corrected rabbits demonstrate proximal thickening despite restoration of BP and WSS similar to controls. These results indicate the possibility that altered vasorelaxation and contractility of the SMC may occur in these arteries such that structural changes persist after correction.

Comparing structural results to CFD indices in proximal arteries, it is possible that the increased vascular remodeling in the proximal dAo of untreated CoA subjects may be a result of significantly reduced TAWSS observed in this region which may exacerbate structural changes due to increased BP [16]. Conversely, proximal corrected arteries demonstrate significant vascular remodeling without any differences in TAWSS. Comparing distal structural results with CFD indices, we observe a slight, but not statistically significant, increase in vascular remodeling in the distal dAo of both CoA and corrected rabbits which may be a result of significantly increased TAWSS in CoA and reduced TAWSS in corrected rabbits in the distal dAo.

Although the exact cellular mechanisms governing these structural changes are not know for the current rabbit model of CoA, structural changes may occur through proliferation of smooth muscle cells [123], reduced apoptosis of smooth muscle cells, and increased extracellular matrix deposition [106]. Previous research has identified several vasoactive molecules involved in these processes, including platelet-derived growth factor (PDGF), tissue growth factor (TGF-β), ANG II, and soluble heparin glycosaminoglycans (HSPGs) [100, 124-126].

It is likely that the structural changes of this aim correspond with alterations to vascular biomechanics from PC-MRI strain results discussed in aim 1. For example, reduced strain and distensibility were found in proximal arteries of untreated and corrected rabbits, and this is coincident with vascular remodeling observed in the current aim. Medial thickening and fragmentation of elastin in response to the coarctation may cause alterations in the resting mechanical properties which are reflected in strain results. Load induced fragmentation of elastin in particular has been linked with increased pulse BP [36, 47, 127, 128], a hallmark of CoA. Alterations to conduit vessel stiffness serve to compromise vascular compliance and contribute to permanent cardiovascular complications [129-131].

Immunohistochemistry

Analysis of phenotypic smooth muscle modulation manifested by SM α-Actin, NM myosin, SM MHC, and Caldesmon revealed increased NM myosin and decreased SM MHC expression in untreated and corrected CoA in proximal regions, while SM α-Actin was unchanged. Phenotypic modulation occurring via decreased SM α-Actin has been reported in several studies of hypertension and atherosclerosis [100]. However, few of these studies to date have observed smooth muscle response in the large arteries and previous work with animal models of CoA has demonstrated altered expression of smooth muscle contractile proteins without significant depression of SM α-actin [105, 106]. It was further reasoned that medial smooth muscle may be multifunctional and that loss of SM α-actin is not an absolute prerequisite for phenotypic changes. Previous work

has shown NM myosin to have mechanosensitive properties that allow it to respond to changes in mechanical stimuli through its expression and activation. Increased application of cyclic strain reduces NM myosin expression [132], while more recent studies demonstrate NM myosin activation to be increased in cell cultures with greater rigidity [133, 134]. The mechanosensitive response of NM myosin is thought to involve changes to its actin-linking and contractile functions, which subsequently affect smooth muscle cell migration and adhesion. In the current study, mechanical stimuli in the form of increased systolic BP, pulse BP, and increased mean BP appear to result in increased NM myosin expression as well as decreased SM MHC expression. This dedifferentiation may lead to medial thickening and elastin fragmentation at locations both near the site of coarctation (proximal dAo) as well as further upstream (LCCA).

NM myosin and SM MHC dedifferentiation may cause proximal arterial stiffening manifested through biomechanics indices of reduced distensibility and strain in untreated and corrected CoA. Strain indices in the untreated group are likely due to the downstream coarctation; however the findings of reduced strain and distensibility in the corrected group indicates that passive mechanical properties are elevated despite BP alleviation and is consistent with previous studies suggesting altered vascular properties persist despite treatment [46]. Changes in passive mechanical properties are typically reflected by alterations to collagen, elastin, and medial thickness [119], and aortic stiffening causes increased cardiac afterload and decreased coronary perfusion [10, 135]. The current results indicate phenotypic changes in vascular SMC are present in these regions, which may cause subsequent vascular remodeling and extracellular matrix deposition resulting in arterial stiffening.

Taken together, the stimuli of increased systolic, mean, and pulse BP appear to provide a stimulus for structural alterations in coarctation in the form of increased medial thickness and elastin fragmentation. Results from corrected rabbits suggest these structural alterations take effect within 8-10 weeks of coarctation and persist upon BP restoration. Vascular structural changes in untreated and corrected CoA may alter resting mechanical properties of the conduit vasculature, and may thus elucidate the high rates of early-onset coronary artery disease and hypertension suffered by post-repair CoA patients. Preliminary immunohistochemistry results are the first to provide a possible explanation involving SMC dedifferentiation by which surrogate endpoints for cardiovascular disease are increased despite CoA correction, independent of genetic or developmental factors. The increased expression of NM myosin and decreased SM MHC expression in proximal regions of both untreated and treated groups may illustrate a pathway wherein mechanical stimuli causes dedifferentiation of vascular SMC, which results in medial thickening at the expense of aortic stiffening.

5.5 Limitations

Comparisons of structural alterations across groups must be interpreted within the constraints of several potential limitations. As mentioned previously, changes in medial thickness may occur through several different processes including increased SMC proliferation, decreased SMC apoptosis, and increased extracellular matrix deposition. The current methods sought to determine general structural changes present in untreated

CoA and correction and thus do not allow observation of these specific phenomena, leading to possible ambiguity in the exact cause of medial thickening. Previous research using rabbit and pig models of CoA-induced hypertension have demonstrated an increase in SMC proliferation that occurs in proximal arteries without a compensatory increase in apoptosis [74, 106], thus supporting the role of a proliferative response to hypertension. While the current results demonstrated elastin fragmentation, accurate evaluation of changes to total elastin and collagen content will likely require implementation of advanced molecular techniques targeting specific isoforms of these proteins [75, 136]. Indeed recent research with a rabbit model of CoA has demonstrated total collagen expression is increased in the remodeling response to CoA, however the temporal and spatial expression of collagen isoforms varied [75]. Future *in vivo* studies using 5-bromo-2'-deoxyuridine (BrdU), terminal deoxynucleotidyl transferase (TUNEL) labeling, and collagen isoforms are feasible using the current methods [16, 74, 75], and may elucidate the specific contributions of SMC proliferation and matrix deposition in observed medial thickening.

While the use of Verhoeff Van Gieson's staining uniquely allows observation of elastic fibers, the specialized nature of the stain does not allow bulk staining of sections and thus results in slight qualitative differences in color across individual samples. When possible, these differences were corrected by appropriate white balancing and contrast control using the IM50 software. This limitation was addressed by staining in small groups to ensure proper differentiation occurred for all samples.

CHAPTER 6: QUANTIFY THE ENDOTHELIUM-DEPENDENT AND CONTRACTILE RESPONSE TO AGENTS USING ESTABLISHED MYOGRAPH TECHNIQUES FOR ARTERIAL SEGMENTS IN REGIONS OF ALTERED HEMODYNAMICS AND VASCULAR BIOMECHANICS PROXIMAL AND DISTAL TO EXPERIMENTAL COARCTATION AS COMPARED TO CONTROL RABBITS.

6.1 Review of rationale applicable to the current aim

The endothelium is dynamic, serving to sense mechanical stimuli and regulate vasomotor tone by the release of dilatory substances, as well as antithrombotic and anti-inflammatory agents to maintain vascular health [137, 138]. Impaired vasodilation through endothelial NO release, assessed either through myograph studies in *ex vivo* experiments or non-invasively through forearm hyperemic vasodilatory flow, is a characteristic effect of hypertension. Furthermore, endothelial dysfunction has been associated with numerous cardiovascular disorders including heart failure and atherosclerosis, particularly in coronary artery disease [138, 139].

Vascular constriction, mediated by arterial smooth muscle, may also play a role in the adaptive response of arteries to hypertension. Both active and resting components of vascular contractility may contribute to stiffness. Resting stiffness is reflective of the content of collagen, elastin, and medial thickness [119], while the active stiffness is a function of vascular smooth muscle tone. Vascular stiffness is a risk factor for cardiovascular disease and associated mortality [47, 140], and mounting evidence suggests these vascular impairments caused by the interplay between altered vasorelaxation and vasoconstriction may indicate increased risk of coronary artery disease [17, 141].

CoA induces elevated mean, systolic, and pulse BP in the proximal arteries, and these mechanical stimuli may directly affect vascular function in a manner that increases the likelihood of adverse cardiovascular events. Currently the limited number and heterogeneity of surgically repaired CoA subjects in clinical follow-ups has limited the

interpretations of vascular function analysis. In addition, the *in vivo* assessment of endothelial control of vascular tone in humans is constrained by several limitations and assumptions which must be considered when interpreting clinical studies [141, 142].

Thus the objective of the current aim was to quantify the endothelium-dependent relaxation and contractile response of proximal and distal dAo arteries in untreated and corrected CoA using myograph techniques. Comparison of results across groups will allow identification of possible functional abnormalities in spatial locations of interest in the thoracic aorta and may elucidate substantial morbidities observed in human patients following CoA repair.

6.2 METHODS

6.2.1 Harvest of arteries

The animal model for this specific aim has been described in detail in Specific aim 1. Following BP catheter measurements and euthanasia described previously, arterial segments from the descending thoracic aorta proximal and distal to CoA were excised and maintained in cold (4º) physiological saline solution (PSS; in mM: 140 NaCl, 4.7 KCl, 1.2 $MgSO_4$, 1.6 $CaCl_2$, 1.2 $NaHPO_4$, 2.0 MOPS adjusted to pH 7.4, 0.02 Na_2ethylenediamine tetraacetic acid to chelate heavy metals, and 5.6 D-glucose). Extreme care was taken to avoid damage to the fragile endothelium or smooth muscle

tissue of the aorta upon removal. Arteries were harvested from the aorta at locations illustrated in Figure 21, and were relatively far (>3 mm) from the CoA suture to avoid any potential influence of surgical injury.

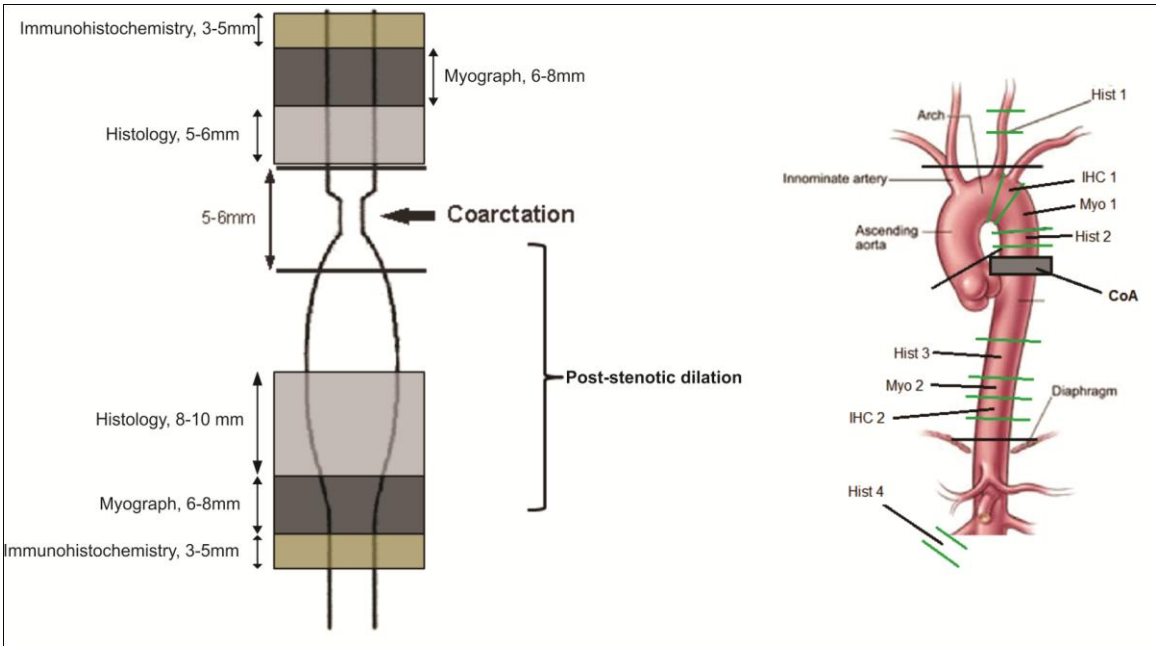

Figure 21. Diagram illustrating location of arteries harvested for histology (Hist), immunohistochemistry (IHC), and myograph (Myo) experiments in the descending thoracic aorta relative to the CoA and post-stenotic dilation (left). Example of map used during harvest (right).

6.2.2 Aortic ring setup and preparation for myograph testing

Arteries were trimmed to 3-4 mm segments and removed of adhering tissue and fat. The resulting segments were mounted on tungsten wire hooks **(Figure 22)** in a water-jacketed isometric myograph maintained in PSS at 37º C and bubbled continuously 95% O_2 5% CO_2. Arteries were allowed to equilibrate for at least one hour in the bath at <2 grams resting tension as discussed in more detail below. To test the viability of tissue

before experimentation, arteries were contracted using a potassium PSS (K^+PSS) to observe contractile response. K^+PSS contains a relatively high concentration ([4.7] mM in PSS vs. [109] mM in K^+PSS) of potassium compared to PSS, which effectively depolarizes the membrane and opens voltage dependent calcium channels, causing an influx of extracellular calcium and subsequently contraction. Tissues were rinsed with PSS at least 3 times following each activation, and allowed to return to resting force, and this process was repeated 2-3 times until force response of an artery was consistent. The time to peak arterial contraction was measured in order to observe general changes in contraction due to calcium influx.

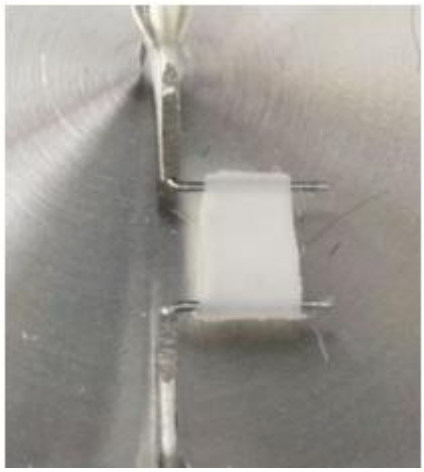

Figure 22. Example of rat thoracic aorta prepared for myograph analysis. Sample is cleared of perivascular tissue, trimmed to 3-4 mm width with squared ends, and mounted on isometric force transducer. (Danish Myo Technology product systems [5])

6.2.3 Determination of resting force

Previous experiments investigating the force-length relationship of smooth muscle have identified a broad peak under which resting lengths produce maximum force due to optimum interaction of actin and myosin filaments (***Figure 23***), reasoned to be the functional length at which smooth muscle operates under resting physiology.

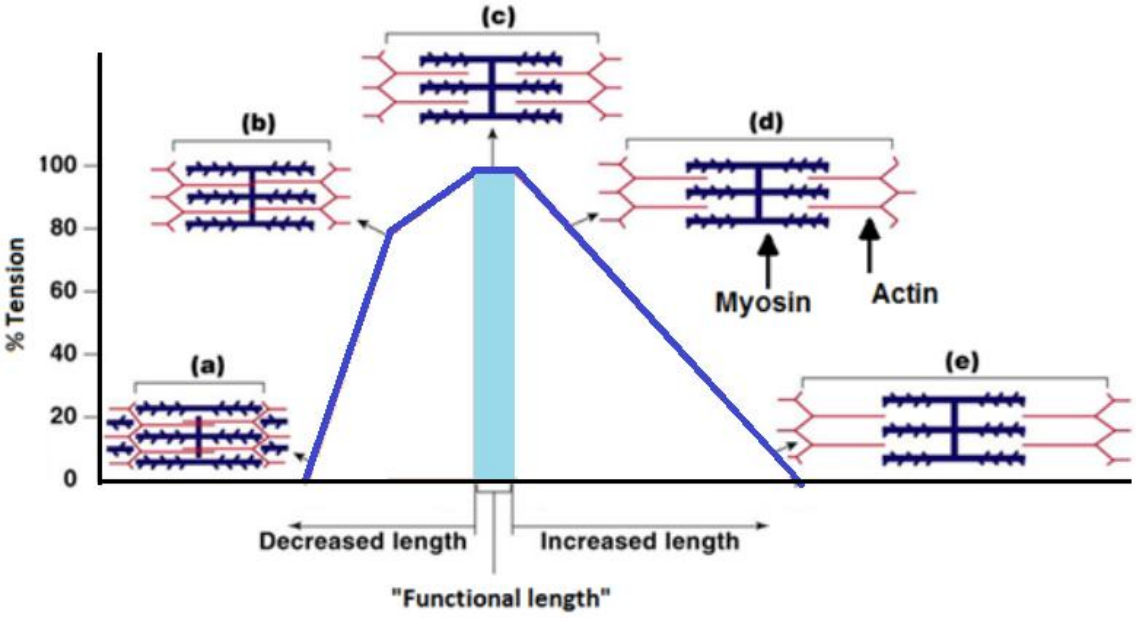

Figure 23. Schematic diagram of smooth muscle length-tension curve. Myosin-actin filament interactions associated with respective lengths are shown to illustrate changes in tension development. At "functional length", myosin and actin filaments interact optimally, resulting in peak tension development. (Adapted from Marieb et al, [6])

Subsequent studies investigated the range of functional length in airway smooth muscle and demonstrated functional length occurred when resting force was 10-20% of active force [143-145]. At lengths corresponding to <10% resting force, active contractile force is decreased and the smooth muscle undergoes visible extension. At lengths >10%, active force is decreased as the smooth muscle resists stretch. Together these studies

illustrate a reproducible reference length for smooth muscle which is important when studying the physical properties of vasomotor tone.

In order to determine the appropriate resting force for functional length in the current study, preliminary experiments with this model investigated active/resting force ratios from K^+PSS contractions under resting forces from 1-5g with control rabbits. It was found that 2 g resting force most consistently produced an active/resting force ratio of 10-20%, and therefore this functional force of 2g was for used for all myograph experiments. This resting force is in agreement with additional studies [146, 147] investigating the functional response of rabbit aortic rings. The decision to use a uniform resting force for all subjects based on control subjects is further discussed in *Limitations.*

6.2.4 Endothelial relaxation: Acetylcholine

To determine the effect of CoA-induced BP and hemodynamic alterations on endothelial function, aortic rings were first pre-contracted with 0.2 uM Phenylephrine (PE) and endothelium-dependent NO relaxation was determined by cumulative addition of acetylcholine (ACH, 10^{-9} to 10^{-5} M) **(Figure 24)**. Force measurements were obtained 5 minutes after addition of ACH, and cumulative response curves were constructed as percentages of active relaxation from pre-contracted tension.

Acetylcholine is an agonist of the M3 muscarinic receptor which has been used extensively to measure the release of NO from the intact endothelium and cause vasodilatation [148, 149]. Activation of the M3 receptors on endothelial cells causes an increase in nitric oxide synthase activity, which results in an increased synthesis of the

highly diffusible free radical NO. NO diffuses from the endothelial cells into the adjacent smooth muscle of the vascular media, where it activates the cytoplasmic enzyme guanylate cyclase. This increases intracellular cyclic-3'-5'-guanosine monophosphate (cyclic GMP or cGMP) which activates cGMP protein kinase and promotes relaxation of the SMC by reduction of cytosolic Ca^{2+} concentration. As this process is critically dependent on the presence of an intact endothelium, the relaxation response to ACH provides an accurate estimate of endothelial function.

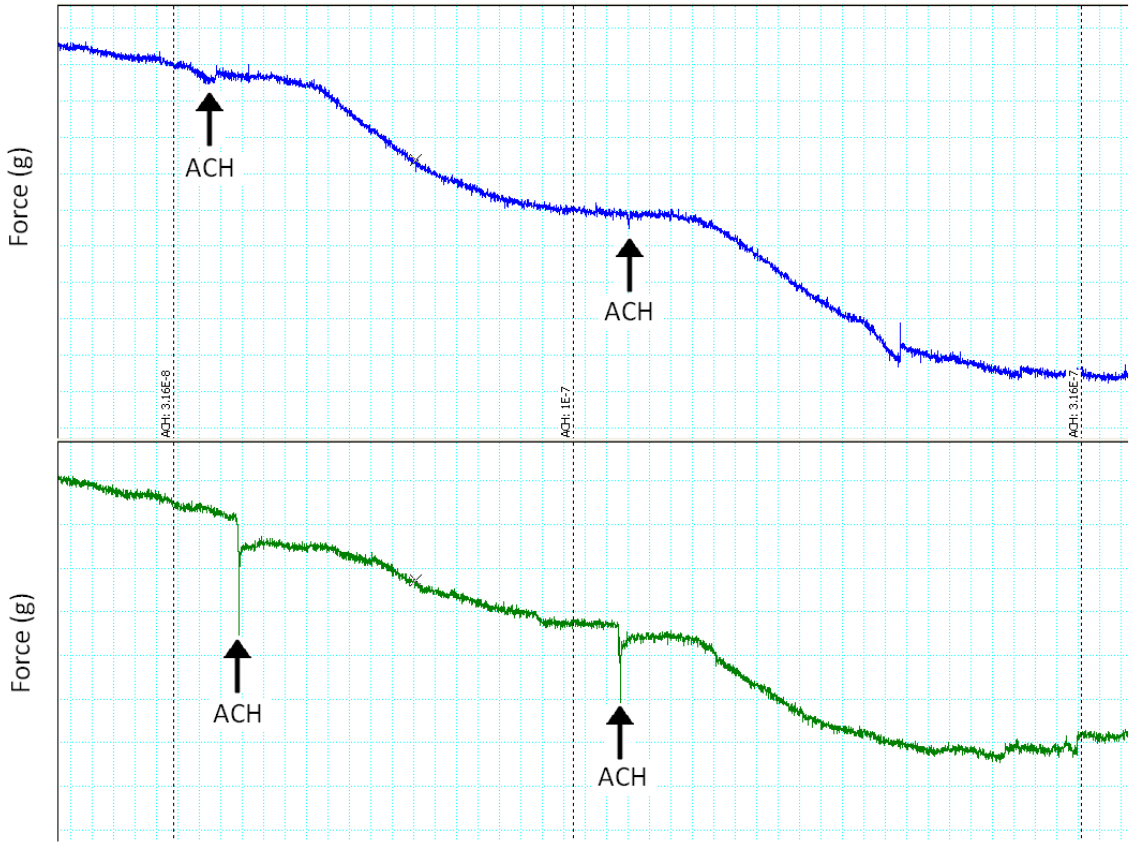

Figure 24. CHART data of Acetylcholine relaxation from myograph experiments with arteries from proximal (blue trace) and distal (green) regions displayed. Arrows indicate when ACH was administered to baths. Subsequent release of NO from the endothelium results in smooth muscle relaxation and decreased force.

6.2.5 Endothelium-independent relaxation: Sodium Nitroprusside

Following ACH experiments, samples were washed at least three times with fresh PSS and equilibrated for >1 hour prior to determining endothelium-independent vasorelaxation to cumulative doses of Sodium Nitroprusside (SNP; a NO donor, 10^{-9} to 10^{-5} M) **(Figure 25)**. Samples were again pre-contracted with 0.2 uM PE before SNP relaxation, and SNP response curves were constructed as percentages of active relaxation from pre-contracted tension.

SNP metabolizes in PSS to release NO, which diffuses to the vascular smooth muscle, causing cGMP-mediated relaxation. As an NO donor, SNP is not dependent on the presence of endothelial cells to cause relaxation and thus provides a method to observe if vasorelaxation impairments are specific to the endothelium.

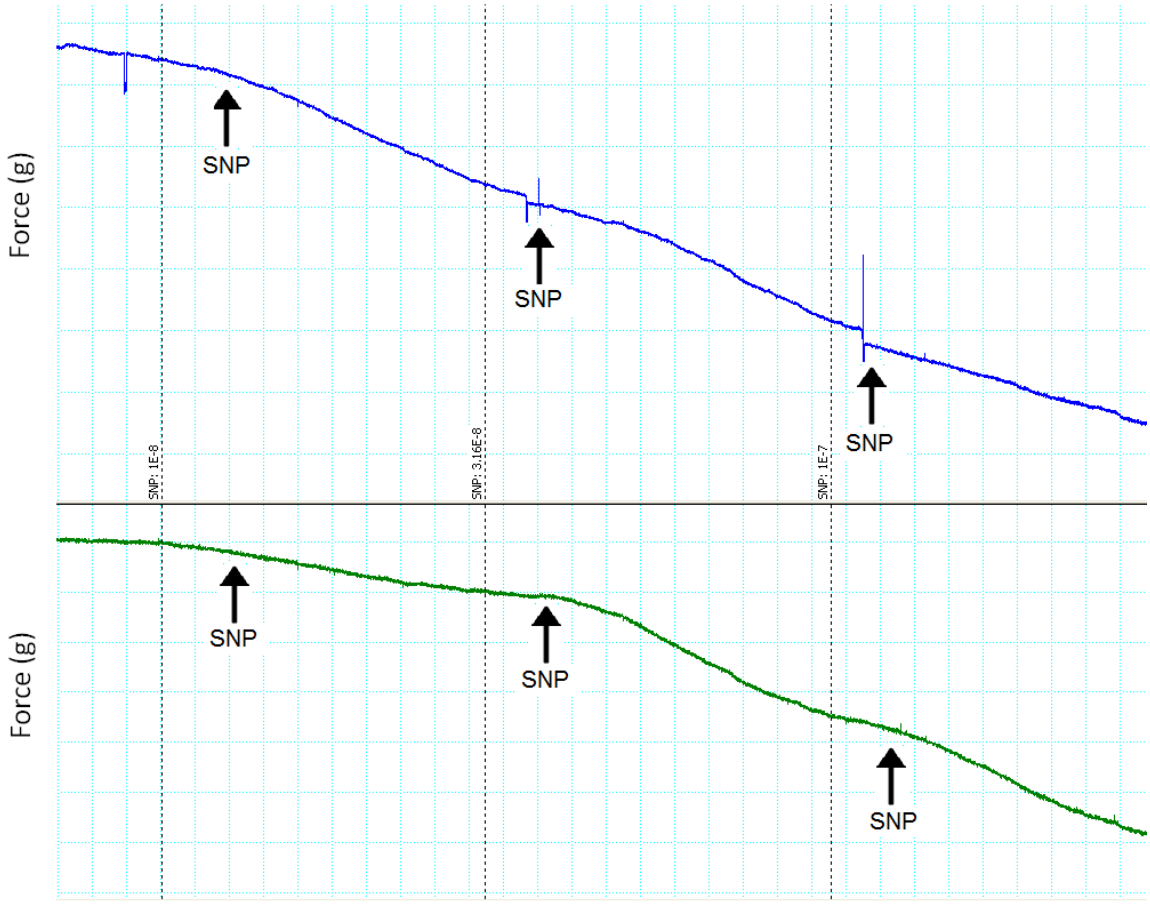

Figure 25. CHART data of Sodium Nitroprusside relaxation from myograph experiments with arteries from proximal (blue trace) and distal (green) regions displayed. Arrows indicate when SNP dose was administered to baths. SNP metabolizes to release NO, resulting in smooth muscle relaxation and decreased force independent of the endothelium.

6.2.6 Vascular contractility

Following SNP relaxation experiments, samples were rinsed at least 3 times with PSS and allowed to equilibrate for at least one hour at resting force. Aortic rings were then stimulated with cumulative concentrations of PE (10^{-9} to 10^{-5} M) **(Figure 26)**. Effective force response to each PE concentration was normalized to the tissue's maximum K^{+}PSS contractile response to account for potential differences in size and cross-sectional area. Cumulative dose response curves for PE were constructed for each

group. Phenylephrine is an agonist of the α1-adrenergic receptor which causes activation of ionosol-triphosphate (IP3) and subsequently calcium release from the sarcoplasmic reticulum leading to vasoconstriction.

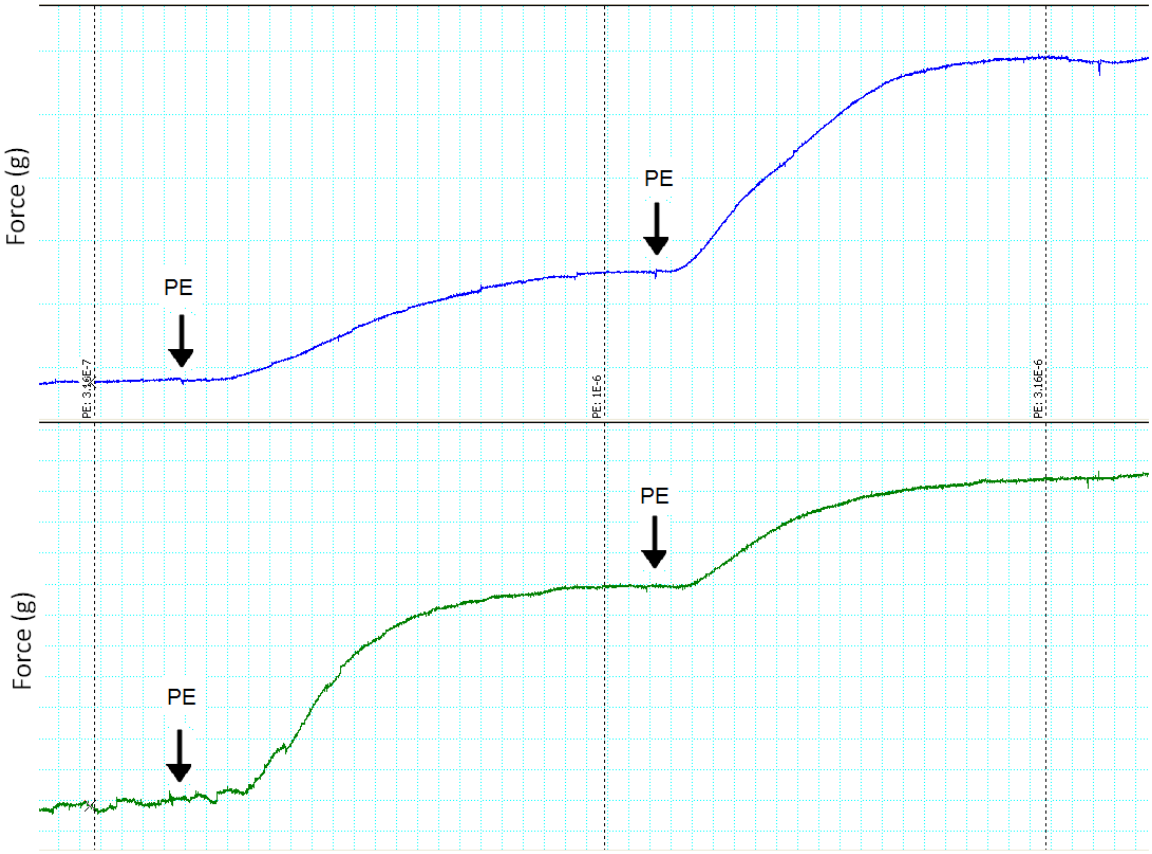

Figure 26. CHART data of Phenylephrine contraction from myograph experiments with arteries from proximal (blue trace) and distal (green) regions displayed. Arrows indicate when PE dose was administered to baths. PE activates IP3, resulting in the release of calcium from the sarcoplasmic reticulum and thus contraction, which increases force.

6.2.7 Statistical procedures used for data analysis

4-5 rabbits were used for each experimental group. At least 2 arterial sections from each spatial location of interest was taken for each rabbit from which measurements were averaged to obtain an estimate of effective dose response values for each subject. Representative CRC curves were obtained by averaging the spatial locations in a single

group of rabbits. Statistical analysis of myograph data was conducted as detailed in the methods common to all specific aims.

6.3 RESULTS

6.3.1 Endothelial relaxation

Arterial relaxation curves in response to the endothelium-dependent agonist ACH at proximal and distal locations are shown in **Figure 27**. Proximal to the coarctation, control rabbits show intact endothelial function by demonstrating ACH relaxation to ~80% of pre-contracted tension. In contrast, both CoA and corrected rabbits showed significantly impaired ACH relaxation (17% ± 4% and 33% ± 6% respectively, $P<0.05$), with CoA rabbits showing marked impairment at peak ACH values. In the distal region, differences between corrected and controls were abolished with endothelial function intact in these groups and relaxations of 85% ± 3% and 78% ± 3% respectively. CoA rabbits continued to show significantly impaired ACH relaxation ($P<0.05$) with peak relaxation of 18% ± 8% of pre-contracted tension.

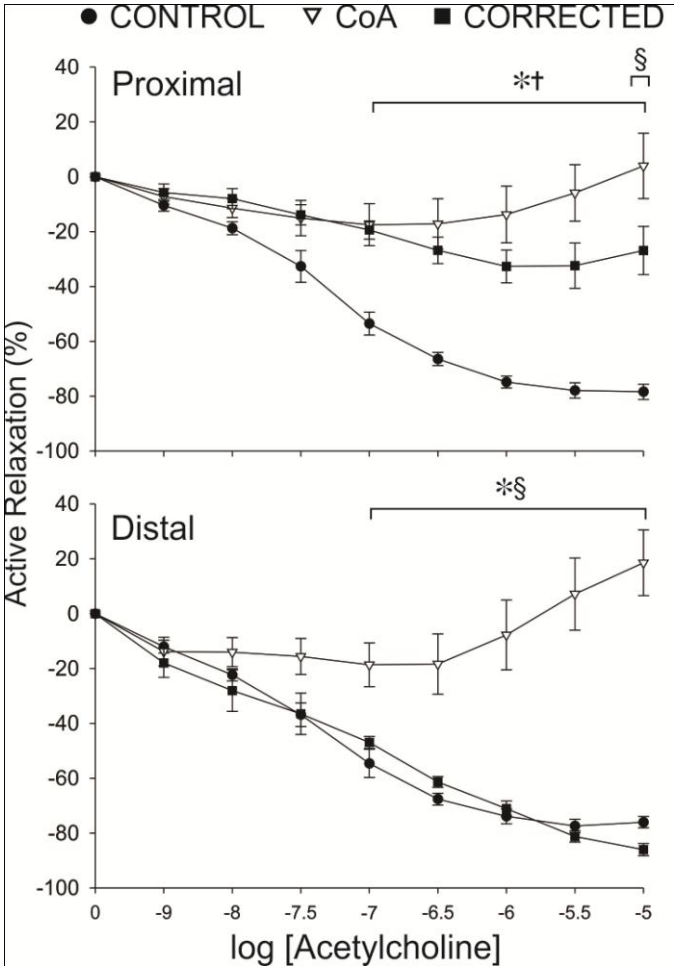

Figure 27. Active vasorelaxation curves in response to ACh for rings of aortic tissue proximal (top) and distal (bottom to the coarctation region in CoA and corrected groups as compared to spatially equivalent locations from control rabbits. ✻ = CoA significantly different (P<0.05) from control; † = corrected significantly different (P<0.05) from control; § = CoA significantly different (P<0.05) from corrected.

Endothelium-independent relaxation to the agonist SNP (**Figure 28**) in the proximal dAo reached ~90% of pre-contracted values in control rabbits. Significant differences between CoA and controls were present at lower doses of SNP (log [-7.5 to -6.5]), however peak SNP relaxation between all groups was not significantly different. Interestingly, corrected rabbits showed similar SNP relaxation response at all doses compared to controls. In the distal dAo, corrected and control rabbits continued to show

similar SNP relaxation response, while CoA rabbits had significantly greater relaxation compared to corrected group at early doses (log[-7 to -4.5]), and control group at peak doses (98% ± 1% in CoA vs 90% ± 1% in controls).

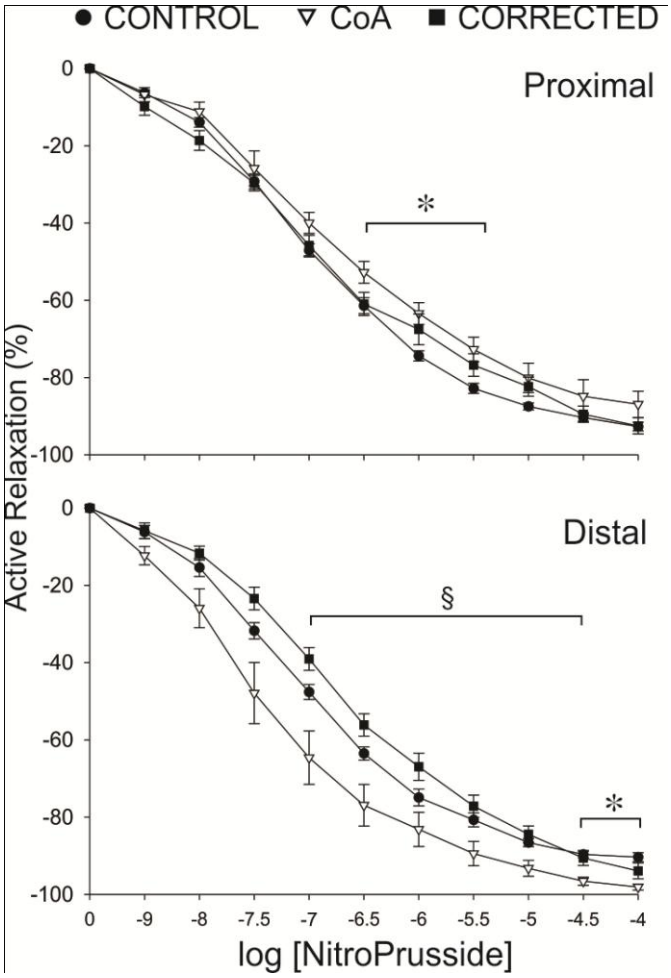

Figure 28. Active vasorelaxation curves in response to SNP for rings of aortic tissue proximal (top) and distal (bottom to the coarctation region in CoA and corrected groups as compared to spatially equivalent locations from control rabbits. ✲ = CoA significantly different (P<0.05) from control; † = corrected significantly different (P<0.05) from control; § = CoA significantly different (P<0.05) from corrected.

6.3.2 Vascular contractility

PE force response was evaluated at proximal and distal dAo locations **(Figure 29)**. In the proximal aorta control rabbits show normalized effective force response peaking at 1.13 ± 0.08, while both CoA and corrected groups showed significantly diminished force at several concentrations of PE, peaking at 0.94 ± 0.04 and 0.92 ± 0.03 respectively ($P<0.05$). In the distal dAo, control rabbits demonstrated peak contractility of 1.04 ± 0.05 and CoA force response was similar, albeit slightly increased. Interestingly corrected force response remained significantly reduced ($P<0.05$) compared to controls with peak isometric force of 0.88 ± 0.06.

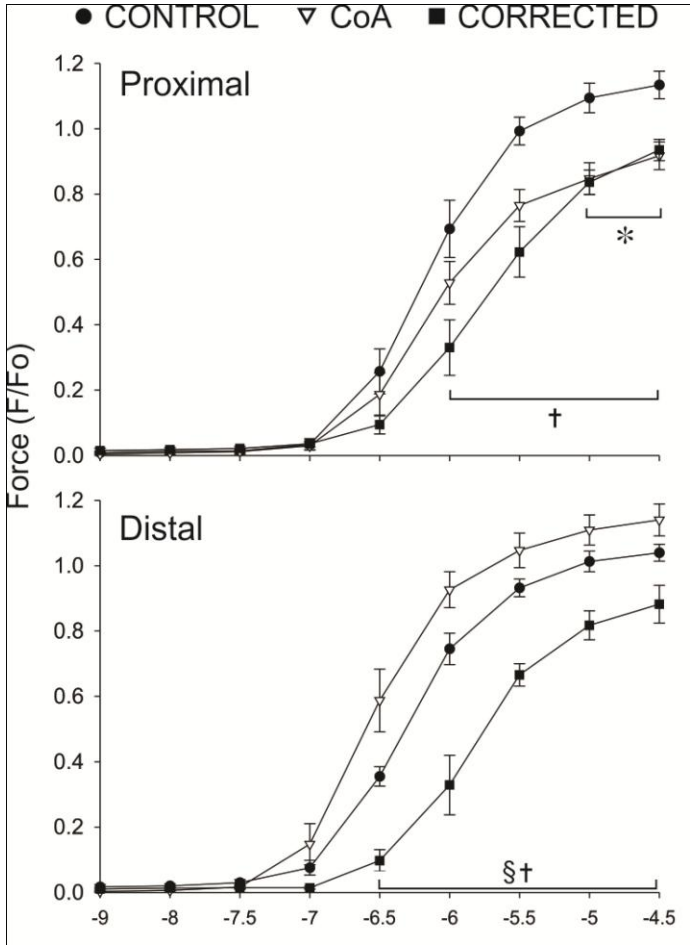

Figure 29. Active contraction curves in response to PE for rings of aortic tissue proximal (top) and distal (bottom to the coarctation region in CoA and corrected groups as compared to spatially equivalent locations from control rabbits. ✻ = CoA significantly different (P<0.05) from control; † = corrected significantly different (P<0.05) from control; § = CoA significantly different (P<0.05) from corrected.

6.3.3 Time to peak contraction

Time to peak contractile response of K^+PSS quantified from arteries proximal and distal to CoA is displayed in **Figure 30**. In proximal arteries, untreated CoA samples demonstrated significantly increased time to reach peak contraction. Time to peak

contraction in arteries of corrected CoA rabbits in this region were slightly increased, but did not reach significance. Differences between groups were abolished distal to CoA.

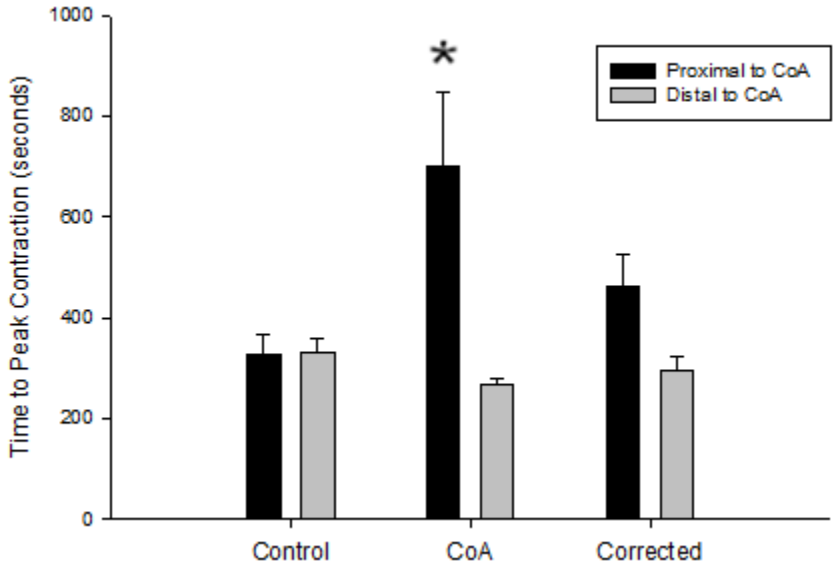

Figure 30. Time to peak K^+PSS contraction in respective experimental groups in dAo arteries proximal and distal to CoA. Values are presented ± SEM, ✻ = CoA significantly different ($P<0.05$) from control.

6.4 SUMMARY

The myograph techniques applied to the animal model used for the current investigation illustrates a method for quantifying endothelial and contractile function of the aortic vasculature in response to untreated and corrected CoA. While previous research has identified impaired endothelial relaxation and altered contractility to occur in response to acute hypertension and vascular injury of conduit arteries [95, 150], the specific effects of CoA and correction have not been investigated to date in a clinically representative model. The current aim provides a reproducible method of analysis by which changes to endothelial function as well as resting and active force can be observed

following CoA and correction representative of surgical treatment at spatial locations where hemodynamic and vascular biomechanics indices can be determined.

Endothelial dysfunction

Proximal dAo arteries from untreated and corrected experimental groups demonstrate endothelial dysfunction as ACh relaxation response from both groups showed significant impairments while peak SNP relaxation response (endothelium-independent) was unchanged. These results suggest a reduced NO bioavailability present in both untreated and corrected groups in the proximal arteries, possibly due to the damaging effects of elevated SBP and pulse BP. Distal arteries of the CoA group continued to show endothelial dysfunction, while no differences between corrected and controls were present. Importantly peak ACH relaxation in CoA and corrected groups ranged from 10-20%, and previous research using similar myograph methods consider ACH relaxation less than 50% to be non-functional [151]. While endothelial dysfunction in proximal arteries of untreated CoA rabbits is in agreement with spontaneously hypertensive animal models [95], the data presented from corrected rabbits is the first to demonstrate endothelial dysfunction in coarctation despite complete BP alleviation. These results are consistent with recent clinical evaluations of normotensive post-repair patients who demonstrate reduced forearm vasodilation during reactive hyperemia compared to age-matched control patients [65, 70]. Atherosclerosis, particularly in coronary artery disease, is associated with endothelial dysfunction as a result of reduced endothelial NO release, and indeed high rates of early-onset coronary artery disease are a primary form of morbidity leading to reduced life expectancy in surgically treated CoA

[9, 27]. Whether the etiology of endothelial dysfunction observed here is a result of reactive oxygen species or increased expression of inflammatory and/or adhesion molecules is currently unclear. Previous studies investigating NO bioavailability in aorta-banded hypertensive animal models report evidence of increased expression of reactive oxygen species in proximal arteries and unchanged expression in regions distally [97, 152, 153]. While a considerable difference was present in terms of BP gradients used (~20 mmHg in current study vs. 75-100 mmHg in cited studies) these studies may suggest a possible explanation for reduced NO availability in untreated and corrected CoA which leads to the substantial late morbidities observed.

The finding of endothelial impairment in distal arteries of CoA rabbits may be attributable to the presence of high velocity and WSS in these regions. Previous research demonstrated remodeling and fragmentation of the IEL to occur under significantly increased blood flow rates [154]. Thus sustained conditions of increased flow in the untreated CoA group due to the stentoic velocity jet may serve to alter the endothelial environment and subsequently NO release. IEL fragmentation due to high WSS may also explain the slight increase in distal dAo SNP relaxation response at several concentrations, as NO may diffuse more readily into medial smooth muscle to cause relaxation.

The possible influence of structural alterations to endothelial dysfunction must be considered as well. Vascular remodeling is evident in the form of fragmented elastin and increased medial thickness in CoA and corrected proximal arteries, and these changes may conceivably cause increased NO diffusion distance and altered NO relaxation of

SMC. However, since CoA and corrected rabbits demonstrate peak SNP relaxation similar to controls it is unlikely that structural changes affect SMC relaxation to NO.

Altered vascular contractility

Myograph results demonstrated reduced active tone through diminished PE force response in proximal arteries of both untreated and corrected rabbits. These findings are likely a direct consequence of the increased passive stiffness illustrated in these regions in Aim 1. In order to maintain the vessel diameter, previous work with hypertensive rat arterioles illustrated that increasing passive force decreases the capacity for active force response [45]. Although studied less frequently than resistance vessels, conduit arteries demonstrate an ability to adapt smooth muscle tone in response to WSS and BP to control luminal diameter [17]. In both untreated and corrected CoA, elevated BP due to the stenosis causes alterations to vessel stiffness and vascular medial thickness. It is possible that if vascular remodeling increases resting force in response to CoA-induced mechanical stimuli, active force of proximal aortas in untreated and treated groups must be limited to avoid excessive vasoconstriction and narrowing of the lumen. Furthermore, since maximum active force in the untreated and corrected groups was reduced compared to control, it is likely that active force is a consequence of aortic stiffness and not a contributing factor.

Reduced active force observed in distal arteries of corrected rabbits occurred without transient increase in BP and is thus not strictly consistent with proximal results. The presence of significantly reduced TAWSS in corrected rabbits at this region from

CFD results may explain reduced tension, as alterations in WSS may affect smooth muscle contractility *(discussed in limitations)*.

Results from time to peak contraction K^+PSS measurements revealed untreated CoA had significantly longer contraction times in the proximal region, while no differences were present in the distal region. K+PSS causes contraction through two mechanisms. The primary mechanism is thought to occur by the depolarization of smooth muscle membrane by K^+, which causes the opening of voltage-dependent channels and thus an influx of calcium, while a secondary mechanism of calcium sensitization through translocation of RhoKinase may play a minor role in contraction as well [155]. It is possible that structural changes in the form of increased medial thickness in proximal untreated CoA (and to a minor extent corrected CoA) may increase diffusion distance for calcium, thus increasing the time to peak contraction. Changes in cytoskeletal proteins may result in altered resting mechanical properties which affect contractile force response time, as increased stiffness should result in reduced time to peak contraction. However the opposite trend is observed in the current results, as proximal untreated CoA arteries showed significantly increased stiffness. Thus it is likely that cytoskeletal alterations to passive mechanical properties can be ruled out as a cause of increased time to peak contraction. Lastly, it is possible that changes in second messenger pathways including IP3 and PKC may be altered in CoA pathology such that calcium transport is affected [156, 157]. However, without parallel observation of contraction time with appropriate inhibitors to calcium-dependent pathways and measurement of transient calcium currents, second messenger changes cannot be confirmed.

6.5 Limitations

While the current methods allow comparison of functional properties in CoA, results should be considered against several potential limitations. Perhaps the most significant is the use of a uniform resting force for all groups. Arteries are thought to operate at a consistent functional length, discussed previously in *methods*. Preliminary experiments identified a resting force of 2g to be an appropriate resting length in control rabbits; however it is conceivable that structural and functional changes are present in untreated and corrected CoA rabbits which may result in an altered functional length and thus resting force in these groups. It was reasoned that making consistent comparisons across groups was of greater importance than using a variable resting force for each group after review of literature using myograph analysis in pathophysiological states [95, 150, 158] and discussions with an expert researcher in this area [146, 159] (Dr. Katherine Gauthier, personal communication).

Differences in active force observed across groups are thought to be a result of changes in resting and active components of smooth muscle contraction, independent of intracellular calcium regulation. However, it is conceivable that observations may be a result of calcium-dependent pathways including cGMP kinase and L-type channels, or calcium-independent G-protein coupling, all of which serve to alter contractility in response to sustained hemodynamic stimuli through shear stress [38, 39, 160, 161]. Future studies using inhibitors for calcium channels (Verapamil) and agonist activation (Phentolamine) are feasible using the current methods and will allow the determination of calcium-dependent regulation in contractile force response in untreated and corrected

CoA. Several studies have indicated mechanisms by which contractile response is calcium-independent [39, 147], identifying the Rho kinase pathway as being primarily responsible for this phenomenon, with protein kinase C (PKC) involved to a lesser degree [38, 160]. To obviate this limitation, future models *in vivo* models will analyze peak contractile response to KPSS and Phe before and after incubation with Y-6732, a highly specific Rho-kinase inhibitor to determine what role if any calcium sensitization plays.

Preliminary experiments with the current rabbit model have shown the maximum effective relaxation of healthy controls to ACH is approximately 80%. A review of studies investigating endothelial relaxation in the thoracic aorta routinely reveals +90% relaxation of pre-contracted force [146, 159]. These studies further demonstrated a decrease in endothelial relaxation to occur with increasing age. Therefore this limitation may be attributable to the 32-week timeline of rabbits used in the present study, as compared to the 4-8 week animal models used in previous studies. Since the objective of the current aim was to quantify endothelial relaxation across untreated and corrected groups and timelines were identical across groups, this limitation is not likely to influence conclusions.

While changes in active force were quantified across groups, it is possible that evaluation of vascular tension, defined as pressure*radius, may be more pertinent to physiological vascular function. The current experiment did not facilitate the use of a controlled pressure-diameter setup which may allow evaluation of passive and active tension *in situ*.

CHAPTER 7: FUTURE DIRECTIONS AND CONCLUSIONS

7.1 Review of investigation findings

The work presented has provided unique insight into the consequences of CoA and correction that consider hemodynamic, structural, and functional changes caused by the disease. Collectively, results provide evidence that the ramifications of coarctation go beyond removal of the stenosis and restoration of the pressure gradient. The unique contributions this work has made to the field are as follows and summarized in a simplified table to display significant differences (Table 5):

1) Subject specific CFD simulations using an established animal model of CoA and correction consistent with BP gradient endpoint criteria of CoA intervention in humans, as well as morphological outcomes in agreement with previous imaging studies, revealed significant hemodynamic alterations in the form of reduced TAWSS in proximal arteries and markedly increased TAWSS in the distal aorta of untreated CoA subjects. Distal alterations to hemodynamics may be particularly important as corrected subjects demonstrated reduced TAWSS persists despite BP restoration. Increased stiffening in the proximal arteries of both untreated and corrected CoA subjects was demonstrated through analysis of vascular biomechanics quantified from CFD simulations. These findings suggest altered hemodynamics and vascular biomechanics in untreated and corrected CoA may influence any structural and functional changes present in these groups.
2) Structural changes in the form of increased medial thickness and elastin fragmentation were found to occur in the proximal arteries of untreated CoA through histological analysis. These changes persist in the corrected group,

suggesting mechanisms of medial thickening occur before correction at 8-10 weeks and are not restored with alleviation of BP.

3) Analysis of smooth muscle differentiation protein expression demonstrated significantly increased NM myosin expression and decreased SM MHC expression in proximal arteries of both untreated and corrected CoA. This dedifferentiation may influence vascular biomechanics indices of reduced strain and distensibility observed.

4) Impaired ACh relaxation occurred in the proximal arteries of both untreated and corrected groups while SNP relaxation was >90%, indicating endothelial dysfunction occurs in untreated CoA and persists with correction. In addition, reduced active force was present in untreated and corrected groups, likely due to the elevated passive stiffness in these arteries.

Changes vs. control	Proximal to CoA		Distal to CoA	
	CoA	Corrected	CoA	Corrected
Blood Pressure	↑	NC	NC	NC
Wall shear stress	↓	NC	↑↑	↓
Medial thickness	↑	↑	NC	NC
Vascular stiffness	↑↑	↑	N/A	N/A
Vessel contractility	↓	↓	NC	↓
EC relaxation	↓↓	↓	↓	NC
SMC relaxation	NC	NC	↑	NC

Table 6. Summary of significant changes to measured parameters compared to controls. ↑ = significant increase (↑↑ marked increase); ↓ = significant decrease (↓↓ marked decrease); NC = No significant differences; N/A = Measurement not available.

CoA causes increased BP and tensile stress as well as reduced TAWSS in proximal arteries which results in SMC phenotypic changes evidenced by NM myosin and SM MHC. This dedifferentiation results in increased medial thickness and increased stiffness, which reduces the need for active force response. Furthermore, the increased tensile stress and reduced TAWSS causes proximal endothelial dysfunction in CoA. Distally TAWSS is markedly increased by the stenotic velocity jet, which causes endothelial dysfunction and increased SMC (endothelium-*independent*) relaxation. These results are somewhat in agreement with work by [154] who presents evidence that high WSS results in fragmentation and disruptions of the IEL which may explain loss of mechanical properties.

Despite no change in BP or TAWSS in the proximal arteries of corrected rabbits, dedifferentiation persists and continues to cause increased medial thickness and increased stiffness, reducing the need for active force response. Endothelial dysfunction persists in proximal corrected arteries and is thus established within 8-10 weeks of CoA. Distally the residual dilatation present in corrected aorta results in reduced TAWSS which causes a reduced active force response.

7.2 Future Directions

The findings in the presented research lend themselves to various applications in biomedical engineering and medicine directed at future research and treatment techniques of congenital CoA. These may include the identification of cellular mechanisms present in the CoA pathology and the development of exercise therapies for CoA patients.

Cellular mechanisms

Global changes in structure and function have been identified due to CoA and correction; however the development of novel interventions may require identification of specific cellular mechanisms which result in changes to medial thickness and vascular function. Research utilizing animal models of hypertension and flow ligation have identified possible mechanistic pathways to these stimuli, with TGF-β, fibronectin, heparin sulfate glycosaminoglycans (HSPGs), and matrix metalloproteases (MMPs) all suggested to play considerable roles in the vascular remodeling and functional response [36, 74, 103, 126, 130, 162-164]. These mechanisms may be similarly involved in CoA in a manner that explains structural and functional changes, and the current research for the first time provides a reproducible model to investigate these phenomena in the pathophysiology of untreated and corrected CoA. Successful identification of pathways leading to long term morbidities in CoA may allow application of inhibitors to augment surgical treatment and thus improve patient outcomes of life expectancy.

Exercise Therapies

The current research demonstrates evidence of altered endothelial function occurring due to CoA and persistent upon correction. Normal endothelial function is integral to vascular health due to the production of numerous vasodilators, anti-inflammatory, and antithrombotic agents. Impaired NO availability and relaxation is associated with numerous negative cardiovascular outcomes as previously discussed. Interestingly, recent research suggests that if the endothelium is activated during exercise,

it can be postulated that repetitive exposure to exercise induced hemodynamic and WSS changes may result in adaptation such that the NO dilatory function is up-regulated. Indeed, regular exercise training is associated with increased vasodilator capacity and longitudinal studies suggest an anti-atherogenic effect with regular activity [37, 165, 166]. The current research uniquely identifies persistent endothelial dysfunction to occur in proximal arteries despite CoA correction, and thus suggests a potential benefit for the development of simple exercises, such as an isometric hand-grip routine, to augment post-surgical treatment. Children with CoA are generally discouraged from exercise due to the potential negative effects from the increase in BP during the exercise itself. However, development of these relatively light exercise regiments would serve to increase endothelial stimulation of the proximal arteries and thus may improve endothelial function in a manner that counteracts negative changes due to CoA. Additionally, exercise treatments may mitigate the need for extended drug therapies for these patients, which is of particular benefit when considering the young age of patients undergoing surgical CoA treatment.

7.3 Conclusions

The present results demonstrate that untreated and corrected CoA result in alterations to hemodynamics, vascular structure, and vascular function that occur independent of genetic or developmental factors. Untreated CoA causes significant alterations to TAWSS in the proximal and distal thoracic aorta, and these changes persist in the distal region despite correction of CoA and alleviation of BP. Medial thickening and increased passive stiffness occur in the proximal arteries of both untreated and

corrected CoA. In addition, the functional properties of untreated and corrected CoA subjects are significantly disturbed as endothelial dysfunction and reduced active tension is present in both groups. The animal model creates a platform to accurately replicate untreated CoA and surgical correction through resection and end-to-end anastomosis for the first time, while the use of a coupled imaging and experimental technique allows unique localization of hemodynamic and vascular biomechanics alterations and parallel observation of structural and functional changes which may have direct consequences on cardiovascular health. In addition to providing a unique insight of CoA pathology to clinicians, the current methods may facilitate the identification of specific cellular mechanisms leading to late morbidities, which may lead to targeted inhibitors as therapeutic agents.

BIBLIOGRAPHY

1. Leschka, S., et al., *Pre- and postoperative evaluation of congenital heart disease in children and adults with 64-section CT.* Radiographics, 2007. **27**(3): p. 829-46.

2. Kirk, C.R., *Thumbnail Guide to Congenital Heart Disease*, 2006.

3. Gargiulo, G., et al., *Neonatal coarctation repair using extended end-to-end anastomosis. Multimedia Manual of Cardiothroacic Surgery*, 2008.

4. Nichols, W.W. and M.F. O'Rourke, *McDonald's Blood Flow in Arteries: Theoretical, Experimental and Clinical Principles*. 5th Ed. ed. 2005, New York: Hodder Arnold. 77.

5. DMT-USA, I., *Wire Myograph System*, D.M. Technologies, Editor 2011: Ann Arbor, 48104 MI USA.

6. Marieb, E. and K. Hoehn, *Human Anatomy and Physiology, 7/E*. 7th ed. 2006: Benjamin Cummings; 7 edition. 1159.

7. Kirklin, J.W. and B.G. Barratt-Boyes, *Coarctation of the aorta*, in *Cardiac surgery*. 1992, Churchill Livingstone Inc.: New York. p. 1264-1303.

8. Marshall, A.C., et al., *Early results and medium-term follow-up of stent implantation for mild or recurrent aortic coarctation.* Am Heart J, 2000. **139**: p. 1054-60.

9. Perloff, J.K., *Coarctation of the aorta*, in *Clinical recognition of congenital heart disease*. 2003, Saunders: Philadelphia. p. 113-43.

10. O'Rourke, M.F. and T.B. Cartmill, *Influence of aortic coarctation on pulsatle hemodynamics in the proximal aorta.* Circulation, 1971. **44**(2): p. 281-92.

11. Xu, C., C.K. Zarins, and S. Glagov, *Biphasic response of tropoelastin at the poststenotic dilation segment of the rabbit aorta.* J Vasc Surg, 2002. **36**(3): p. 605-12.

12. Xu, J., et al., *Intravascular ultrasound assessment of regional aortic wall stiffness, distensibility, and compliance in patients with coarctation of the aorta.* American Heart Journal, 1997. **134**(1): p. 93-8.

13. Ladisa, J.F., et al., *Computational simulations for aortic coarctation: representative results from a sampling of patients.* J Biomech Eng, 2011. **133**(9): p. 091008.

14. LaDisa, J.F., et al., *Computational simulations demonstrate altered wall shear stress in aortic coarctation patients treated by resection with end-to-end anastomosis.* Congenit Heart Dis, 2011. **6**(5): p. 432-43.

15. Kawashima, S. and M. Yokoyama, *Dysfunction of endothelial nitric oxide synthase and atherosclerosis.* Arterioscler Thromb Vasc Biol, 2004. **24**(6): p. 998-1005.

16. Ueno, H., et al., *Blood flow regulates the development of vascular hypertrophy, smooth muscle cell proliferation, and endothelial cell nitric oxide synthase in hypertension.* Hypertension, 2000. **36**(1): p. 89-96.

17. Fitch, R.M., et al., *Synergistic effect of angiotensin II and nitric oxide synthase inhibitor in increasing aortic stiffness in mice.* Am J Physiol Heart Circ Physiol, 2006. **290**(3): p. H1190-8.

18. Ferencz, C., et al., *Congenital heart disease: prevalence at livebirth. The Baltimore-Washington Infant Study.* American Journal of Epidemiology, 1985. **12**(1): p. 31-6.

19. Michelakis, E.D., et al., *O2 sensing in the human ductus arteriosus: regulation of voltage-gated K+ channels in smooth muscle cells by a mitochondrial redox sensor.* Circ Res, 2002. **91**(6): p. 478-86.

20. Elgamal, M.A., E.D. McKenzie, and C.D. Fraser, *Aortic arch advancement: the optimal one-stage approach for surgical management of neonatal coarctation with arch hypoplasia.* Ann Thorac Surg, 2002. **73**(4): p. 1267-72; discussion 1272-3.

21. Sybert, V.P. and E. McCauley, *Turner's syndrome.* N Engl J Med, 2004. **351**(12): p. 1227-38.

22. Rosenthal, E., S.A. Qureshi, and M. Tynan, *Stent implantation for aortic recoarctation.* Am Heart J, 1995. **129**(6): p. 1220-1.

23. Ebeid, M.R., L.R. Prieto, and L.A. Latson, *Use of balloon-expandable stents for coarctation of the aorta: initial results and intermediate-term follow-up.* J Am Coll Cardiol, 1997. **30**(7): p. 1847-52.

24. Singer, M.I., M. Rowen, and T.J. Dorsey, *Transluminal aortic balloon angioplasty for coarctation of the aorta in the newborn.* Am Heart J, 1982. **103**: p. 131-2.

25. O'Laughlin, M.P., et al., *Use of endovascular stents in congenital heart disease.* Circulation, 1991. **83**: p. 1923-39.

26. Carr, J.A., *The results of catheter-based therapy compared with surgical repair of adult aortic coarctation.* J Am Coll Cardiol, 2006. **47**(6): p. 1101-7.

27. Anagnostopoulos-Tzifa, A., *Management of aortic coarctation in adults: endovascular versus surgical therapy.* Hellenic J Cardiol, 2007. **48**(5): p. 290-5.

28. GROSS, R.E., *Surgical correction for coarctation of the aorta.* Surgery, 1945. **18**: p. 673-8.

29. Zang, P., et al., *Intraprocedural cerebral aneurysm rupture during endovascular coiling.* Neurol India, 2011. **59**(3): p. 369-72.

30. Kühn, A., et al., *Impaired elastic properties of the ascending aorta persist within the first 3 years after neonatal coarctation repair.* Pediatr Cardiol, 2009. **30**(1): p. 46-51.

31. Hernandez-Gonzalez, M., et al., *Intraluminal aortoplasty vs. surgical aortic resection in congenital aortic coarctation. A clinical random study in pediatric patients.* Archives of Medical Research, 2003. **34**(4): p. 305-10.

32. Backer, C.L., et al., *Repair of coarctation with resection and extended end-to-end anastomosis.* Ann Thorac Surg, 1998. **66**(4): p. 1365-70; discussion 1370-1.

33. Pfammatter, J.P., et al., *Isolated aortic coarctation in neonates and infants: results of resection and end-to-end anastomosis.* Ann Thorac Surg, 1996. **62**(3): p. 778-82; discussion 782-3.

34. Lehoux, S., Y. Castier, and A. Tedgui, *Molecular mechanisms of the vascular responses to haemodynamic forces.* J Intern Med, 2006. **259**(4): p. 381-92.

35. Humphrey, J.D., *Vascular adaptation and mechanical homeostasis at tissue, cellular, and sub-cellular levels.* Cell Biochem Biophys, 2008. **50**(2): p. 53-78.

36. Humphrey, J.D., *Mechanisms of arterial remodeling in hypertension: coupled roles of wall shear and intramural stress.* Hypertension, 2008. **52**(2): p. 195-200.

37. Maiorana, A., et al., *Exercise and the nitric oxide vasodilator system.* Sports Med, 2003. **33**(14): p. 1013-35.

38. Ainslie, K., et al., *Rat aortic smooth muscle cells contract in response to serum and its components in a calcium independent manner.* Ann Biomed Eng, 2004. **32**(12): p. 1667-75.

39. Civelek, M., et al., *Smooth muscle cells contract in response to fluid flow via a Ca2+-independent signaling mechanism.* J Appl Physiol, 2002. **93**(6): p. 1907-17.

40. Rush, J.W., S.G. Denniss, and D.A. Graham, *Vascular nitric oxide and oxidative stress: determinants of endothelial adaptations to cardiovascular disease and to physical activity.* Can J Appl Physiol, 2005. **30**(4): p. 442-74.

41. Malek, A.M., S.L. Alper, and S. Izumo, *Hemodynamic shear stress and its role in atherosclerosis.* JAMA, 1999. **282**(21): p. 2035-42.

42. Cohen, M., et al., *Coarctation of the aorta. Long-term follow-up and prediction of outcome after surgical correction.* Circulation, 1989. **80**(4): p. 840-5.

43. Graham, D.A. and J.W. Rush, *Cyclooxygenase and thromboxane/prostaglandin receptor contribute to aortic endothelium-dependent dysfunction in aging female spontaneously hypertensive rats.* J Appl Physiol, 2009. **107**(4): p. 1059-67.

44. Graham, D.A. and J.W. Rush, *Exercise training improves aortic endothelium-dependent vasorelaxation and determinants of nitric oxide bioavailability in spontaneously hypertensive rats.* J Appl Physiol, 2004. **96**(6): p. 2088-96.

45. Bohlen, H.G. and J.M. Lash, *Active and passive arteriolar regulation in spontaneously hypertensive rats.* Hypertension, 1994. **23**(6 Pt 1): p. 757-64.

46. Ong, C.M., et al., *Increased stiffness and persistent narrowing of the aorta after successful repair of coarctation of the aorta: relationship to left ventricular mass and blood pressure at rest and with exercise.* American Heart Journal, 1992. **123**(6): p. 1594-600.

47. Laurent, S., P. Boutouyrie, and P. Lacolley, *Structural and genetic bases of arterial stiffness.* Hypertension, 2005. **45**(6): p. 1050-5.

48. Weber, T., et al., *Arterial stiffness and arterial wave reflections are associated with systolic and diastolic function in patients with normal ejection fraction.* Am J Hypertens, 2008. **21**(11): p. 1194-202.

49. Weber, T., et al., *Arterial stiffness, wave reflections, and the risk of coronary artery disease.* Circulation, 2004. **109**(2): p. 184-9.

50. Fridez, P., et al., *Adaptation of conduit artery vascular smooth muscle tone to induced hypertension.* Ann Biomed Eng, 2002. **30**(7): p. 905-16.

51. Fridez, P., et al., *Short-Term biomechanical adaptation of the rat carotid to acute hypertension: contribution of smooth muscle.* Ann Biomed Eng, 2001. **29**(1): p. 26-34.

52. O'Rourke, M.F. and M.G. Taylor, *Input impedance of the systemic circulation.* Circ Res, 1967. **20**(4): p. 365-80.

53. Westerhof, N., et al., *Analog studies of the human systemic arterial tree.* J Biomech, 1969. **2**(2): p. 121-43.

54. Westerhof, N., N. Stergiopulos, and M.I.M. Noble, *Snapshots of hemodynamics an aid for clinical research and graduate education*. 2005, New York: Springer.

55. Stergiopulos, N., P. Segers, and N. Westerhof, *Use of pulse pressure method for estimating total arterial compliance in vivo.* Am J Physiol Heart Circ Physiol, 1999. **276**(45): p. H424-8.

56. Araoz, P.A., et al., *MR findings of collateral circulation are more accurate measures of hemodynamic significance than arm-leg blood pressure gradient after repair of coarctation of the aorta.* J Magn Reson Imaging, 2003. **17**(2): p. 177-83.

57. Kilner, P.J., et al., *Helical and retrograde secondary flow patterns in the aortic arch studied by three-directional magnetic resonance velocity mapping.* Circulation, 1993. **88**(5 Pt 1): p. 2235-47.

58. Frydrychowicz, A., et al., *Image analysis in time-resolved large field of view 3D MR-angiography at 3T.* J Magn Reson Imaging, 2008. **28**(5): p. 1116-24.

59. Frydrychowicz, A., et al., *Visualization of vascular hemodynamics in a case of a large patent ductus arteriosus using flow sensitive 3D CMR at 3T.* J Cardiovasc Magn Reson, 2007. **9**(3): p. 585-7.

60. Vriend, J.W., et al., *Age at repair and left ventricular mass in patients after repair of aortic coarctation.* J Thorac Cardiovasc Surg, 2005. **130**(3): p. 896-7.

61. Vriend, J.W., et al., *Carotid intima-media thickness in post-coarctectomy patients with exercise induced hypertension.* Heart, 2005. **91**(7): p. 962-3.

62. Vriend, J.W., et al., *Increased carotid and femoral intima-media thickness in patients after repair of aortic coarctation: influence of early repair.* Am Heart J, 2006. **151**(1): p. 242-7.

63. O'Leary, D.H., et al., *Carotid-artery intima and media thickness as a risk factor for myocardial infarction and stroke in older adults. Cardiovascular Health Study Collaborative Research Group.* N Engl J Med, 1999. **340**(1): p. 14-22.

64. Niwa, K., et al., *Structural abnormalities of great arterial walls in congenital heart disease: light and electron microscopic analyses.* Circulation, 2001. **103**(3): p. 393-400.

65. Brili, S., et al., *Evidence of vascular dysfunction in young patients with successfully repaired coarctation of aorta.* Atherosclerosis, 2005. **182**(1): p. 97-103.

66. Vriend, J.W., et al., *Predictive value of mild, residual descending aortic narrowing for blood pressure and vascular damage in patients after repair of aortic coarctation.* European Heart Journal, 2005. **26**(1): p. 84-90.

67. Bianchini, E., et al., *Assessment of carotid stiffness and intima-media thickness from ultrasound data: comparison between two methods.* J Ultrasound Med, 2010. **29**(8): p. 1169-75.

68. Philpott, A.C., et al., *Comparison of new measures of vascular function to flow mediated dilatation as a measure of cardiovascular risk factors.* Am J Cardiol, 2009. **103**(11): p. 1610-5.

69. Heger, M., et al., *Vascular dysfunction after coarctation repair is related to the age at surgery.* Int J Cardiol, 2005. **99**(2): p. 295-9.

70. Brili, S., et al., *Effects of ramipril on endothelial function and the expression of proinflammatory cytokines and adhesion molecules in young normotensive subjects with successfully repaired coarctation of aorta: a randomized cross-over study.* J Am Coll Cardiol, 2008. **51**(7): p. 742-9.

71. Vignon, I., K.C. Jansen, and C.A. Taylor. *Outflow boundary conditions for finite element modeling of blood flow in arteries*. in *Sixth World Congress on Computational Mechanics*. 2004. Beijing, China: Tsinghua University Press & Springer-Verlag.

72. Wentzel, J.J., et al., *Does shear stress modulate both plaque progression and regression in the thoracic aorta? Human study using serial magnetic resonance imaging.* J Am Coll Cardiol, 2005. **45**(6): p. 846-54.

73. Frydrychowicz, A., et al., *Multidirectional flow analysis by cardiovascular magnetic resonance in aneurysm development following repair of aortic coarctation.* J Cardiovasc Magn Reson, 2008. **10**: p. 30.

74. Xu, C., et al., *Molecular mechanisms of aortic wall remodeling in response to hypertension.* J Vasc Surg, 2001. **33**(3): p. 570-8.

75. Xu, C., et al., *Differential transmural distribution of gene expression for collagen types I and III proximal to aortic coarctation in the rabbit.* J Vasc Res, 2000. **37**(3): p. 170-82.

76. Beekman, R.H., et al., *Reoperation for coarctation of the aorta.* American Journal of Cardiology, 1981. **48**(6): p. 1108-14.

77. Greve, J.M., et al., *Allometric scaling of wall shear stress from mice to humans: quantification using cine phase-contrast MRI and computational fluid dynamics.* Am J Physiol Heart Circ Physiol, 2006. **291**(4): p. H1700-8.

78. Wilson, N., et al., *A software framework for creating patient specific geometric models from medical imaging data for simulation based medical planning of vascular surgery.* Lect Notes Comput Sci, 2001. **2208**: p. 449-456.

79. Stergiopulos, N., J.J. Meister, and N. Westerhof, *Simple and accurate way for estimating total and segmental arterial compliance: the pulse pressure method.* Ann Biomed Eng, 1994. **22**(4): p. 392-7.

80. Stergiopulos, N., D.F. Young, and T.R. Rogge, *Computer simulation of arterial flow with applications to arterial and aortic stenoses.* J Biomech, 1992. **25**(12): p. 1477-88.

81. Laskey, W.K., et al., *Estimation of total systemic arterial compliance in humans.* J Appl Physiol, 1990. **69**(1): p. 112-9.

82. Taylor, C.A., T.J.R. Hughes, and C.K. Zarins, *Computational investigations in vascular disease.* Computers in Physics, 1996. **10**(3): p. 224-232.

83. Taylor, C.A., T.J.R. Hughes, and C.K. Zarins, *Finite element modeling of three-dimensional pulsatile flow in the abdominal aorta: Relevance to atherosclerosis.* Ann Biomed Eng, 1998. **26**: p. 1-14.

84. Windberger, U., et al., *Whole blood viscosity, plasma viscosity and erythrocyte aggregation in nine mammalian species: reference values and comparison of data.* Exp Physiol, 2003. **88**(3): p. 431-40.

85. Figueroa, C.A., et al. *A coupled momentum method to model blood flow in deformable arteries*. in *Sixth World Congress on Computational Mechanics*. 2004. Beijing, China: Tsinghua University Press & Springer-Verlag.

86. Figueroa, C.A., et al. *A coupled-momentum method for fluid-structure interaction: applications to aortic coarctation*. in *Second International Conference on Computational Bioengineering*. 2005. Lisbon, Portugal.

87. Les, A.S., et al., *Quantification of hemodynamics in abdominal aortic aneurysms during rest and exercise using magnetic resonance imaging and computational fluid dynamics.* Ann Biomed Eng, 2010. **38**(4): p. 1288-313.

88. Tang, B.T., et al., *Abdominal aortic hemodynamics in young healthy adults at rest and during lower limb exercise: quantification using image-based computer modeling.* Am J Physiol Heart Circ Physiol, 2006. **291**(2): p. H668-76.

89. Bekkers, E.J. and C.A. Taylor. *Quantification of wall shear stress using 4D PCMRI*. in *ISMRM Flow and Motion Workshop*. 2004. Zurich, Switzerland.

90. Tang, B.T., et al., *Abdominal aortic hemodynamics in young healthy adults at rest and during lower limb exercise: quantification using image-based computer modeling.* Am J Physiol Heart Circ Physiol, 2006. **291**(2): p. H668-76.

91. Sho, E., et al., *Arterial enlargement, tortuosity, and intimal thickening in response to sequential exposure to high and low wall shear stress.* J Vasc Surg, 2004. **39**(3): p. 601-12.

92. Wentzel, J.J., et al., *Shear stress, vascular remodeling and neointimal formation.* J Biomech, 2003. **36**(5): p. 681-8.

93. Frydrychowicz, A., et al., *Time-resolved magnetic resonance angiography and flow-sensitive 4-dimensional magnetic resonance imaging at 3 Tesla for blood flow and wall shear stress analysis.* J Thorac Cardiovasc Surg, 2008. **136**(2): p. 400-7.

94. Stefanadis, C., et al., *Distensibility of the ascending aorta: comparison of invasive and non-invasive techniques in healthy men and in men with coronary artery disease.* Eur Heart J, 1990. **11**(11): p. 990-6.

95. Lee, S.K., et al., *Alteration of p66shc is associated with endothelial dysfunction in the abdominal aortic coarctation of rats.* FEBS Lett, 2008. **582**(17): p. 2561-6.

96. Vaziri, N.D., K. Liang, and Y. Ding, *Increased nitric oxide inactivation by reactive oxygen species in lead-induced hypertension.* Kidney Int, 1999. **56**(4): p. 1492-8.

97. Barton, C.H., Z. Ni, and N.D. Vaziri, *Enhanced nitric oxide inactivation in aortic coarctation-induced hypertension.* Kidney Int, 2001. **60**(3): p. 1083-7.

98. Wolinsky, H. and S. Glagov, *A lamellar unit of aortic medial structure and function in mammals.* Circ Res, 1967. **20**(1): p. 99-111.

99. Figueroa, C.A., et al., *A coupled momentum method for modeling blood flow in three-dimensional deformable arteries.* Comput Methods Appl Mech Eng, 2006. **195**: p. 5685-5706.

100. Owens, G.K., M.S. Kumar, and B.R. Wamhoff, *Molecular regulation of vascular smooth muscle cell differentiation in development and disease.* Physiol Rev, 2004. **84**(3): p. 767-801.

101. Li, C. and Q. Xu, *Mechanical stress-initiated signal transduction in vascular smooth muscle cells in vitro and in vivo.* Cell Signal, 2007. **19**(5): p. 881-91.

102. LaDisa, J.F., Jr., et al., *Alterations in wall shear stress predict sites of neointimal hyperplasia after stent implantation in rabbit iliac arteries.* Am J Physiol Heart Circ Physiol, 2005. **288**(5): p. H2465-75.

103. Chiang, H.Y., et al., *Fibronectin is an important regulator of flow-induced vascular remodeling.* Arterioscler Thromb Vasc Biol, 2009. **29**(7): p. 1074-9.

104. Korshunov, V.A. and B.C. Berk, *Flow-induced vascular remodeling in the mouse: a model for carotid intima-media thickening.* Arterioscler Thromb Vasc Biol, 2003. **23**(12): p. 2185-91.

105. Jimenez, M., et al., *Immunohistological and ultrastructural analysis of the intimal thickening in coarctation of human aorta.* Cardiovasc Res, 1999. **41**(3): p. 737-45.

106. Hu, J.J., et al., *Time courses of growth and remodeling of porcine aortic media during hypertension: a quantitative immunohistochemical examination.* J Histochem Cytochem, 2008. **56**(4): p. 359-70.

107. Eddinger, T.J. and D.P. Meer, *Myosin II isoforms in smooth muscle: heterogeneity and function.* Am J Physiol Cell Physiol, 2007. **293**(2): p. C493-508.

108. Vicente-Manzanares, M., et al., *Non-muscle myosin II takes centre stage in cell adhesion and migration.* Nat Rev Mol Cell Biol, 2009. **10**(11): p. 778-90.

109. Conti, M.A. and R.S. Adelstein, *Nonmuscle myosin II moves in new directions.* J Cell Sci, 2008. **121**(Pt 1): p. 11-8.

110. Thompson, J.A., et al., *Central Stiffening in Adulthood Linked to Aberrant Aortic Remodeling Under Suboptimal Intrauterine Conditions.* Am J Physiol Regul Integr Comp Physiol, 2011.

111. Kovács, M., et al., *Load-dependent mechanism of nonmuscle myosin 2.* Proc Natl Acad Sci U S A, 2007. **104**(24): p. 9994-9.

112. Greer, C.E., J.K. Lund, and M.M. Manos, *PCR amplification from paraffin-embedded tissues: recommendations on fixatives for long-term storage and prospective studies.* PCR Methods Appl, 1991. **1**(1): p. 46-50.

113. Greer, C.E., C.M. Wheeler, and M.M. Manos, *Sample preparation and PCR amplification from paraffin-embedded tissues.* PCR Methods Appl, 1994. **3**(6): p. S113-22.

114. Goldstein, N.S., et al., *Minimum formalin fixation time for consistent estrogen receptor immunohistochemical staining of invasive breast carcinoma.* Am J Clin Pathol, 2003. **120**(1): p. 86-92.

115. Baker, J.R., *Principles of biological microtechnique*. 1958, Methuen, London, UK.

116. Owens, G.K., *Regulation of differentiation of vascular smooth muscle cells.* Physiol Rev, 1995. **75**(3): p. 487-517.

117. Sobue, K. and J.R. Sellers, *Caldesmon, a novel regulatory protein in smooth muscle and nonmuscle actomyosin systems.* J Biol Chem, 1991. **266**(19): p. 12115-8.

118. Eddinger, T.J., J.D. Schiebout, and D.R. Swartz, *Adherens junction-associated protein distribution differs in smooth muscle tissue and acutely isolated cells.* Am J Physiol Gastrointest Liver Physiol, 2007. **292**(2): p. G684-97.

119. WOLINSKY, H. and S. GLAGOV, *STRUCTURAL BASIS FOR THE STATIC MECHANICAL PROPERTIES OF THE AORTIC MEDIA.* Circ Res, 1964. **14**: p. 400-13.

120. Stone, P.H., et al., *Effect of endothelial shear stress on the progression of coronary artery disease, vascular remodeling, and in-stent restenosis in humans: in vivo 6-month follow-up study.* Circulation, 2003. **108**(4): p. 438-444.

121. Wolinsky, H. and S. Glagov, *Comparison of abdominal and thoracic aortic medial structure in mammals. Deviation of man from the usual pattern.* Circ Res, 1969. **25**(6): p. 677-86.

122. Steelman, S.M. and J.D. Humphrey, *Differential remodeling responses of cerebral and skeletal muscle arterioles in a novel organ culture system.* Med Biol Eng Comput, 2011. **49**(9): p. 1015-23.

123. Zarins, C.K., et al., *Differential enlargement of artery segments in response to enlarging atherosclerotic plaques.* J Vasc Surg, 1988. **7**(3): p. 386-94.

124. Li, Y.S., J.H. Haga, and S. Chien, *Molecular basis of the effects of shear stress on vascular endothelial cells.* J Biomech, 2005. **38**(10): p. 1949-71.

125. Haga, J.H., Y.S. Li, and S. Chien, *Molecular basis of the effects of mechanical stretch on vascular smooth muscle cells.* J Biomech, 2007. **40**(5): p. 947-60.

126. Baker, A.B., et al., *Endothelial cells provide feedback control for vascular remodeling through a mechanosensitive autocrine TGF-beta signaling pathway.* Circ Res, 2008. **103**(3): p. 289-97.

127. Humphrey, J.D., *Mechanics of the arterial wall: review and directions.* Crit Rev Biomed Eng, 1995. **23**(1-2): p. 1-162.

128. Bezie, Y., et al., *Connection of smooth muscle cells to elastic lamellae in aorta of spontaneously hypertensive rats.* Hypertension, 1998. **32**(1): p. 166-9.

129. Berk, B.C., *Vascular smooth muscle growth: autocrine growth mechanisms.* Physiol Rev, 2001. **81**(3): p. 999-1030.

130. Arribas, S.M., et al., *Heightened aberrant deposition of hard-wearing elastin in conduit arteries of prehypertensive SHR is associated with increased stiffness and inward remodeling.* Am J Physiol Heart Circ Physiol, 2008. **295**(6): p. H2299-307.

131. Arribas, S.M., et al., *Enhanced survival of vascular smooth muscle cells accounts for heightened elastin deposition in arteries of neonatal spontaneously hypertensive rats.* Exp Physiol, 2010. **95**(4): p. 550-60.

132. Reusch, P., et al., *Mechanical strain increases smooth muscle and decreases nonmuscle myosin expression in rat vascular smooth muscle cells.* Circ Res, 1996. **79**(5): p. 1046-53.

133. Beningo, K.A., et al., *Nascent focal adhesions are responsible for the generation of strong propulsive forces in migrating fibroblasts.* J Cell Biol, 2001. **153**(4): p. 881-8.

134. Beningo, K.A., et al., *Traction forces of fibroblasts are regulated by the Rho-dependent kinase but not by the myosin light chain kinase.* Arch Biochem Biophys, 2006. **456**(2): p. 224-31.

135. O'Rourke, M.F. and M.E. Safar, *Relationship between aortic stiffening and microvascular disease in brain and kidney: cause and logic of therapy.* Hypertension, 2005. **46**(1): p. 200-4.

136. Xu, C., et al., *Hypercholesterolemia superimposed by experimental hypertension induces differential distribution of collagen and elastin.* Arterioscler Thromb Vasc Biol, 2000. **20**(12): p. 2566-72.

137. Drexler, H., *Factors involved in the maintenance of endothelial function.* Am J Cardiol, 1998. **82**(10A): p. 3S-4S.

138. Drexler, H., *Endothelial dysfunction: clinical implications.* Prog Cardiovasc Dis, 1997. **39**(4): p. 287-324.

139. Drexler, H. and B. Hornig, *Endothelial dysfunction in human disease.* J Mol Cell Cardiol, 1999. **31**(1): p. 51-60.

140. Meaume, S., et al., *Aortic pulse wave velocity predicts cardiovascular mortality in subjects >70 years of age.* Arterioscler Thromb Vasc Biol, 2001. **21**(12): p. 2046-50.

141. Ioannou, C.V., et al., *Left ventricular hypertrophy induced by reduced aortic compliance.* J Vasc Res, 2009. **46**(5): p. 417-25.

142. Ioannou, C.V., et al., *Hemodynamics induced after acute reduction of proximal thoracic aorta compliance.* Eur J Vasc Endovasc Surg, 2003. **26**(2): p. 195-204.

143. Speich, J.E., et al., *Adjustable passive length-tension curve in rabbit detrusor smooth muscle.* J Appl Physiol, 2007. **102**(5): p. 1746-55.

144. Speich, J.E., et al., *A mechanical model for adjustable passive stiffness in rabbit detrusor.* J Appl Physiol, 2006. **101**(4): p. 1189-98.

145. Smolensky, A.V. and L.E. Ford, *The extensive length-force relationship of porcine airway smooth muscle.* J Appl Physiol, 2007. **102**(5): p. 1906-11.

146. Gauthier, K.M., et al., *11(R),12(S),15(S)-trihydroxyeicosa-5(Z),8(Z),13(E)-trienoic acid: an endothelium-derived 15-lipoxygenase metabolite that relaxes rabbit aorta.* Am J Physiol Heart Circ Physiol, 2008. **294**(3): p. H1467-72.

147. Zhou, S., et al., *Paraoxon attenuates vascular smooth muscle contraction through inhibiting Ca2+ influx in the rabbit thoracic aorta.* J Biomed Biotechnol. **2010**: p. 829190.

148. Angus, J.A., et al., *Vasodilatation by acetylcholine is endothelium-dependent: a study by sonomicrometry in canine femoral artery in vivo.* J Physiol, 1983. **344**: p. 209-22.

149. Angus, J.A. and T.M. Cocks, *Role of endothelium in vascular responses to norepinephrine, serotonin and acetylcholine.* Bibl Cardiol, 1984(38): p. 43-52.

150. Denniss, S.G. and J.W. Rush, *Impaired hemodynamics and endothelial vasomotor function via endoperoxide-mediated vasoconstriction in the carotid artery of spontaneously hypertensive rats.* Am J Physiol Heart Circ Physiol, 2009. **296**(4): p. H1038-47.

151. López, D., et al., *Acidic reoxygenation protects against endothelial dysfunction in rat aortic rings submitted to simulated ischemia.* Am J Physiol Heart Circ Physiol, 2008. **295**(6): p. H2409-16.

152. Vaziri, N.D. and Z. Ni, *Expression of NOX-I, gp91phox, p47phox and P67phox in the aorta segments above and below coarctation.* Biochim Biophys Acta, 2005. **1723**(1-3): p. 321-7.

153. Vaziri, N.D. and Y. Ding, *Effect of lead on nitric oxide synthase expression in coronary endothelial cells: role of superoxide.* Hypertension, 2001. **37**(2): p. 223-6.

154. Masuda, H., et al., *Adaptive remodeling of internal elastic lamina and endothelial lining during flow-induced arterial enlargement.* Arterioscler Thromb Vasc Biol, 1999. **19**(10): p. 2298-307.

155. Ratz, P.H., et al., *Regulation of smooth muscle calcium sensitivity: KCl as a calcium-sensitizing stimulus.* Am J Physiol Cell Physiol, 2005. **288**(4): p. C769-83.

156. Khalil, R.A. and K.G. Morgan, *Phenylephrine-induced translocation of protein kinase C and shortening of two types of vascular cells of the ferret.* J Physiol, 1992. **455**: p. 585-99.

157. Villalba, N., et al., *Contribution of both Ca2+ entry and Ca2+ sensitization to the alpha1-adrenergic vasoconstriction of rat penile small arteries.* Am J Physiol Heart Circ Physiol, 2007. **292**(2): p. H1157-69.

158. Graham, D.A. and J.W. Rush, *Cyclooxygenase and thromboxane/prostaglandin receptor contribute to aortic endothelium-dependent dysfunction in aging female spontaneously hypertensive rats.* J Appl Physiol, 2009. **107**(4): p. 1059-67.

159. Gauthier, K.M., et al., *Apamin-sensitive K+ currents mediate arachidonic acid-induced relaxations of rabbit aorta.* Hypertension, 2004. **43**(2): p. 413-9.

160. Ainslie, K.M., et al., *Vascular smooth muscle cell glycocalyx influences shear stress-mediated contractile response.* J Appl Physiol, 2005. **98**(1): p. 242-9.

161. Sharma, R., et al., *Intracellular calcium changes in rat aortic smooth muscle cells in response to fluid flow.* Ann Biomed Eng, 2002. **30**(3): p. 371-8.

162. Chen, Z. and E. Tzima, *PECAM-1 is necessary for flow-induced vascular remodeling.* Arterioscler Thromb Vasc Biol, 2009. **29**(7): p. 1067-73.

163. Kawashima, S., et al., *Endothelial NO synthase overexpression inhibits lesion formation in mouse model of vascular remodeling.* Arterioscler Thromb Vasc Biol, 2001. **21**(2): p. 201-7.

164. Sho, E., et al., *High flow drives vascular endothelial cell proliferation during flow-induced arterial remodeling associated with the expression of vascular endothelial growth factor.* Exp Mol Pathol, 2003. **75**(1): p. 1-11.

165. Sinoway, L., et al., *Forearm training attenuates sympathetic responses to prolonged rhythmic forearm exercise.* J Appl Physiol, 1996. **81**(4): p. 1778-84.

166. Lee, I.M., H.D. Sesso, and R.S. Paffenbarger, *Physical activity and coronary heart disease risk in men: does the duration of exercise episodes predict risk?* Circulation, 2000. **102**(9): p. 981-6.